Al –Azhar University – Gaza
Deanship of Postgraduate Studies
Faculty of Applied Science
Department of Chemistry

Synthesis and Characterization of Encapsulated Metal Oxides Mesoporous Silica and their Curcumin Complexes

By

Nehal S. H. Tabassi.

Supervisors

Prof. Dr. Issa M. El-Nahhal
Professor of Inorganic Chemistry

Prof. Dr. Jamil K. Salem
Professor of Physical Chemistry

A thesis Submitted in Partial Fulfillment of Requirement for the Degree of master in chemistry

2017

Dedication

To

My parents

My sisters

My brothers

My uncle's soul

Acknowledgements

First of all, I am grateful to Allah, who granted me power and courage to finish this thesis.

This thesis would not be possible without the contribution of many mentors, co-workers, friends, and loved ones. While I cannot list everyone, I would like to especially thank the following people who have helped me succeed.

I wish to express my gratitude to my parents, and my siblings, for their love and support.

*I would like to thank my supervisors, Prof. **Dr. Issa M. El-Nahhal** and Prof. **Dr. Jamil K. Salem**, for their support, understanding, patience, and guidance through my graduate career. I am also grateful to the members of my committee for their assistance and support of my studies. In addition, I thank **Dr. Fauzi Qudeh**, who provided support, counsel, and advice, both professionally and personally.*

*I am also heavily indebted to the past and present members of the study group not only for providing an enjoyable work environment, but also for providing great friendship. I also wish to express my appreciation to **Sumayaa Abu Sharrekh** and **Sarah El-Bhessi** for advice and sharing their expertise with me. The faculty, staff, students, and support personnel within the chemistry department also deserve recognition for their part in my experience at Al-Azhar University.*

*Outside of the University, I wish to acknowledge **Mrs. Sylvia Kuhn** from Saarland University (Germany) and **Mr. Mohamed Selmane** from Université Piere Curie-Paris 6 (France) for their contributions to this work.*

Last but not least, I wish to thank the many family members, friends, and loved ones who have each contributed to this achievement.

While not individually listed, you know who you are, and I offer my sincerest thanks

Nehal S. H. Tabassi.

Ch. Nehal Tobassi

Abstract

Mesoporous silica materials were synthesized via sol-gel method using a series of triblock copolymer (Pluronic) surfactants (P-123, L-81, L-61 & L-31) as templates. Encapsulated metal oxides (CaO, MgO, CuO & ZnO) mesoporous silica were synthesized using impregnation method. In this method, metal precursors (metal acetate) were firstly loaded into the pores of mesoporous silica. Metal precursors were converted to metal oxide via calcination process at 600 ^{o}C. Curcumin-metal (II) complexes encapsulated mesoporous silica were synthesized by adding encapsulated metal oxide mesoporous silica to ethanolic curcumin solution. Mesoporous silica, encapsulated metal oxides mesoporous silica and curcumin-metal (II) complexes encapsulated mesoporous silica structural properties were investigated using several characterization techniques such as Fourier transform infrared spectroscopy (FTIR), X-ray diffraction (XRD), small angle X-ray scattering (SAXS), transmission electron microscopy (TEM) and thermal gravimetric analysis (TGA). Curcumin uptake % was examined using Ultraviolet-Visible spectroscopy (UV-vis). FTIR and TGA analysis prove that metal oxide were physically bonded with silanol groups, while curcumin was chemically bonded with metal oxides. SAXS pattern and TEM images show that mesoporous silica synthesized with short EO chain (below 5 units) surfactant gives lamellar meso-structure, while that synthesized with medium EO (17-31 units) chain gives 2D hexagonal (p6mm) meso-structure. They also prove that the loaded metal oxide did not alter the mesoscopic structure of used mesoporous silica materials. XRD confirmed the purity of synthesized materials and showed that the mean particle size of encapsulated metal oxide was changed according to the used mesoporous silica. UV-vis analysis shows that curcumin uptake % varied with used encapsulated metal oxide mesoporous silica.

توليف وتوصيف أكاسيد المعادن المغلفة بالميزوسليكا المسامية ومعقدات الكركمين لها

الملخص العربي

صُنعت مواد الميزوسيليكا المسامية عبر طريقة sol-gel ، باستخدام سلسلة من البوليمرات ثلاثية الوحدة البنائية (P-123, L-81, L-61 and L-31) ، التي استخدمت كقوالب. صُنعت أكاسيد المعادن (أكسيد الكالسيوم ، أكسيد الماغنيسيوم ، أكسيد النحاس و أكسيد الزنك) المغلفة بالميزوسلكا المسامية بطريقة التحميل. من خلال هذه الطريقة، يتم تحميل أملاح المعادن (أستيات المعدن) داخل مسامات مواد الميزوسيليكا المسامية أولًا. تُحول أملاح المعادن لأكاسيد المعادن عن طريق عملية التكليس عند600 درجة مئوية. تُصنع معقدات الكركمين مع أكاسيد المعادن المغلفة بالميزوسيليكا المسامية بإضافة أكسيد المعدن المغلف بالميزوسيليكا المسامية الى محلول الكركمين الكحولي. دُرست الخصائص الهيكلية لمواد الميزوسيليكا المسامية، أكاسيد المعادن المغلفة بالميزوسيليكا المسامية و معقدات الكركمين مع أكاسيد المعادن المغلفة بالميزوسيليكا المسامية باستخدام عدة تقنيات تشخيص، مثل: التحليل الطيفي بالأشعة تحت الحمراء (FTIR) ، المجهر الانتقالي الالكتروني (TEM) ، حيود الأشعة السينية (XRD)، الأشعة السينية صغيرة الزاوية المنتثرة (SAXS)، التحليل الوزني الحراري (TGA). حُددت النسبة المئوية لامتصاص الكركمين باستخدام مطيافية الأشعة فوق البنفسجية-المرئي (UV-vis). أثبتت تحاليل FTIR و TGA أن أكاسيد المعادن ارتبطت مع مجموعات silanol فيزيائيًا، بينما ارتبط الكركمين مع أكاسيد المعادن المغلفة كيميائيًا. أظهرت تحاليل SAXS و TEM أن مواد الميزوسيليكا المُصنعة باستخدام بوليمرات قصيرة سلسلة EO (أقل من 5 وحدات) تُعطي شكل رقائقي الهيكل (lamellar)، بينما المُصنعة باستخدام بوليمرات متوسطة سلسلة EO (17 -31 وحدة) تُعطي شكل ثنائي الأبعاد سداسي الهيكل (P6mm). كما أثبتت أيضًا أن أكاسيد المعادن المُحملة في الميزوسيليكا المسامية لم تُغير في البُنية الهيكلية لتلك المواد. أكدت تحاليل XRD مدى نقاء المواد المصنعة، و أن متوسط حجم أكاسيد المعادن المغلفة يتغير وفقًا لمواد الميزوسيليكا المسامية المستخدمة. أظهرت تحاليل الأشعة فوق البنفسجية-مرئي (UV-vis) أن نسبة امتصاص الكركمين متنوعة وفقا لأكسيد المعدن المغلف بالميزوسيليكا المسامية المستخدم.

List of tables

List of schemes

List of figures

List of abbreviation and formulas

abbreviation	**Meaning**
3D	3 dimention
B.P	Boiling point
Ca	Calcium
Ca^{+2}	Calcium ion
CaO	Calcium Oxide
C.A.S.	Chemical abstracts service
CMC	Critical micelle concentration
CO_2	Carbon dioxide
CuO	Copper oxide
D.I.W.	Deionized water
DLS	Dynamic light scattering
DTA	Differential thermal analysis
EDX	Energy dispersive X-ray
EO	Ethylene oxide
EPR	Electron paramagnetic resonance
eV	Electron volt
F(F127)	Flake (solid)
Fe^{+3}	Ferric ion
Fig.	Figure
FTIR	Fourier transform infrared
H	Hour
HCl	Hydrochloric acid
HLB	Hydrophilic – Lipophilic Balance
HPLC	High performance liquid chromatography
IUPAC	International union of pure and applied chemistry
λ_{max}	Maximum wave length
L(L-121)	Liquid
LC	Liquid crystal
M	Molar
MAS-NMR	Magic angle spinning-nuclear magnetic resonance

MCM	Mobile crystal mesoporous
meV	Million electron volt
mg	Milli gram
MgO	Magnesium oxide
mL	Milli litter
nm	Nano meter
NPs	Nanoparticles
n-type	Negative- type
O	Oxygen
O^{-2}	Oxygen ion
PL	Photo-luminescence
PO	Propylene oxide
p-type	Positive type
rpm	Round per minute
s	Second
SAXRD	Small angle X-ray diffraction
SAXS	Small angle X-ray scattering
SBA	Santa Barbara university
SEM	Scanning electron microscopy
TEM	Transmission electron microscopy
TEOS	Tetraethoxyorthosilane
TGA	Thermal gravimetric analysis
TLC	Thin layer chromatography
TLCT	True liquid crystal template
UV-vis	Ultraviolet-visible
XPS	X-ray photoelectron spectroscopy
XRD	X-ray diffraction
ZnO	Zinc oxide

Chapter One

Introduction

1.1 Metal oxide nanoparticles

Metal oxides work very essential role in many areas of chemistry, physics and materials science. Metal oxides adopt an infinite number of structural geometries with an electronic structure that can exhibit metallic, semiconductor or insulator character (Fernández-García & Rodriguez, 2011). Metal oxide nanoparticles have been used in a large variety of applications due to their optical, magnetic, and electronic properties. They are used in numerous consumer products such as cosmetics, dental fillings, solar-driven, self-cleaning coatings, textiles and for photo-catalytic degradation of various organic pollutants (Pathakoti *et al.*, 2014). Metal oxides are especially attractive with respect to applications in catalysis, sensing, energy storage, conversion optics, electronic devices, memory arrays, biomedical application and acoustic wave devices (Khalil *et al.*, 2014). The use of solid metal oxides as catalysts is well established. High specific surface area, strong base strength and high concentration of base sites are characteristics of catalyst (Refaat, 2011). Oxide nanoparticles can exhibit unique physical and chemical properties due to their limited size and a high surface area to volume ratio. Since the surface area to volume ratio of particle increases as the particle diameter decreases, nanoparticles with all three external dimensions in the nanoscale, may be more bio-reactive than normal bulk materials (Smijs & Pavel, 2011). Structural and electronic properties drive the physical and chemical properties of the solid. In their bulk state, many oxides have wide band gaps and a low reactivity. A decrease in the average size of an oxide particle change the magnitude of the band gap, with strong influence in the conductivity and chemical reactivity (Fernández-García & Rodriguez, 2011). Engineered metal oxide nanoparticles are finding increasing utility in the medical field ranging from use as antimicrobial agents to diagnostic imaging and potential cancer treatment. While scaling down the size of materials to the nanometer scale gives useful traits, they are within a size range to interact with bio-molecules, such as proteins and nucleic acids (Wehmas *et al.*, 2015).

1.2 Calcium oxide nanoparticles

Calcium oxide (CaO) is an important material because of its application as catalyst and effective chemisorbents for numerous materials (Mirghiasi *et al.*, 2014). There are mainly two methods on the preparation of nano-CaO according to the literatures. One is thermal decomposition (Tang *et al.* 2008), and the other is sol–gel (Ghiasi &

Malekzadeh, 2012). CaO nanoparticles can be obtained about 4 nm through sol–gel method, the cost is very high, the process is very complicated and time-consuming. Therefore, it is very difficult to apply sol–gel method into industry. Thermal decomposition method has some advantages such as simple process, low cost, easiness to obtain high purity product, etc. Therefore, it is promising and facile to be applied into industry (Tang *et al.* 2008). CaO as an alkaline earth metal oxide have several applications such as catalyst, toxic-waste remediation agent, additive in refractory, doped material to modify electrical and optical properties, crucial factor for CO_2 capture, flue gas desulfurization and pollutant emission control (Aguilera-Camacho, 2015; Mirghiasi *et al.*, 2014; Tang *et al.* 2008). The increased catalytic activity of CaO nanoparticles over the bulk CaO is attributed to the higher surface area of nanomaterials. CaO nanoparticles show highly effective catalytic behavior, because of surface properties, including acidity by Ca^{2+} and basicity by O^{2-} (Safaei-Ghomi *et al.*, 2013). CaO in particular, being cheap, has a high basicity, non-corrosive and economically benign. CaO nanoparticles, as an efficient, non-explosive, eco-friendly, recyclable and easy to handle catalyst, are used in the catalysis of many organic transformations.

1.3 Magnesium oxide nanoparticles

Magnesium oxide (MgO) is an attractive basic metal oxide that has many applications. MgO as a versatile oxide material with assorted properties finds extensive applications in catalysis, ceramics, antibacterial materials, toxic waste remediation, or as an additive in refractory, paint and superconductor products (Dhal *et al.*, 2015; Maoz *at al.*, 2011; Mohandes *et al.*, 2010). MgO has been extensively used in various applications owning to its unique optical, electronic, magnetic, thermal, mechanical and chemical properties (Mageshwari *et al.*, 2013; Verma *et al.*, 2014). MgO with ultrafine, nanoscale particles and high specific surface area have shown great promise as destructive adsorbent for toxic chemical agents (Ramanujam & Sundrarajan, 2014). It exhibits a rock salt structure like oxides of other alkaline earth metals. The non-polar (100) face is by far the most stable surface, and particles of MgO usually display a cubic shape (Fernández-García & Rodriguez, 2011; Meenakshi, 2012). The large surface area to volume ratio and the presence of reactive sites on the surface make MgO nanoparticles suitable for uses in a number of organic heterogeneous catalyst. Other possible fields of application are gas and humidity sensors and cryosurgery, due to low cost, electro-stability, nontoxic, and biodegradable properties of MgO nanoparticles (De Falco *et al.*, 2013; Fernández-García & Rodriguez, 2011). Many different synthetic routes provide nanoscale MgO including sol–gel, hydrothermal/solvothermal, laser vaporization, chemical gas phase deposition, aqueous wet chemical, surfactant methods, and microwave-assisted method (Mohandes *et al.*, 2010; Ramanujam & Sundrarajan, 2014). MgO continues to receive attention due to its interesting properties in bulk as well as in nanoscale and wide ranging applications in microelectronics, heterogeneous catalysis, plasma display panels, etc (Kumar *et al.*, 2011).

1.4 Zinc oxide nanoparticles

Zinc oxide (ZnO) nanoparticles are one of the most attractive metal oxides. ZnO nanoparticles are widely used in paint, pharmaceutical, and cosmetics industries, in addition to biomedicine (Tada-Oikawa *et al.*, 2015). ZnO nanoparticles have gained deep attention due to their wide range of applications in the fields of electronics, light (UV) emission, chemical sensor and personal care products. Endowed with high catalytic efficiency and strong adsorption ability they are also used as key ingredient in sunscreens, rubber processing, wastewater treatment, and as a fungicide (Singh *et al.*, 2014). They are especially attractive due to their small size, large surface to volume ratio, chemically alterable physical properties, unique electrical, thermal and mechanical features. Moreover, ZnO nanoparticles are not only stable and have a longer life than organic-based disinfectants, but also are generally regarded as safe to human beings (Kairyte *et al.*, 2013). ZnO is an n-type semiconductor with wide band gap energy (3.37 eV), a large bond strength, and large excitation binding energy (60 meV) at room temperature (Kundu *et al.*, 2014; Nagajyothi *et al.*, 2015; Talebian *et al.*, 2013). Conventional synthesis of ZnO nanoparticles include sol–gel (Chandran *et al.*, 2014), wet chemical route, microwave method, gas-phase synthesis, microemulsion, dry-casting and micellar templating (Kundu *et al.*, 2014). ZnO nanoparticles have received considerable attention due to their unique antibacterial, antifungal, UV filtering properties, high catalytic and photochemical activity (Ambika & Sundrarajan, 2015).

1.5 Copper oxide nanoparticles

Copper oxide (CuO) is a potential p-type semiconductor and gains considerable attentions due to its optical, electrical, physical, and magnetic properties. CuO with narrow band gap of 1.2 eV is widely used in various applications such as catalysis, solar energy conversion, gas sensor and field emission (Phiwdang *et al.*, 2013). Some methods for the preparation of CuO have been reported such as the sonochemical method (Suleiman *et al.*, 2013), sol-gel technique (Azam *et al.*, 2012; Kshirsagar *et al.*, 2015), aqueous precipitation method (El-Trass *et al.*, 2012; Mustafa *et al.*, 2013), microwave irradiation (Wang *et al.*, 2012) and thermal decomposition (Son *et al.*, 2009). Using CuO nanoparticles with narrow size distribution for these applications would further promote the chemical reactivity of the nanoparticles because as the particle size reduces the surface-to-volume ratio increases, and consequently the number of reactive sites increases. CuO nanoparticles exhibit improved electronic and optical properties compared to their bulk equivalent (Dagher *et al.*, 2014). CuO is an attractive metal oxide semiconductor due to its unique electrical, optical, antibacterial and catalytic properties

1.6 Sol-gel process

Sol-gel process is a method for producing inorganic network materials from metal alkoxide molecules. The common metal alkoxides are the alkoxysilanes. Other alkoxides such as aluminates, titanates, zirconates, and borates are also commonly used in the sol-gel process. The process involves conversion of monomers (alkoxides) into a colloidal particles (sol) and their subsequent network formation (gel). Metal alkoxides are most common because they react readily with water. Sol-gel reactions are a series of hydrolysis and condensation reactions of an alkoxides in presence of acid or base (Young, 2002). Sol-gel reaction is presented in scheme 1.1

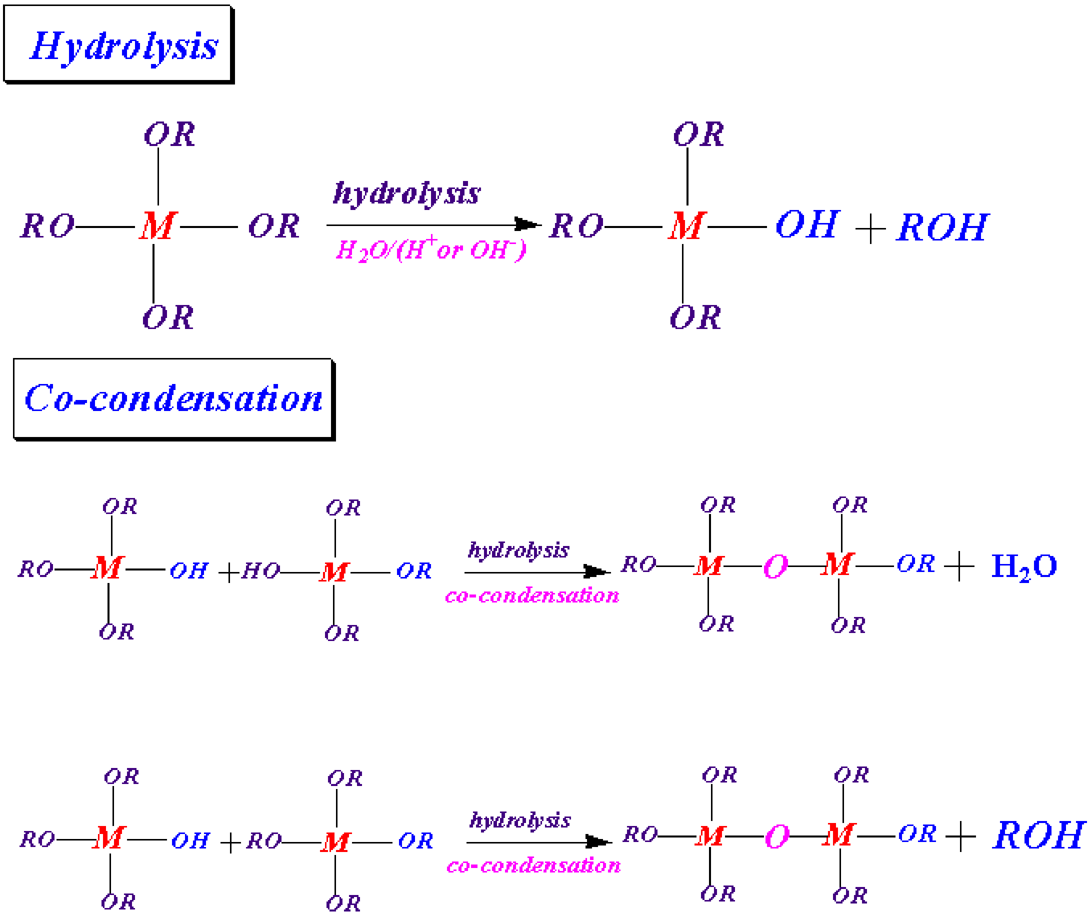

Scheme 1.1 Sol – gel reactions (hydrolysis and co-condensation).

1.7 Mesoporous silica material

Mesoporous materials consist of inorganic metal oxides, like silica or alumina, and have pore sizes in the range of between 2 and 50 nm (Barrabino, 2011). Mesoporous silica materials have attracted attention because of their utilities in adsorption, selective separation and catalysis (Showkat *et al.*, 2007). Mesoporous silica materials with characteristic high surface area, controllable mesostructures and mesopore sizes, coupled with high chemical and thermal stability and availability for surface functionalization could be ideal for a wide range of applications (Waldron *et al.*, 2014). Ordered mesoporous silica-based materials are attractive for the construction of advanced materials on the nanometer scale. The ability to control their structural and textural properties and to functionalize them with organic groups and/or inorganic entities holds the key to their promising applications (Huang *et al.*, 2012). Since the discovery of ordered mesoporous silica materials, there has been a tremendous effort devoted to the control of their nanostructure, texture and macroscopic morphology. The precise control of these characteristics is highly desirable for various purposes and applications in the field of adsorption, separation, catalysis, controlled drug delivery systems, photonic crystals (Sierra *et al.*, 2009). A variety of mesostructured materials exhibiting lamellar, hexagonal (p6mm), 3D hexagonal (P63/mmc) or cubic (Ia3d, Im3m and Pm3n) organizations have already been prepared under different preparative conditions, through a co-condensation of inorganic species, in conjunction with surfactants under acidic or basic conditions (Naik *et al.*, 2004). The most well-known types of silica materials include the silica solids MCM-41 (with a hexagonal arrangement of the mesopores), MCM-48 (with a cubic arrangement of the mesopores), and MCM-50 (with a laminar structure). The use of amphiphilic triblock copolymers as a structure-directing agents has resulted in the preparation of well-ordered hexagonal mesoporous silica structures (SBA-15, SBA: Santa Barbara University) with uniform pore sizes up to approximately 30 nm. Mesoporous silica is synthesized via poly-condensation of silica species, which originate from different sources of silica in the presence of surfactants as structure-directing agents (Hoffmann *et al.*, 2006; Wei *et al.*, 2010). Many types of ionic and non-ionic surfactants have been used for obtaining mesoporous silica with different pore structure and morphological characteristics (Wei *et al.*, 2010). Some of the methods used to synthesize silica nanoparticles are reverse microemulsion and widely sol-gel. In reverse microemulsion, the surfactants molecules dissolved in organic solvents forms spherical micelles. In the presence of water, the polar head groups organize themselves to form micro-cavities containing water. This method was successfully applied for the coating of nanoparticles with different functional groups for various applications (Rahman & Padavettan, 2012). The sol-gel process is widely applied to produce silica, glass, and ceramic materials due to its ability to form pure and homogenous products at mild conditions. Mesoporous materials possess excellent adsorption capacity, due to their large surface area, ordered pore arrangement, uniform pore size and controllable modifying ratio of functional groups (Yang *et al.*, 2008). Mesostructured silica materials with high porosities, well ordered and controlled pore size promised to be potentially useful in catalysis, separation and in optical devices.

1.8 Synthesis of mesoporous silica material

Generally, there are two general mechanisms for synthesis of mesoporous silica materials. These are true liquid-crystal template process (TLCT) and cooperative liquid crystal template process (scheme 1.2).

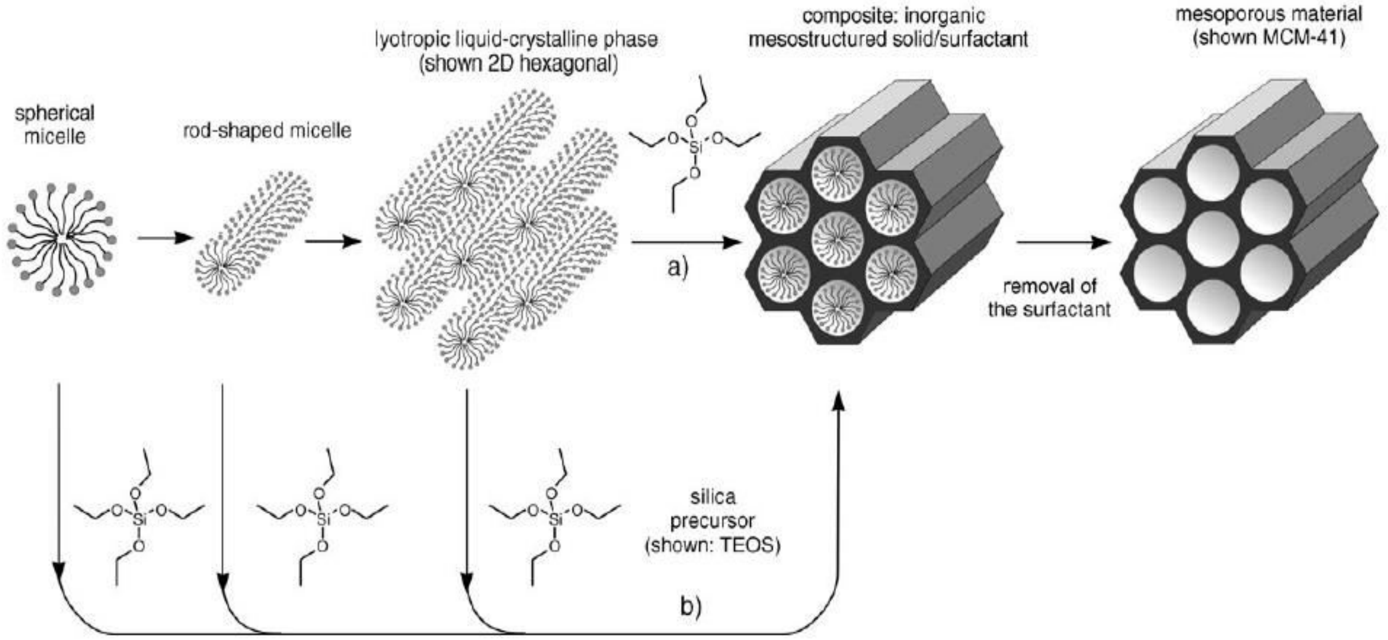

Scheme 1.2 Formation of mesoporous materials by structure-directing agents: a) true liquid-crystal template mechanism and b) cooperative liquid crystal template mechanism (Hoffmann *et al.*, 2006).

1.8.1 Cooperative Self-Assembly Template

The cooperative self-assembly is based on the interactions between the surfactant micelles and silica species that form organic-inorganic mesostructured materials. The cooperative self-assembly can be categorized into four stages, the adsorption of silicates on circular micelles, the association of circular micelles into rods, the precipitation of rods, and the micelle-micelle coalescence. Then the cylindrical micelles come together to form large domains. Simultaneously, the solvent molecules (water) are replaced with silicate species (Sayin, 2010). In the cooperative self-assembly pathway generally, hydrothermal method (80 – 130 ^{o}C) has been employed for the synthesis of mesoporous silica materials.

1.8.2 True Liquid Crystal Template (TLCT)

In the true liquid crystalline template pathway, the liquid crystalline phase is directly used to synthesize ordered mesoporous silica solids (Sayin, 2010). In true liquid-crystal template, the concentration of the surfactant is so high that under the prevailing conditions (temperature, pH) a lypotropic liquid-crystalline phase is formed without requiring the presence of the precursor inorganic framework materials (Hoffmann *et al.,* 2006). The order and the mesostructure of the liquid crystal is mimicked by the inorganic precursors to obtain mesostructured. The condensation reactions of silica precursors around the surfactants, which were in the liquid crystal phase cause the formation of the mesostructured silica. The confined growth of silica species around the surfactants formed the ceramic-like frameworks. The inorganic silica species get their pore structures, pore sizes, and symmetries from the LC frameworks (Sayin, 2010). In general, the first step, is preparing a homogenous solution by dissolving the surfactants in a solvent, water is mostly used as solvent in the synthesis. Then, the silica precursor is added to the reaction media, where the silica precursor undergoes hydrolysis and condensation with the help of acid or base catalyst. The interactions between the surfactant micelles and silica precursors, cooperative self-assembly and the aggregation result in precipitation of mesostructured silica particles. To complete the condensation of silica and to enhance the meso-order, the hydrothermal treatment is usually employed. At the end, the product cooled down to room temperature, washed and dried. The organic surfactants are removed to obtain mesoporous material by calcination or extraction (Hoffmann *et al.*, 2006; Sayin, 2010).

1.9 Types of mesoporous silica structures

Mesoporous silica materials have been synthesized with various mesophase structures include hexagonal, cubic, lamellar (scheme1.3). Amphiphilic block copolymers have emerged as cheap and valuable templates for mesostructured materials possessing long range order (Bagshaw *et al.*, 1995). The tendency for (ethylene oxide)*x*-(propylene oxide)*y*-(ethylene oxide)*x* block copolymers to adopt different structures depending on composition (EO/PO ratio). The length of the EO chains is essential for establishing the mesoporous structure. Polymers with short EO chains (>5 unit) form lamellar structures; with medium length chains (12- 37 units), two-dimensional hexagonal structures are preferentially formed; and long EO chains favor a cubic structure (Kipkemboi *et al.*, 2001).

Table 1.1 mesostructured silica material using triblock copolymer as template.

Surfactant	Surfactant structure	Meso-structure	Reference
L101	$EO_4\ PO_{59}\ EO_4$	Lamellar	Kipkemboi *et al,*, 2001
P103	$EO_{17}\ PO_{59}\ EO_{17}$	Hexagonal	Kipkemboi *et al,*, 2001
P104	$EO_{17}\ PO_{61}\ EO_{27}$	Hexagonal	Kipkemboi *et al,*, 2001
P105	$EO_{37}\ PO_{56}\ EO_{37}$	Hexagonal	Kipkemboi *et al,*, 2001
F108	$EO_{132}\ PO_{50}\ EO_{132}$	Cubic	Kipkemboi *et al,*, 2001
L121	$EO_5\ PO_{70}\ EO_5$	Lamellar	Zhao *et al.*, 1998
F127	$EO_{106}\ PO_{70}\ EO_{106}$	Cubic	Ballem *et al.*, 2010
F88	$EO_{100}\ PO_{39}\ EO_{100}$	Cubic	Zhao *et al.*, 1998
F68	$EO_{80}\ PO_{30}\ EO_{80}$	Cubic	Zhao *et al.*, 1998
P123	$EO_{20}\ PO_{70}\ EO_{20}$	Hexagonal	Flodstrom & Alfredsson, 2003
P103	$EO_{17}\ PO_{85}\ EO_{17}$	Hexagonal	Flodstrom & Alfredsson, 2003
P65	$EO_{20}\ PO_{30}\ EO_{20}$	Hexagonal	Flodstrom & Alfredsson, 2003
L64	$EO_{13}\ PO_{70}\ EO_{13}$	Hexagonal	Zhao *et al.*, 1998
P85	$EO_{26}\ PO_{39}\ EO_{26}$	Hexagonal	Flodstrom & Alfredsson, 2003

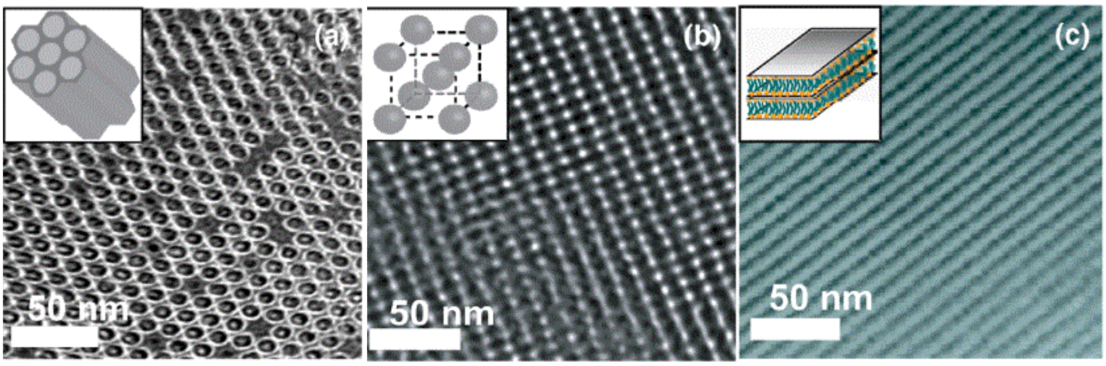

Scheme 1.3 TEM images of (a) hexagonal, (b) cubic, and (c) lamellar mesostructured silicas (Athens *et al.*, 2009).

1.10 Encapsulated metal oxide mesoporous silica

Nanoscience and nanotechnology researches are gradually shifting from the individual component to hybrid, coated and encapsulated nanostructured materials. A large variety of nanostructured materials are made of, or can be coated with silica.

The most advantage of silica is its high surface area to volume ratio, high thermal stability and the broad field of organosilanes available to modify the silica surface with functional groups to give it desired properties (Claesson & Philipse, 2007). Extensive research has been attentive on the highly ordered mesoporous silica SBA-15 due to its tailorable pore size, the high surface area and their potential applications, it seems a long way for them to replace the common micro porous catalysts, and one of the reasons for this delay is their inherent weakness (Wang *et al.*, 2005). Either MCM-41 or SBA-15 consist of only silica and suffer the lack of metal ion so that lack the necessary active species for catalysis. Chemical modification of the pore channels with metal, metal oxides and organic moieties led to new materials with unique physical, chemical and catalytic properties (Lam *et al.*, 2005). Mesoporous silica-coated nano-crystals, which reserve the properties of the functional core, possess a high surface area and pore volume, accessible pore channels, and are favorable for loading fluorophores, drugs and macromolecules (Yang *et al.*, 2011). Properly coated or surface-modified nanoparticles can offer a high potential for numerous applications, due to change of their interfacial characteristic and electrical, magnetic or optical properties (Nikolić *et al.*, 2010).

1.11 Synthesis of encapsulated metal oxide mesoporous silica

Modification of silica mesoporous materials becomes the key step to enable them applied in industry, and many efforts were devoted to prepare the large-pore ordered catalysts with active components, such as metals or metal oxides, organic group and enzymes (Wang *et al.*, 2005). Some of the methods used to synthesize encapsulated metal oxide mesoporous silica are direct synthesis (Lee *et al.*, 2012; Wang *et al.*, 2005) and post modification like impregnation (Furtado *et al.*, 2011; Lee & Chang, 2012; Roggenbuck *et al.*, 2008).

1.11.1 Post modification method (Impregnation)

Encapsulation has been achieved by post synthesis, wet impregnation of metal precursor into the existing mesoporous silica followed by its reduction to metal nanoparticles. The synthesis required multistep procedures susceptible to reducing final yield as well as involving complicated liquid chemistries. Furthermore, metal loading was not easily controllable.

1.11.2 Direct modification method (One-pot or Co-condensation)

Metal salts could be added directly into the precursor solution for mesoporous silica followed by aging in liquid phase, filtration, and final calcination. However, since some metal was lost in filtrate, such incorporation was not so controllable. Direct synthesis attracts most attention because it is timesaving.

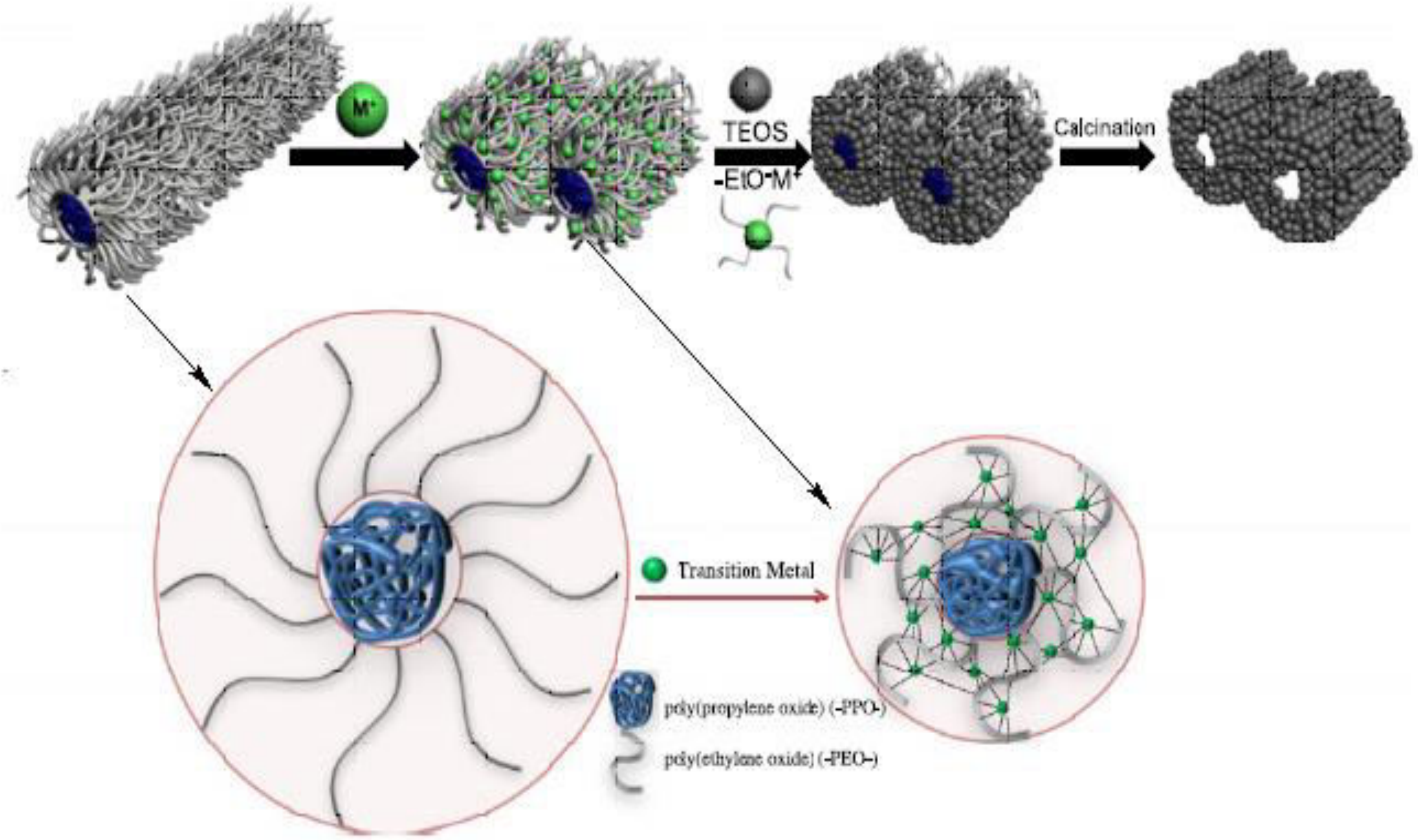

Scheme 1.4 Formation of encapsulated mesoporous silica via one pot synthesis (Lee *et al.*, 2012).

Incorporation of metal nanoparticles in these mesoporous structures has been a very interesting and promising field of research such as catalysis, optics, and photonics.

1.12 Curcumin

Curcumin, 1,7-bis(4-hydroxy-3-methoxyphenyl)-1,6-heptadiene-3,5-dione, is the main yellow bioactive component of turmeric (Curcuma longa), a perennial plant of the ginger family (Zingiberaceae), which is native to tropical South Asia (Patra & Barakat, 2011).

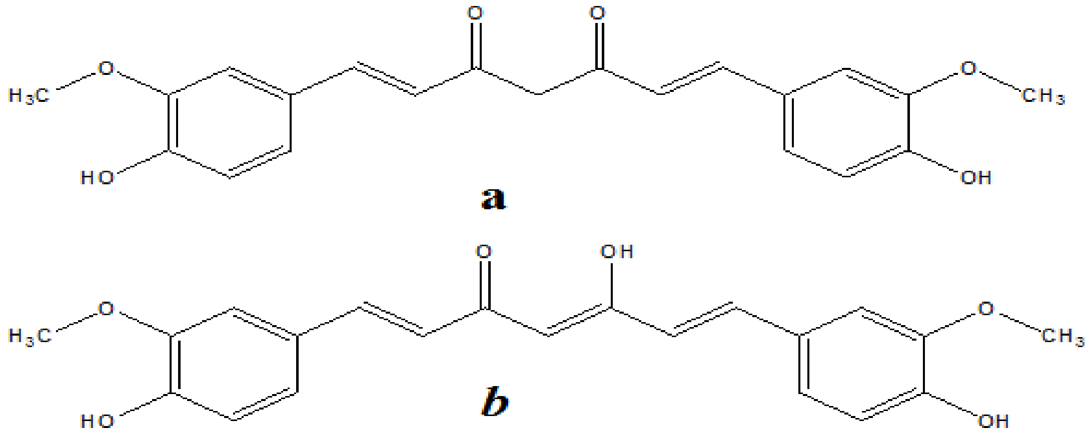

Scheme 1.5 curcumin chemical structure (a) Keto-form and (b) Enol-form.

Table 1.2 Curcumin properties (Patra and Barakat, 2011; Stankovic, 2004).

Properties	**Describtion**
IUPAC name	1,7-Bis-(4-hydroxy-3-methoxyphenyl)-hepta-1,6-diene-3,5-dione diferuloylmethane
Chemical formula	$C_{21}H_{20}O_6$
C.A.S. number	458-37-7
Molecular weight	368.38 g/mol
Appearance	Bright yellow-orange powder
Melting point	183 ^{o}C
Solubilty	Soluble in water at basic pH and organic solvent but insoluble in water at acidic and neutral pH
Color	At pH <1 has red color At pH range 1-7 has yellow color At pH > 7.5 has red color
Stability	Stable at acidic and neutral medium Unstable at basic medium and presence of light
λ_{max} absorption	350-480 nm due to $\pi \rightarrow \pi^*$

Curcumin possesses a variety of biological and pharmacological activities. Recently, curcumin has attracted much interest to researchers because several experimental studies show that this natural polyphenol has anti-inflammatory, anti-oxidant, anti-Alzheimer’s disease, anti-cystic fibrosis, anti-neoplastic, anti-cancer and wound-healing effects, anti-angiogenic activities. Oral take up of curcumin with minimal acute has the great value to overcome these chronic illnesses. Major problem with curcumin for the treatment of diseases is its reduced bioavailability. Curcumin is very soluble in organic solvents, such as ethanol, dimethylsulfoxide, and acetone (Zhu, 2009). Curcumin practically insoluble in water at acidic and neutral pH, soluble in alkali. It is stable at high temperatures and in acids, but unstable in alkaline conditions and in the presence of light ((Ghosh & Mondal, 2012; Stankovic, 2004). The solubility of curcumin in water is reported to be 1.99×10^{-4} mg/mL (Pang *et al.*, 2014). The maximum absorption of curcumin in methanol is at 430 nm and in acetone at 415-420 nm. Usually, curcumin is stable at acidic pH but unstable at basic pH and in the presence of light, under which conditions it is degraded to ferulic acid feruloylmethane. Curcumin is more stable in human blood and no more than 20% of curcumin being degraded within 1 hour and approximately 50% by 8 hours. The major degradation product of curcumin is trans-6-(40-Hydroxy-30-methoxyphenyl)-2,4-dioxo-5-hexenal, while the minor degradation products are vanillin, ferulic acid and feruloylmethane (Zhu, 2009). Curcumin is produced by several methods. Curcumin was synthesized by the condensation of vanillin substituted by acetyl acetone (Subhan *et al.*, 2013). Curcumin was extracted from turmeric by magnetically stirred and heated under reflux (Anderson *et al.*, 2000; Subhan *et al.*, 2013), by soxhlet extractor (Kulkarni *et al.*, 2012) and by column extraction using different organic solvent (Popuri & Pagala, 2013). Curcumin continues to receive attention due to its potential pharmaceutical importance.

1.13 Literature review

1.13.1 Mesoporous silica

During last years, interest of mesoporous silica materials has increased due to benefits that these materials can offer. Mesoporous silica materials, discovered in 1992 by the Mobile Oil Corporation, have received considerable attention due to their superior textual properties such as high surface area, large pore volume, tunable pore diameter, and narrow pore size distribution. Mesoporous silica is so special due to its uses as biocompatible, stimuli-responsive drug delivery devices. Several types of ionic and non-ionic surfactants have been used for synthesis of mesoporous silica with different pore structure and morphological characteristics. Using amphiphilic triblock copolymers as structure-directing agents under acidic condition has resulted in the preparation of well-ordered hexagonal mesoporous silica structures (SBA-15) with uniform pore sizes up to approximately 30 nm (Hoffmann *et al.*, 2006; Wei *et al.*, 2010). Flodstrom and Alfredsson (Flodström & Alfredsson, 2003) have investigated the effect of different block lengths of Pluronic surfactants, (EO)x–(PO)y–(EO)x, in the formation of mesoporous silica. The syntheses were performed in micellar solution of the surfactant under acidic conditions. The materials were characterized by SAXS, TEM and nitrogen adsorption measurements. Higgins *et al.* (Higgins *et al.*, 2006) have reported on the preparation and characterization of mesoporous silica membranes via micellar templating using the non-ionic $(EO)_{20}$–$(PO)_{70}$–$(EO)_{20}$ surfactant, Pluronic P123, as a template under various template/silica volume percentages ($V_{TS\%}$). Mesa, Sierra and Guth (Mesa *et al.*, 2008) have investigated the evolution of the micelles of two triblock copolymer surfactants, Pluronic F127 and Pluronic P123, in diluted aqueous reaction mixtures during the formation of SBA-16 and SBA-15 at different temperatures, acid and salt concentrations using DLS, respectively. Chen *et al.* (Chen *et al.*, 2011) have studied the use of block copolymer (BCP) nonionic surfactant mixtures (including Pluronic, Brij and Tetronic types) as templates for synthesizing porous silica materials of mixed pore sizes. Benamor *et al.* (Benamor *et al.*, 2012) have studied the identification of parameters governing structural, textural properties and hydrophilic/hydrophobic balance of SBA-15 type ordered mesoporous silica by the study of the influence of the temperature and the stirring at the ripening step (first synthesis step), the duration of the two principal synthesis steps (ripening and aging). In addition, the heating process at the aging step. The synthesis medium has been analyzed by dynamic light scattering (DLS), both the as-synthesized and calcined SBA-15 ordered mesoporous solids have been characterized by small angle X-ray diffraction (SAXRD), nitrogen sorption experiments, scanning and transmission electron microscopy (SEM/TEM) and ^{29}Si magic-angle spinning (MAS) NMR spectroscopy. Benamor *et al.* (Benamor *et al.*, 2012) have reported a new rapid calcination method that has been used to completely remove the organic template from SBA-15 ordered mesoporous silica, and to preserve a high number of silanol in these materials.

1.13.2 Encapsulated metal oxide mesoporous silica

Chemical modification of the pore channels of mesoporous silica with metal and metal oxides led to new materials with unique physical, chemical and catalytic properties. Wang *et al.* (Wang *et al.*, 2005) have studied the in situ coating process of

MgO or CuO on SBA-15. Metal oxide-modified SBA-15 functional mesoporous materials can be directly synthesized through adding simple precursor salts into the synthetic system, recovering the composites via evaporation and subsequent calcination. Barreca *et al.* (Barreca *et al.*, 2007) have investigated the deposition of iron oxide nanoparticles on the exterior of and inside the pores of hexagonal mesoporous silica by a direct synthesis technique with iron phthalocyanine as precursor. Lu *et al.* (Lu *et al.*, 2009) have studied the employing of the two-solvent method to prepare ZnO encapsulated in mesoporous silica (ZnO/SBA-15). The prepared ZnO/SBA-15 samples have been studied by XRD, TEM, XPS, nitrogen sorption isotherm, and PL spectroscopy. The ZnO/SBA-15 nanocomposite has the ordered hexagonal mesostructure of SBA-15. ZnO clusters of a high loading are distributed in the channels of SBA-15. ZnO clusters encapsulated in SBA-15 can be used as light-emitting diodes and ultraviolet nanolasers. Huang *et al.* (Huang *et al.*, 2010) have studied the developing of a modified CaO-based mesoporous CO_2 sorbent with high sorption capacity. Highly ordered mesoporous SBA-15 molecular sieves used as carriers were successfully synthesized through direct-synthesis by using non-ionic surfactants as the structure-directing agent under strong acidic conditions. Calcium ions using calcium acetate as the precursor were finely dispersed onto prepared carriers using an impregnation method. Calcium oxide was obtained under calcination at high temperature. Analytical techniques, such as XRD, nitrogen physisorption isotherms, SEM/EDX and TEM, were used to characterize the synthesized mesoporous materials.

1.13.3 Curcumin

Curcumin has received ample attention as potential drug because of potential pharmaceutical applications as an antioxidant, anti-inflammatory and anti-carcinogenic agent (Patra & Barakat, 2011), anti-Alzheimer’s disease, anti-cystic fibrosis, anti-neoplastic, and wound-healing effects, anti-angiogenic activities (Zhu, 2009). Different methods have been reported to produce curcumin. Anderson *et al.* (Anderson *et al.*, 2000) and Subhan *et al.* (Subhan *et al.*, 2013) have extracted curcumin from turmeric using dichloromethane, which was heated under reflux for 1 h, then the reddish yellow oily residue was triturated with hexane and the resulting solid was collected by suction filtration. Kulkarni *et al.* (Kulkarni *et al.*, 2012) have extracted curcumin from turmeric by soxhlet extractor using different organic solvent such as chloroform (B.P. =61˚c), ethyl acetate, methanol and acetone. Isolation and purification of curcumin was carried out by column chromatography. Subhan *et al.* (Subhan *et al.*, 2013) have synthesized curcumin by the condensation of vanillin substituted by acetyl acetone. Popuri and Pagala (Popuri & Pagala, 2013) have extracted curcumin from turmeric by column extraction using different organic solvent such as acetone, ethanol, methanol, isopropanol and ethyl acetate. And then distillation is performed to separate the mixture of solvent and solute.

Curcumin is very poorly soluble in water which reducing its effectiveness as a drug. For that reason, various methods are being developed to enhance curcumin solubility and effectiveness of the drug during its delivery. Bahawana *et al.* (Bahawana *et al.*, 2011) have developed a method for the preparation of nanoparticles of curcumin with a view to improve its aqueous-phase solubility and examine the effect on its antimicrobial properties. Nanoparticles of curcumin (nanocurcumin) were prepared by a process based on a wet-milling technique and were found to have a narrow particle size distribution in the range of 2- 40 nm. Unlike curcumin, nanocurcumin was found to be freely dispersible in water in the absence of any surfactants. The chemical structure of nanocurcumin was the same as that of curcumin, and there was no modification during nanoparticle preparation. Modasiya & Patel (Modasiya & Patel, 2012) have studied increasing solubility of curcumin as drug using solid dispersion technique. The solid binary systems were prepared using different drug: polymer ratio (1:1, 1:4 and 1:8) with polyethylene glycol 4000 and 6000 by different techniques like physical mixing, melting method and solvent evaporation method. PVP K 30 was also used as a polymer. The formulations were characterized by SEM, thin layer chromatography (TLC), compatibility study, diffraction study and *in vitro* dissolution rate studies.

Several methods have been proposed to characterize and determine the concentration of curcumin and its derivatives in curcumin products. Gupta *et al.* (Gupta *et al.* , 2010) have developed a precise, accurate, sensitive and reliable method for determination of low concentrations of curcumin, using spectrofluorimetry. A standard curve of curcumin was prepared in methanol and serum in the concentration range 1-10 ng/ml. The method was validated in terms of linearity, accuracy and precision. Curcumin was also estimated in rat serum after oral administration of curcumin at a dose of 100 mg/kg. Hemish *et al.* (Hemish *et al.*, 2011) have investigated the quantitative and qualitative determination of curcumin in Ethanolic extract of curcuma longa. Qualitative estimation was carried out by TLC method. The simultaneous quantitative determination of curcumin was carried out by spectrophotometric and HPLC technique. Panigoro and Dhianawaty (Panigoro & Diah Dhianawaty, 2013) have evaluated the curcumin concentrations in fresh and decoction of dried rhizome as homemade jamu. Concentrations of curcumin were measured with spectrophotometer at wavelength 418 nm. Thejeswari *et al.* (Thejeswari *et al.*, 2013) have studied the qualitative identification and separation of curcuminoids from *C. longa* by various analytical methods. The drug Curcumin was characterized by spectroscopic methods like IR, UV and Thin layer chromatographic studies. The TLC studies performed with various solvents of different polarities were pre-tested for the separation of curcumin. *Ge et al.* (*Ge et al.*, 2014) have studied the interaction between curcumin and its derivatives (demothxycurcumin and bisdemethoxycurcumin) with human serum albumin that has been carried out using multi-spectroscopic analysis and molecular modeling method. The characteristic of fluorescence quenching and the thermodynamic parameters have been studied by state emission fluorescence experiments under different temperatures with an interval of 6 Kelvin. Yue *et al.* (Yue *et al.*, 2014) have studied the detection property of natural drug-curcumin as an excellent UV–vis Furthermore, the ability of probe to detect ClO^- in living cells was also evaluated. Chatterjee *et al.* (Chatterjee *et al.*, 2014) have investigated the antioxidant and also the antimicrobial activity of curcumin when impregnated on wheat flour under normal home storage conditions. Saithongdee *et al.* (Saithongdee *et al.*, 2014) have synthesized zein membrane containing curcumin, which fabricated by electro-spinning and a subsequent heat induced amide crosslinking reaction by using citric acid as crosslinker. Curcumin-loaded zien membrane was evaluated as a new optical sensor for Fe^{3+} ions. The concentration of Fe^{3+} in aqueous solution was determined by naked eye detection after dipping the membrane into the sample solution. Ak and Gülçin (Ak and Gülçin, 2008) have determined the antioxidant activity of curcumin by employing various in vitro antioxidant assays such as 1,1-diphenyl-2-picryl-hydrazyl free radical (DPPH•) scavenging, 2,2-azino-bis(3-ethylbenzthiazoline-6-sulfonic acid) (ABTS) radical scavenging activity, *N*,*N*-dimethyl-*p*-phenylene diamine dihydrochloride (DMPD) radical scavenging activity. Hussien *et al.* (Hussien *et al.*, 2015) have evaluate the potential role of curcumin supplementation in attenuating the aggressive effect of alcohol in experimental induced gastric ulcer. Zebib *et al.* (Zebib *et al.*, 2010) have studied the stabilization of curcumin food pigment by its complexation with divalent ions like (Zn^{2+},Cu^{2+},Mg^{2+}, Se^{2+}), in “green media” and evaluate its stability in vitro compared to curcumin alone. The curcumin complexes were prepared by mechanical mixture of curcumin and sulfate salts of each metal (metal:curcumin 1/1mol) into unconventional and nontoxic glycerol/water solvent. Kanhathaisong *et al.* (Kanhathaisong *et al.*, 2011) have determined the stoichiometric composition of the curcumin–Cu (II) complex formed between curcumin and the Cu (II) ion in an aqueous solution. The complex formation between curcumin dyes and the Cu (II) ion were investigated by using the UV-Vis spectrophotometry method. Zhao *et al.* (Zhao *et al.*, 2010) have synthesized curcumin complexes with Zn^{2+} and Cu^{2+} ions. Curcumin complexes with Zn^{2+} and Cu^{2+} ions were characterized by elemental analysis, mass spectroscopy, IR spectroscopy, UV spectroscopy, solution ^{1}H and solid-state ^{13}CNMR spectroscopy, EPR spectroscopy. In addition, the density functional theory (DFT) based UV and ^{13}C chemical shift calculations were also performed to view insight into those compound structures and properties. Das (Das, 2011) has investigated the synthesis and characterization of curcumin-silica organic-inorganic hybrid materials. The preparation of the hybrid materials via covalent incorporation of the organic curcumin phase into the pre-hydrolyzed sol-gel silicate phase. The degree of incorporation of curcumin phase was verified by thermogravometric analysis (TGA). Material was characterized using FTIR, DSC and fluorescence spectroscopic techniques. The inorganic-organic silica hybrid materials may find wide applications in implant and other biomedical materials with reduced inflammatory properties. Gangwar *et al.* (Gangwar *et al.*, 2013) have studied the conjugation of curcumin with silica nanoparticles to improve its aqueous solubility and hence to make it more bioavailable. Conjugation and loading of curcumin with silica nanoparticles was further examined with TEM and TGA. Cytotoxicity analysis of synthesized silica:curcumin conjugate was studied against HeLa cell lines as well as normal fibroblast cell lines. Silica:curcumin conjugate has great potential for anticancer application.

Here in, we prepare mesoporous silica materials with new amphiphilic triblock copolymer as structure directing agent and determine their characters. Modification of their surface using four different metal oxides with impregnation method. Then, we use these materials as carrier for curcumin drug. Curcumin is a very important drug for cancer and Alzheimer diseases.

1.14 Aims of the present work

In this thesis, CuO/SiO_2, ZnO/SiO_2, CaO/SiO_2 and MgO/SiO_2 are used to synthesize curcumin-metal/SiO_2 complexes, which enhance curcumin solubility and its biological and pharmacological activities.

The present study has focused on the following:

1. Synthesis of mesoporous silica using nonionic triblock copolymer (Pluronic) surfactants (P123, L81, L61 and L31).
2. Synthesis of CuO/SiO_2, ZnO/SiO_2, CaO/SiO_2 and MgO/SiO_2 via impregnation method.
3. Synthesis of curcumin–Cu(II)/SiO_2, curcumin–Zn(II)/SiO_2, curcumin–Ca(II)/SiO_2 and curcumin–Mg(II)/SiO_2 complexes.
4. Determination of structural properties of mesoporous silica, CuO/SiO_2, ZnO/SiO_2, CaO/SiO_2, MgO/SiO_2, curcumin–Cu(II)/SiO_2, curcumin–Zn(II)/SiO_2, curcumin–Ca(II)/SiO_2 and curcumin–Mg(II)/SiO_2 complexes using fourier transform infrared spectroscopy (FTIR), X-ray diffraction (XRD), small angle X-ray scattering (SAXS), transmission electron microscope (TEM) and thermal gravimetric analysis (TGA) .
5. Determination of CuO/SiO_2, ZnO/SiO_2, CaO/SiO_2 and MgO/SiO_2 ability in curcumin uptake using optical absorption.

Chapter Two

Experimental

2.1 Materials

All the used chemicals were analytical grade and directly used as received without further purification. Triblock copolymer Pluronic L61 (EO_2 PO_{31} EO_2), Pluronic L81 (EO_3 PO_{43} EO_3), Pluronic L31 (EO_2 PO_{16} EO_2), Pluronic P123 (EO_{20} PO_{70} EO_{20}), Tetraethoxyorthosilane (TEOS) ($Si(OC_2H_5)_4$), absolute ethanol (C_2H_6O), copper acetate mono-hydrate ($Cu(CH_3COO)_2.2H_2O$) were purchased from Aldrich Company and used without further purification. Magnesium acetate tetra-hydrate ($Mg(CH_3COO)_2.4H_2O$), curcumin ($C_{21}H_{20}O_6$) were purchased from Sigma-Aldrich Company and used without further purification. Zinc acetate di-hydrate ($Zn(CH_3COO)_2.2H_2O$), calcium carbonate ($CaCO_3$) were purchased from Sigma Company. Acetic acid (CH_3COOH) and hydrochloric acid (HCl) were purchased from Merck Company. All the glassware used in this experimental work washed with nitric acid (HNO_3) then with distilled water and dried at 100 °C.

Table 2.1 Triblock copolymer (Pluronic) surfactants properties (Kabanov *et al.*, 2002; Krupka & Exner, 2011).

Properties	**Pluronic P123**	**Pluronic L81**	**Pluronic L61**	**Pluronic L31**
Chemical formula	EO_{20} PO_{70} EO_{20}	EO_3 PO_{43} EO_3	EO_2 PO_{31} EO_2	EO_2 PO_{16} EO_2
Molecular weight	5750 g/mol	2750 g/mol	2000 g/mol	1100 g/mol
HLB	6	2	3	3.2
CMC	$4.4 * 10^{-6}$ M	$2.3 * 10^{-5}$ M	$1.1 * 10^{-4}$ M	N/A
Cloud point (1%) aquous solution	90 °C	20 °C	24 °C	39 °C
Toxicity	Non-toxic	Non-toxic	Non-toxic	Non-toxic
Appearance	slightly milky, cloudy past	slightly milky, cloudy liquid	slightly milky, cloudy liquid	slightly milky, cloudy liquid

2.2 Synthesis of mesoporous silica

In typical synthesis of mesoporous silica (Zhao *et al.*, 1998), (4 g, 0.695 mmol, 1.45 mmol, 2 mmol, 3.6 mmol) of nonionic tri-block copolymer Pluronic surfactant (P123, L81, L61 and L31) was dispersed in (40 mL) of deionized water (D.I.W) under stirring, respectively. In some surfactant (L81, L61 and L31), the solution was kept at low temperature for 1 h until the solution becomes clear. Then (60 mL) of 2 M HCl was added slowly to the surfactant solution under the same conditions for another hour. The (8.8 mL, 39.4 mmol) of TEOS was added to previous mixture dropwisely under the same conditions. The mixture was put under stirring at room temperature for 24 h. Then, the mixture was transfer to sealed autoclave bottle at 100 ℃ for 48 h in oven. The product was filtrated, washed twice with deionized water (D.I.W). Dry in oven at 100 ℃ for 24 h. The materials were calcinated in furnace at 500 ℃ for 3 h. The synthesized materials are labeled as in Table 2.2

Table 2.2 Synthesized mesoporous silica label

Surfactant	Labeled product
Pluronic P123	SiO_2-P123 (SBA-15)
Pluronic L81	SiO_2-L81
Pluronic L61	SiO_2-L61
Pluronic L31	SiO_2-L31

2.3 Synthesis of encapsulated metal oxides/mesoporous silica (MO/SiO_2) via impregnation method

2.3.1 Synthesis of CaO/SiO_2 nanocomposites

This material was prepared as previously reported (Furtado *et al.*, 2011; Lee & Chang, 2012). The CaO/SiO_2 (30 % (wt. /wt.)) nanocomposite was synthesized by adding (0.54 g, 5.4 mmol) of $CaCO_3$ to (50 mL, 0.22 M) of acetic acid. The solution was added to 0.7 g of each mesoporous silica. The mixture was stirred for 2 hours at room temperature, then heated to 80 ℃ under stirring to dryness. The final product was then dried in oven at 100 ℃ overnight. The material was then calcinated at 600 ℃ for 4 hours. The materials were labeled as CaO/SiO_2-P123 (SBA-15), CaO/SiO_2-L81, CaO/SiO_2-L61 and CaO/SiO_2-L31.

2.3.2 Synthesis of MgO/SiO_2 nanocomposites

This material was prepared as previously reported (Furtado *et al.*, 2011; Lee & Chang, 2012). The MgO/SiO_2 (30 % (wt. /wt.)) nanocomposite was synthesized by dissolving (1.61 g, 7.5 mmol) of $Mg(CH_3COO)_2.4H_2O$ in 50 mL of deionized water (D.I.W.). The solution was added to 0.7 g of each mesoporous silica. The mixture was stirred for 2 hours at room temperature, then heated to 80 ℃ under stirring to dryness. The final product was then dried in oven at 100 ℃ overnight. The material was then calcinated at 600 ºC for 4 hours. The materials were labeled as MgO/SiO_2-P123 (SBA-15), MgO/SiO_2-L81, MgO/SiO_2-L61 and MgO/SiO_2-L31.

2.3.3 Synthesis of CuO/SiO_2 nanocomposites

This material was prepared as previously reported (Furtado *et al.*, 2011; Lee & Chang, 2012). The CuO/SiO_2 (30 % (wt./wt.)) nanocomposite was synthesized by dissolving (0.75 g, 3.8 mmol) of $Cu(CH_3COO)_2.2H_2O$ in 50 mL of deionized water (D.I.W.). The solution was added to 0.7 g of each mesoporous silica. The mixture was stirred for 2 hours at room temperature, then heated to 80 ºC under stirring to dryness. The final product was then dried in oven at 100 ºC overnight. The material was then calcinated at 600 ºC for 4 hours. The materials are labeled as CuO/SiO_2-P123 (SBA-15), CuO/SiO_2-L81, CuO/SiO_2-L61 and CuO/SiO_2-L31.

2.3.4 Synthesis of ZnO/SiO_2 nanocomposites

This material was prepared as previously reported (Furtado *et al.*, 2011; Lee & Chang, 2012). The ZnO/SiO_2 (30 % (wt./wt.)) nanocomposite was synthesized by dissolving (0.81 g, 3.7 mmol) of $Zn(CH_3COO)_2.2H_2O$ in 50 mL of deionized water (D.I.W.). The solution was added to 0.7 g of each mesoporous silica. The mixture was stirred for 2 hours at room temperature, then heated to 80 ºC under stirring to dryness. The final product was then dried in oven at 100 ºC overnight. The material was then calcinated at 600 ºC for 4 h. The materials are labeled as ZnO/SiO_2-P123 (SBA-15), ZnO/SiO_2-L81, ZnO/SiO_2-L61 and ZnO/SiO_2-L31.

2.4 Preparation of curcumin solutions for standard curve

0.1 g of curcumin was dissolved in 100 mL of absolute ethanol to prepare $2.71*10^{-3}$ M curcumin solution. Then, 2.214 mL of the previous curcumin solution was diluted to 100 mL with absolute ethanol to prepare $6*10^{-5}$ M stock solution. Then, different curcumin concentrations ((6, 5.4, 4.8, 4.2, 3.6, 3, 2.4, 1.8, 1.2 and 0.6) $*10^{-5}$ M) were prepared from stock solution.

2.5 Synthesis of curcumin–metal(II) complexes/SiO_2

The curcumin uptake by each metal oxide/SiO_2 composite was determined. Ethanolic curcumin solution ($6*10^{-5}$ M) was used. 0.2 g of encapsulated metal oxide/SiO_2 was shaking with 25 mL of ethanolic curcumin solution for 72 hours. Then, curcumin–metal(II) complexes/SiO_2 separated by centrifuge (3500 rpm for 15 minute), washed with 5 mL ethanol and dried at 80 ^{o}C. The amount of curcumin absorbs can be calculated as uptake percentage. The results are discussed in Chapter 5.

Table 2.3 synthesized curcumin–metal(II) complexes/mesoporous silica.

Metal oxide encapsulated silica	curcumin–metal(II)/mesoporous silica complexes label
CaO/SiO_2-P123 (SBA-15)	Curc-Ca(II)/SiO_2-P123 (SBA-15)
CaO/SiO_2-L81	Curc-Ca(II)/SiO_2-L81
CaO/SiO_2-L61	Curc-Ca(II)/SiO_2-L61
CaO/SiO_2-L31	Curc-Ca(II)/SiO_2-L31
MgO/SiO_2-P123 (SBA-15)	Curc-Mg(II)/SiO_2-P123 (SBA-15)
MgO/SiO_2-L81	Curc-Mg(II)/SiO_2-L81
MgO/SiO_2-L61	Curc-Mg(II)/SiO_2-L61
MgO/SiO_2-L31	Curc-Mg(II)/SiO_2-L31
CuO/SiO_2-P123 (SBA-15)	Curc-Cu(II)/SiO_2-P123 (SBA-15)
CuO/SiO_2-L81	Curc-Cu(II)/SiO_2-L81
CuO/SiO_2-L61	Curc-Cu(II)/SiO_2-L61
CuO/SiO_2-L31	Curc-Cu(II)/SiO_2-L31
ZnO/SiO_2-P123 (SBA-15)	Curc-Zn(II)/SiO_2-P123 (SBA-15)
ZnO/SiO_2-L81	Curc-Zn(II)/SiO_2-L81
ZnO/SiO_2-L61	Curc-Zn(II)/SiO_2-L61
ZnO/SiO_2-L31	Curc-Zn(II)/SiO_2-L31

2.6 Characterization technique

2.6.1 Thermal gravimetric analysis (TGA)

Thermal gravimetric Analysis (TGA) was carried out using Melter Toledo SW 7.01 analyzer of 25-600 °C under nitrogen with rate 10 °C/1 minute.

2.6.2 Fourier transform infrared (FTIR)

FTIR spectra were recorded using a Fourier transform infrared spectrophotometer (Frontier Perkin Elmer); The samples were measured on a Zinc Selenide Crystal, it is working as a Multiple Reflection ATR system (Attenuated total Reflection).

2.6.3 Ultraviolet-Visible spectroscopy (UV-vis)

Ultraviolet–visible absorption spectra were recorded on a UV-vis spectrophotometer Shimadzu, UV-2400 in the wavelength range from 200 to 800 nm.

2.6.4 X-ray diffraction analysis (XRD)

Powder X-ray diffraction (XRD) patterns was recorded on Analytical Expert Pro diffractometer utilizing Cu Kα radiation (k = 1.54 Å) and within the 2 h range of 10 –

80 in a step size of 0.0130 and scan step time of 29.07 s.

2.6.5 Transmission electron microscopy (TEM)

TEM analysis was performed with JEM2010 (JEOL) transmission electron microscope with energy-dispersive X-ray spectrometer INCA (Oxford Instruments).

2.6.6 Small angle X- ray scattering (SAXS)

Small angle X-ray scattering (SAXS) patterns was recorded on Analytical Expert Pro diffractometer utilizing Cu Ka radiation (k = 1.54 Å) within the 2 h range of 0.5–5 ^{o} in step size of 0.02 ^{o} and scan step time of 86.19 s.

Chapter Three

Results and Discussion

Synthesis and characterization of mesoporous silica materials.

3.1 Introduction

Some of the used methods to synthesize silica materials are sol-gel process, reverse microemulsion, and flame synthesis. The sol-gel process is widely used to produce pure silica particles due to its ability to control the particle size, size distribution and morphology through systematic monitoring of reaction parameters (Rahman & Padavettan, 2012). Generally, the formation process of these materials using structure-directing agent have prepared in two different mechanisms. Firstly by liquid-crystal template mechanism and secondly, by cooperative liquid crystal template mechanism (Hoffmann *et al.*, 2006). The type of surfactant plays a crucial rule in the synthesis, since its effect on the morphology of the formed materials is probably high, where wide variety of different surfactants can be used. The main surfactant used in synthesis of mesoporous is non-ionic block copolymers (Barrabino, 2011). In our present research thesis, we used four different triblock copolymer surfactants, where they have different (EO/PO) ratio and the PO chain length. We have used TEOS as silica precursor. We have used first mechanism, where triblock copolymer surfactants were firstly dispersed in water under acidic medium with concentration above CMC to form like-crystalline shape, followed by addition of TEOS under stirring and certain temperature. Hydrothermal process was also take place at fixed time and temperature. Different four mesoporous silica materials with four different triblock copolymer surfactants were synthesized. Several methods and techniques were used to examine their structural properties. These methods include fourier transform infrared spectroscopy (FTIR), X-ray diffraction (XRD), small angle X- ray scattering (SAXS), transmission electron microscopy (TEM) and thermal gravimetric analysis (TGA).

3.2 Synthesis

Mesoporous silica was prepared using Pluronic P123 surfactant as in literature (Zhao *et al.*, 1998) labeled as SiO_2-P123 (SBA-15). P123 surfactant was dispersed in water under acidic medium to form like-crystalline shape. TEOS acts as silica precursor was added to the solution to undergo hydrolysis and co-condensation to get silica network. Hydrothermal treatment was carried out to induce the complete condensation and solidification and improve the organization of silica network. Calcination was took place to remove surfactant (Scheme 3.1).

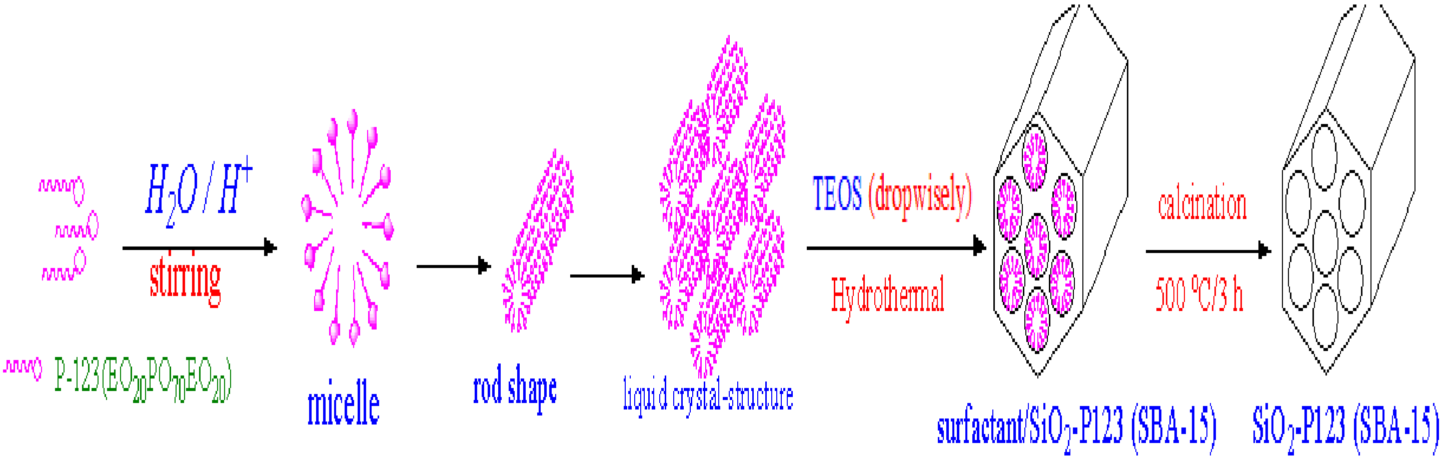

Scheme 3.1 Synthesis of SiO_2-P123 (SBA-15)

Mesoporous silica materials were also prepared using Pluronic L81, L61 and L31 surfactants in the same way as SiO_2-P123 (SBA-15) (Zhao *et al.*, 1998). The mesoporous silica obtained materials were labeled as in Table 2.2. Copolymer surfactants could not form a rod-like micelle because of the short chain EO block copolymers of Pluronic L81, L61 and L31 surfactants. Different micelle shape of lamellar structure is probably obtained (Kipkemboi *et al.*, 2011). The silica precursor (TEOS) was added to the solution to undergo hydrolysis and co-condensation to get silica network. The silica obtained using Pluronic L81, L61 and L31 present weak pore-order as that of SiO_2-P123 (SBA-15). Hydrothermal treatment was carried out to induce the complete condensation and solidification and improve the organization of silica network. Calcination was carried out to remove surfactant (Scheme 3.2).

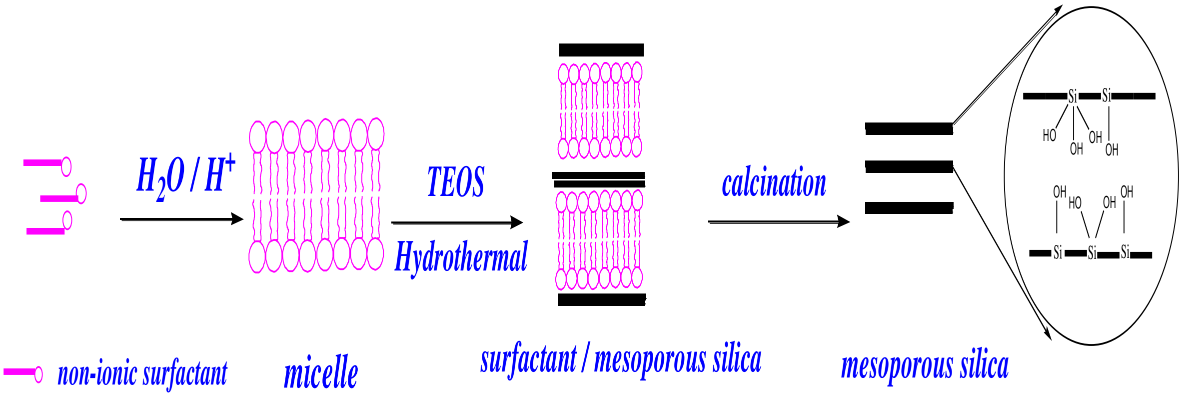

Scheme 3.2 Synthesis of SiO_2-L81, SiO_2-L61 and SiO_2-L31.

3.3 Fourier transform infrared (FTIR)

FTIR spectroscopy is a useful tool to understand the functional group of any material. Figure 3.1 (a & b) shows FTIR spectra of SiO_2-L81 and SiO_2-P123 (SBA-15), respectively. Three absorption regions at 3400-3600 cm^{-1}, 1500-1700 cm^{-1} and 400-1400 cm^{-1} are observed due to ν(O-H), δ(O-H) and (Si-O-Si) vibrations, respectively. A broad band in range of 3400 – 3600 cm^{-1} in Figure 3.1 (a & b) is due to ν(O-H) vibration. This is attributed to hydrogen-bonded silanol groups. The weak peak at 1645 cm^{-1} (Figs.3.1 (a & b)) is probably due to δ(O-H) vibrational. A strong broad band around 1000-1150 cm^{-1} centered at 1085 cm^{-1} (Figs.3.1 (a & b)) is due to the asymmetric stretching vibrational of ν(Si–O) of silica network. In Figures.3.1 (a&b), weak shoulder at 965 cm^{-1} is due to ν(Si-O) vibration of non-condensed silanol groups. The peak around 800 cm^{-1} (Figs.3.1 (a & b)) is due to symmetric stretching of (Si-O) vibration from silica network. The peak around 459 cm^{-1} (Figs.3.1 (a & b)) is due to δ(Si–O) bending vibration from silica network (Wanyika *et al.*, 2011; Wu *et al.*, 2013).

FTIR spectra of SiO_2-P123 (SBA-15) and SiO_2-L81 are similar, which give a good indication about the nature and the functional groups in SiO_2-L81. In contrast, Pluronic P123, long EO chain form 2D hexagonal porous structure was obtained.

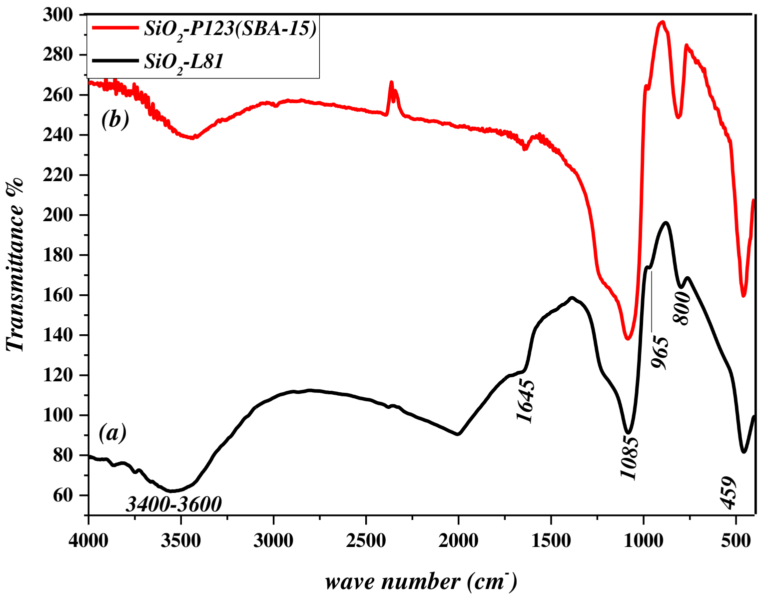

Figure 3.1 FTIR spectra of (a) SiO_2-L81 and (b) SiO_2-P123 (SBA-15).

3.4 X- ray diffraction (XRD)

XRD patterns of SiO_2-L81, SiO_2-L61 and SiO_2-L31 (Figs.3.2 (b-d)) are similar to the XRD pattern of SiO_2-P123 (SBA-15) (Fig.3.2a). This confirmed the amorphous nature of the new synthesized silica (SiO_2-L81, SiO_2-L61 and SiO_2-L31) is similar to that of SBA-15. Figure 3.2 (a-d) shows a strong diffraction peak at 23° which revealed regular periodic variations of the electronic density due to the long-range ordering of the pores in the material (Wanyika *et al.*, 2011).

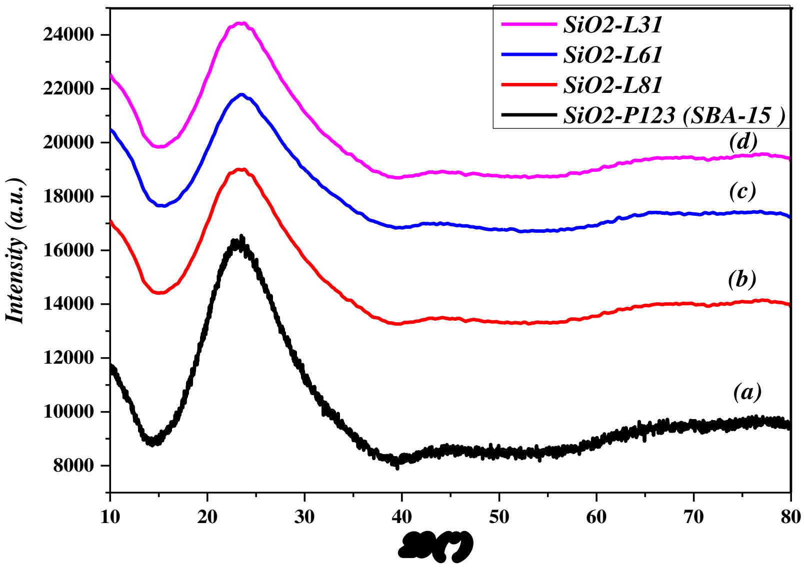

Figure 3.2 XRD patterns of (a) SiO_2-P123 (SBA-15), (b) SiO_2-L81, (c) SiO_2-L61 and (d) SiO_2-L31.

3.5 Small angle X- ray scattering (SAXS)

Small angle X-ray scattering (SAXS) technique is capable of delivering structural information of molecules between 5 and 25 nm. Figure 3.3 shows SAXS pattern of SiO_2-P123 (SBA-15) synthesized with Pluronic P123 (EO_{20} PO_{70} EO_{20}) surfactant. A typical pattern of a hexagonal structure with the occurrence of a strong peak, due to the (100) plane, and other two weak peaks is appeared, due to the (110) and (200) planes. The presence of three well-resolved diffraction peaks is associated with highly ordered mesoporous silica SiO_2-P123 (SBA-15) with a two-dimensional hexagonal structure (space group p6mm) (Thielemann *et al.*, 2011). The d_{100} spacing value is 8.8 nm for silica SiO_2-P123 (SBA-15) and pore-to-pore distance (a_0) is 10.2 nm. We expect that more hydrophilic state is present in the case where P123 is used and this of course lead to different mesoporous structure of these material where well-ordered mesoporous material with larger pores are formed.

In case of Pluronic L81, L61 and L31, the PO/EO is larger than that of P123. More hydrophobic properties is obtained, and a lamellar liquid crystal structure is formed. Figure 3.4 (a-c) shows SAXS patterns of SiO_2-L81, SiO_2-L61 and SiO_2-L31, respectively. These synthesized silica materials are made by triblock copolymer (L31 (EO_2 PO_{16} EO_2), L61 (EO_2 PO_{31} EO_2) and L81 (EO_3 PO_{43} EO_3)) with short EO chains. These materials have less order than that obtained when P123 surfactant is used, with typical lamellar structure with two broad peaks at q= 0.625 nm^{-1} and 3.25 nm^{-1} (Dovgolevsky *et al.*, 2008; García-Martínez *et al.*, 2007). The obvious feature for these Pluronic is the length of the EO block is the same, approximately 3 unit on each side of the PO block. The central PO block vary in length: L81, 43; L61, 31 and L31, 16 units. Hence, the length of PO block has more relation with pore size and silica order (Barrabino, 2011). As the length of the polymers increased, the ability to direct the silica towards an ordered structure was enhanced (Flodström & Alfredsson, 2003). In Figure 3.4, it can be seen that a Pluronic with a long PO-block, such as L81, results in a material with more distinct Bragg peaks than the Pluronics with shorter PO blocks, such as L61 and L31. SiO_2-L81 shows a typical pattern of lamellar structure with the occurrence of two broad peaks at q = 0.625 nm^{-1} and 3.25 nm^{-1}, due to (001) and (002) reflections of lamellar structure (Dovgolevsky *et al.*, 2008; García-Martínez *et al.*, 2007). While SiO_2-L61 and SiO_2-L31 show a typical pattern of lamellar structure with the occurrence of a broad peak at q = 3.25 nm^{-1}, due to (002) reflection of lamellar structure (Zhang & Tsapatsis, 2011).

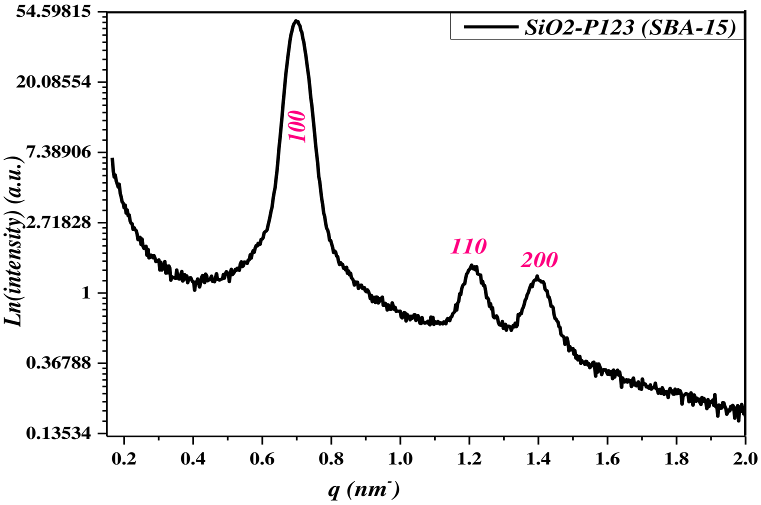

Figure 3.3 SAXS results for SiO_2-P123 (SBA-15).

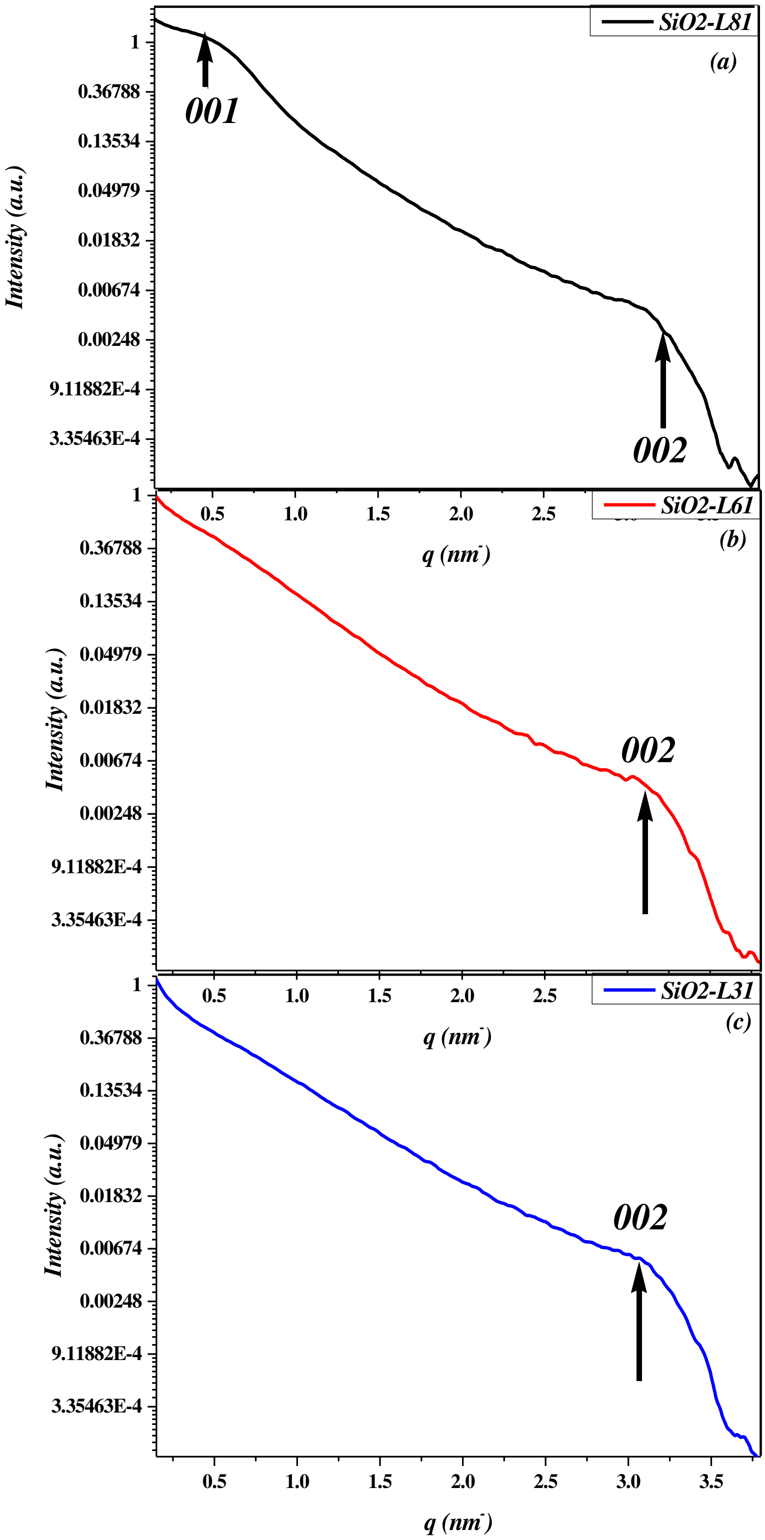

Figure 3.4 SAXS results for (a) SiO_2-L81, (b) SiO_2-L61 and (c) SiO_2-L31.

3.6 Transmission electron microscopy (TEM)

TEM analysis is used to study the morphology of the product. Figure 3.5 (a & b) shows TEM image of SiO_2-P123 (SBA-15) and SiO_2-L81, respectively. In Figure 3.5a, the hexagonal arrangement of the pores confirming the mesoporous ordered structure of SiO_2-P123 (SBA-15) material (Kipkemboi *et al.*, 2001). The estimated pore diameter is about 5.1 nm, center-to-center pore distance is about 10.2 nm which is exactly of same value obtained from SAXS analysis. High-resolution TEM image (Fig.3.5b) shows short channels which are parallel to each other confirming the lamellar mesostructure of SiO_2-L81, in a good agreement with SAXS results (Dovgolevsky *et al.,* 2008).

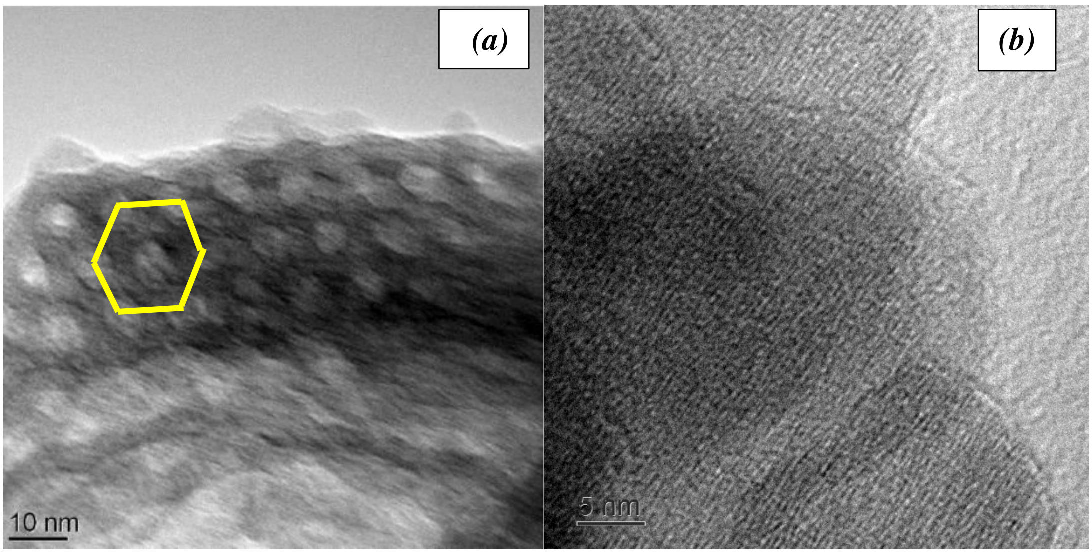

Figure 3.5 TEM image of (a) SiO_2-P123 (SBA-15) and (b) SiO_2-L81.

3.7 Thermal gravimetric analysis (TGA)

Thermal gravimetric analysis (TGA) used to determine chemical changes, which result as changes in mass when material is heated. Thermal gravimetric analysis (TGA) and differential thermal analysis (DTA) are examined under nitrogen at 25-600 °C at rate 10 °C/min. Figure 3.6 (a, b) shows TGA-DTA patterns of SiO_2-L81 and SiO_2-P123 (SBA-15), respectively. TGA-DTA showed two steps of weight loss. The first step occurs at 75 °C due to loss of 1.2-1.4 % of its initial weight. This is attributed to loss of physisorbed water from the system pores. The second step occurs at 300 °C due to loss of 1-1.3 %, which is probably due to the condensation reaction between the Si–OH groups. The total loss is 2.2-2.7 % (Zhang & Li, 2013).

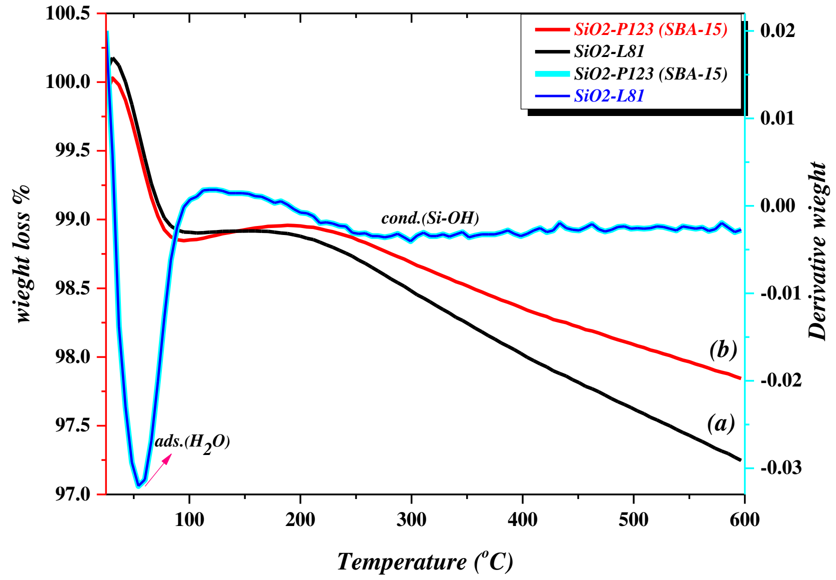

Figure 3.6 TGA-DTA pattern of (a) SiO_2-L81 and (b) SiO_2-P123 (SBA-15).

3.8 Conclusion

Four different types of mesoporous silica were successfully synthesized by sol-gel, using triblock copolymer Pluronic nonionic surfactants. The synthesized materials were characterized using several characterization techniques such as FTIR, XRD, SAXS TEM and TGA. FTIR spectra confirm that all synthesized mesoporous silica materials have the same function groups (i.e. they form silica network with free silanol groups on their surface). Surfactants were totally removed via calcination. From SAXS and TEM, the mesoporous silica structure of the synthesized materials were determined. The medium EO chain surfactant (as P123) gives 2D hexagonal (P6mm) structure, while the short EO chain surfactants (L81, L61 and L31) give a lamellar structure. In addition, as PO chain increased the ordering of mesoporous silica increased. SAXS analysis showed that SiO_2-L81 has more pronounced lamellar structure than SiO_2-L61 and SiO_2-L31 ones. TGA thermogram confirms a high thermal stability of the synthesized mesoporous silica material at high temperature.

Chapter Four

Results and Discussion

Synthesis and characterization of encapsulated metal oxides mesoporous silica.

4.1 Introduction

Modification of silica mesoporous materials becomes the key step to enable them applied in industry. Some of the methods used to synthesize encapsulated metal oxide mesoporous silica are direct synthesis and post modification. The co-condensation (direct synthesis) attracts most attention because it is time saving (Lee *et al.*, 2012;Wang *et al.*, 2005). The impregnation (post modification) requires multistep procedures (Furtado *et al*, 2011; Roggenbuck *et al.*, 2008). In our research, the impregnation method was used in the preparation. Four different metals acetate salts ($Ca(CH_3COO)_2$, $Mg(CH_3COO)_2$, $Cu(CH_3COO)_2$ and $Zn(CH_3COO)_2$) are used in the synthesis with four types of mesoporous silica (SiO_2-P123 (SBA-15), SiO_2-L81, SiO_2-L61 and SiO_2-L31). Metal precursors are introduced into the mesoporous silica to control the particle size and growth of nanoparticles. Calcination step was needed to convert metal acetate to its corresponding metal oxide. Sixteen different encapsulated metal oxide/mesoporous silica materials were prepared. Several methods and techniques were used for structural characterization of these new materials. These methods include fourier transform infrared spectroscopy (FTIR), X-ray diffraction (XRD), small angle X- ray scattering (SAXS), transmission electron microscopy (TEM) and thermal gravimetric analysis (TGA).

4.2 Synthesis

Encapsulated metal oxide/mesoporous silica materials were prepared as previously reported in literature (Furtado *et al*, 2011; Lee & Chang, 2012). Each metal acetate was allowed to disperse into the silica pores network under suitable conditions of stirring and temperature. The encapsulation process was completed to dryness. Calcination step at 600 ^{o}C for 4 h was required to convert metal acetate to its corresponded metal oxide (Scheme 4.1 & scheme 4.2). Table 4.2 summarizes the experimental data for the prepared materials.

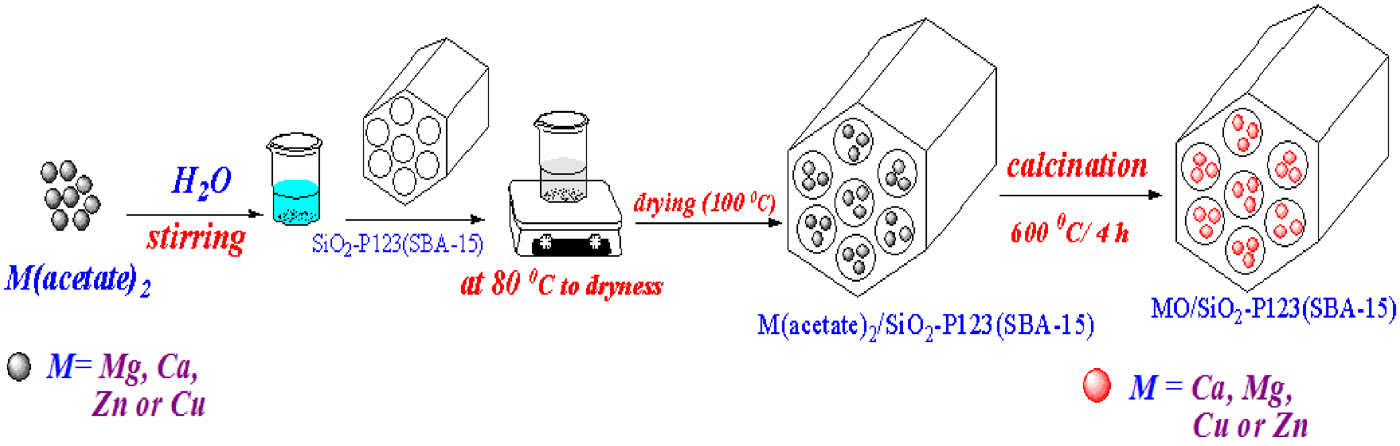

Scheme 4.1 Synthesis of encapsulated metal oxide/ SiO_2-P123 (SBA-15).

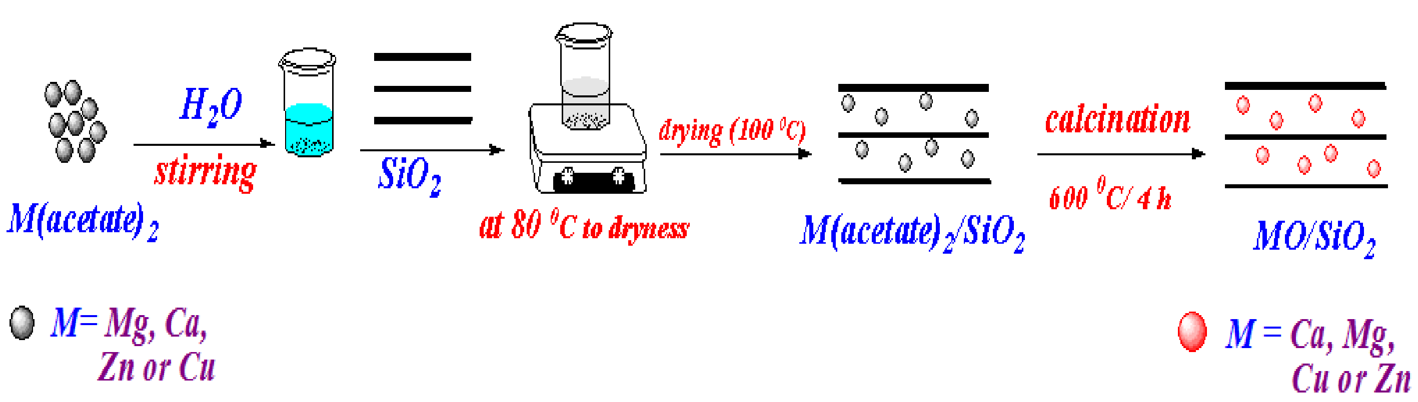

Scheme 4.2 Synthesis of encapsulated metal oxide/ lamellar mesoporous silica.

4.3 CaO/mesoporous silica

4.3.1 Fourier transform infrared (FTIR)

Figure 4.3.1 (a-c) shows FTIR spectra of CaO, SiO_2-L81 and CaO/SiO_2-L81, respectively. Three absorption regions are detected at 3100-3600 cm^{-1}, 1500-1800 cm^{-1} and 400-1200 cm^{-1} due to ν(O-H); ν(C-O) and δ(O-H); ν(Ca-O) and (Si-O-Si) vibrations, respectively. The FTIR spectrum of CaO (Fig.4.3.1a) is complicated which reflects that CaO is presented in a mixture of three components CaO, $Ca(OH)_2$ and $CaCO_3$. This was confirmed later from XRD analysis. The sharp peak at 3643 cm^{-1} (Fig.4.3.1a) is due to ν(O-H) of free hydroxyl group of $Ca(OH)_2$ component (Mirghiasi *et al.*, 2014). The broad band at 3400-3600 cm^{-1} (Figs.4.3.1 (b & c)) is due to ν(O-H) stretching vibration of hydrogen bonded hydroxyl group with water molecules inside silica pores (Wanyika *et al.*, 2011; Wu *et al.*, 2013). The peak at 1645 cm^{-1} (Figs.4.3.1 (b & c)) is due to δ(O-H) bending vibration (Yang *et al.*, 2008). At 965 cm^{-1} a slight weak shoulder (Figs.4.3.1 (b & c)) is due to ν(Si-O) vibration of non-condensed silanol groups. In Figure 4.3.1 (b & c), the three peaks at 1087 cm^{-1} (broad), 800 cm^{-1} and 459 cm^{-1} are due to asymmetric, symmetric stretching and bending of Si-O-Si vibrations from silica network, respectively (Wanyika *et al.*, 2011; Wu *et al.*, 2013). A broad peak at 500 cm^{-1} (Fig.4.3.1.a) is due to ν(Ca-O) of CaO nanoparticle (Mirghiasi *et al.*, 2014). This broad peak for pure CaO is decreased to a shoulder at about 510 cm^{-1} for encapsulated CaO/mesoporous silica (Figs.4.3.1 (b & c)). A weak peak at 1799 cm^{-1} (Fig.4.3.1.a) is also associated to the carbonate C═O bond (Miguel *et al.*, 2009). The broad band at 1400-1500 cm^{-1}, and two weak peaks at 883 cm^{-1} and 715 cm^{-1} (Fig.4.3.1.a) are due to the ν(C-O) related to carbonation of CaO (Miguel *et al.*, 2009; Mirghiasi *et al.*, 2014). The weak absorption peaks at 2972 cm^{-1}, 2864 cm^{-1} and 2516 cm^{-1} (Fig.4.3.1.a) are assigned to (C=O) vibration of carbonate in $CaCO_3$ component (Miguel *et al.*, 2009).The absence of the peaks at 2972 cm^{-1}, 2864 cm^{-1}, 2516 cm^{-1}, 1799 cm^{-1}, 1400-1500 cm^{-1} and 883 cm^{-1} is good evidence for CaO encapsulation onto SiO_2-L81 (Figs.4.3.1 (b & c). This probably that silica encapsulation of CaO may to some extent protect the CaO from interaction with environment. CaO absorbed onto the silica surface may still interact with outside environment and form $Ca(OH)_2$ and $CaCO_3$.

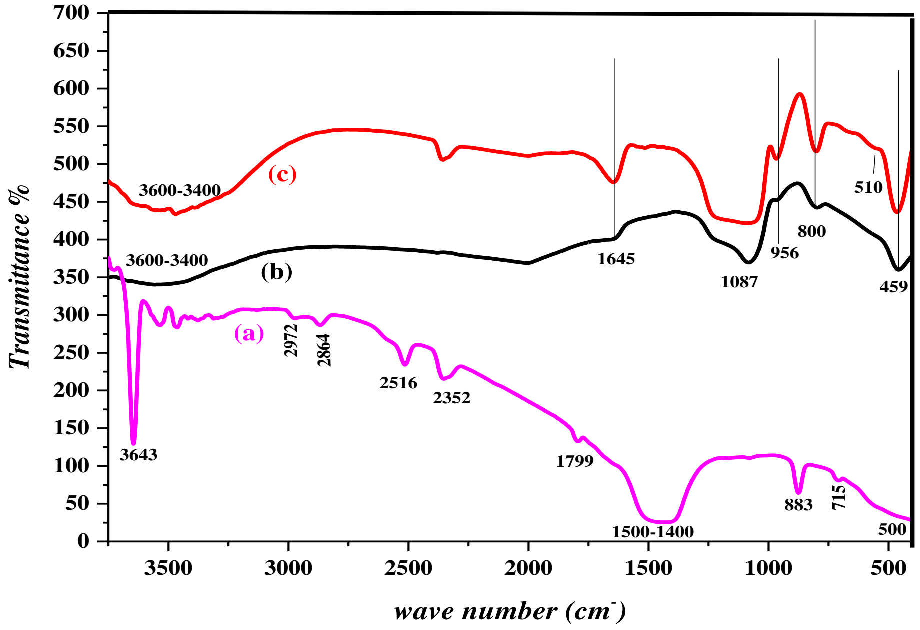

Figure 4.3.1 FTIR spectra of (a) CaO, (b) SiO_2-L81 and (c) CaO/SiO_2-L81.

4.3.2 X- ray diffraction (XRD)

Figure 4.3.2 (a-c) and Figure 4.3.3 show XRD patterns of CaO/SiO_2-L81, CaO/SiO_2-L61, CaO/SiO_2-L31 and pure CaO, respectively. Figures.4.3.2 (a-c) patterns exhibit strong peaks corresponding to a face centered cubic crystal structure of CaO (*) (Imtiaz *et al.*, 2013), hexagonal crystals structure of $Ca(OH)_2$ ($) and $CaCO_3$ (♦) (Stutzman, 1996). In Figures 4.3.2 (a-c), XRD patterns show a reflection peaks at $2\theta = 32.7°, 54.2°, 64.2°$ and $68.7°$ corresponding to (111), (202), (311) and (222) planes of CaO with a face-centered cubic structure, respectively (Imtiaz *et al.*, 2013). All the diffraction peaks of CaO are matched with a face centered cubic structure of CaO (JCPDS PDF# 82-1690) (Imtiaz *et al.*, 2013). Some calcite peaks ($CaCO_3$) with low intensity are presented in the XRD pattern of CaO, illustrated rapid carbonation of CaO by atmospheric CO_2 (Mirghiasi *et al.*, 2014). Carbonation reaction occurs very fast for CaO-NPs. All CaO diffraction peaks were observed for all types of materials with a little difference in intensity. The FTIR spectra and XRD results have confirmed that neither free CaO and its encapsulated silica materials contain pure calcium oxide and a mixture of CaO, $Ca(OH)_2$ and $CaCO_3$ components may present. Scherer's equation determines the crystallite mean size. Scherer's equation, $d = \frac{0.9*\lambda}{\beta*cos\theta}$, (where d is the mean crystallite size, λ is the wavelength of X-ray radiation (0.154 nm), β is the full width at half maximum at Bragg's angle of interest and θ is Bragg's angle of interest), is used to calculate the mean crystallite size of CaO encapsulated by SiO_2-L81, SiO_2-L61 and SiO_2-L31 was estimated. The average crystallite particle size of CaO are given in Table 4.1.

It is found that the peaks intensity of all peaks are decreases in the following order :

CaO/SiO_2-L31 > CaO/SiO_2-L61 > CaO/SiO_2-L81.

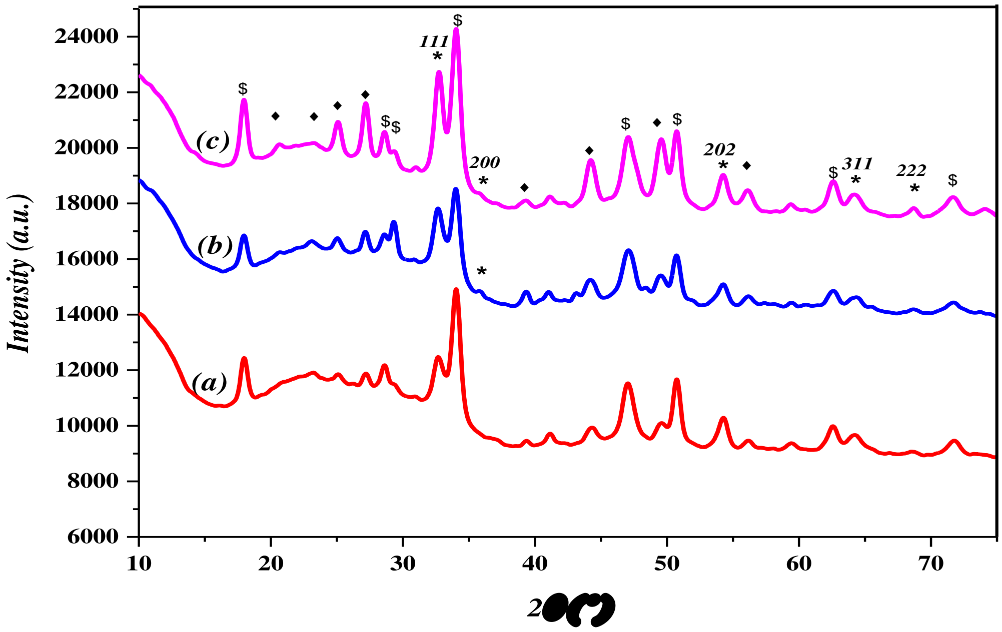

Figure 4.3.2 XRD pattern of (a) CaO/SiO$_2$-L81, (b) CaO/SiO$_2$-L61 and (c) CaO/SiO$_2$-L31.

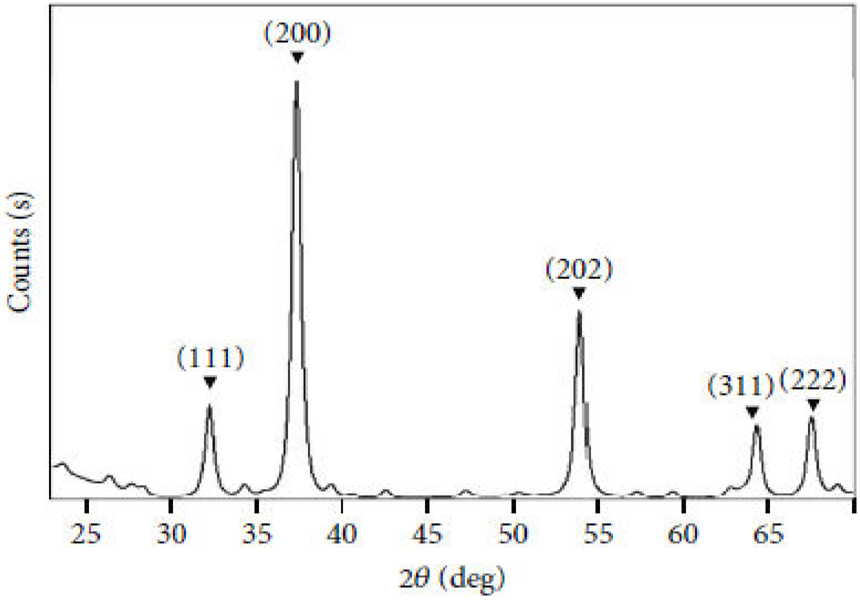

Figure 4.3.3 XRD pattern of pure CaO (Imtiaz *et al.*, 2013).

Table 4.1 Results of mean crystallize particle size of encapsulated metal oxides

Metal oxide/mesoporous silica	Mean crystallize particle size (nm)
CaO/SiO$_2$-L81	8.29
CaO/SiO$_2$-L61	8.25
CaO/SiO$_2$-L31	7.548

MgO/SiO_2-L61	9.3
MgO/SiO_2-L31	8.846
CuO/SiO_2-P123 (SBA-15)	21.4
CuO/SiO_2-L81	26.7
CuO/SiO_2-L61	25.5
CuO/SiO_2-L31	25.6
ZnO/SiO_2-P123 (SBA-15)	22.4
ZnO/SiO_2-L81	22.05
ZnO/SiO_2-L61	21.69
ZnO/SiO_2-L31	22.42

4.3.3 Small angle X- ray scattering (SAXS)

Figure 4.3.4 (a &b) shows SAXS pattern of SiO_2-L81 and CaO/SiO_2-L81, respectively. SiO_2-L81 (Fig.4.3.4a) material exhibits reflection peaks at 0.625 nm^{-1} and 3.25 nm^{-1} correspond to (001) and (002) of lamellar structure. However, the intensity of all reflections decrease (Fig.4.3.4b), which indicates that pore blocking by CaO-NPs have partly destroyed the lamellar structure of SiO_2-L81 (Haung *et al.* 2010). The decreasing of reflections intensity was probably caused by the decreasing scatter contrast between pore walls and pore space with the introduction of CaO-NPs (Sun *et al.*, 2010).

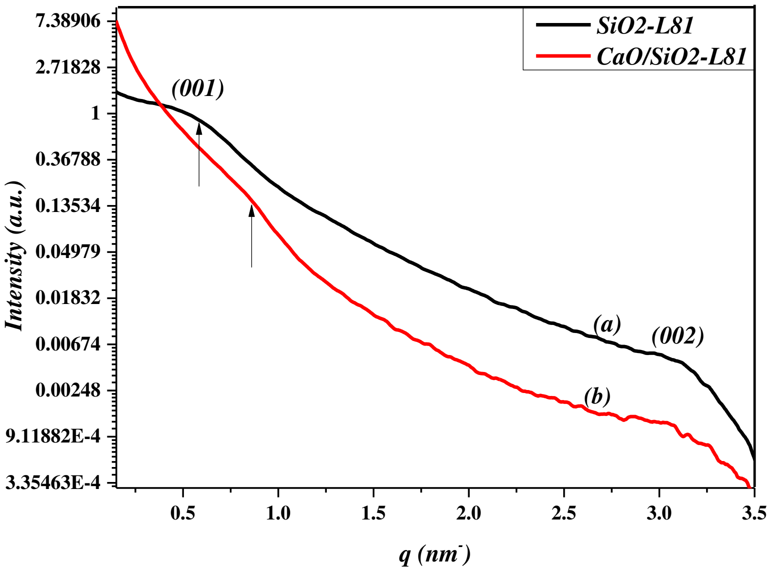

Figure 4.3.4 SAXS pattern of (a) SiO_2-L81, (b) CaO/SiO_2-L81.

4.3.4 Transmission electron microscopy (TEM)

TEM analysis is used to study the morphology of the product. Figure 4.3.5 (a-d) shows TEM images of CaO/SiO_2-L81, CaO/SiO_2-L61 and CaO/SiO_2-L31, respectively. CaO/SiO_2-L81 TEM image (Fig.4.3.5a) shows the encapsulation of CaO appearing in dark and mesoporous silica appearing in gray. In Figure 4.3.5a, CaO/SiO2-L81 TEM image shows some channel shape of mesoporous silica in gray color, while dark color CaO nanoparticles are impregnated into its mesoporous silica. Figure 4.3.5b shows CaO/SiO_2-L61 TEM image, where some channel shape of mesoporous silica in gray color, while dark color CaO nanoparticles are impregnated into its mesoporous silica. Figures 4.3.5 (c & d) show CaO/SiO_2-L31 TEM images, a well channels of mesoporous silica appeared in gray color, while a dark color indicates CaO nanoparticles impregnated into mesopores of SiO_2-L31.

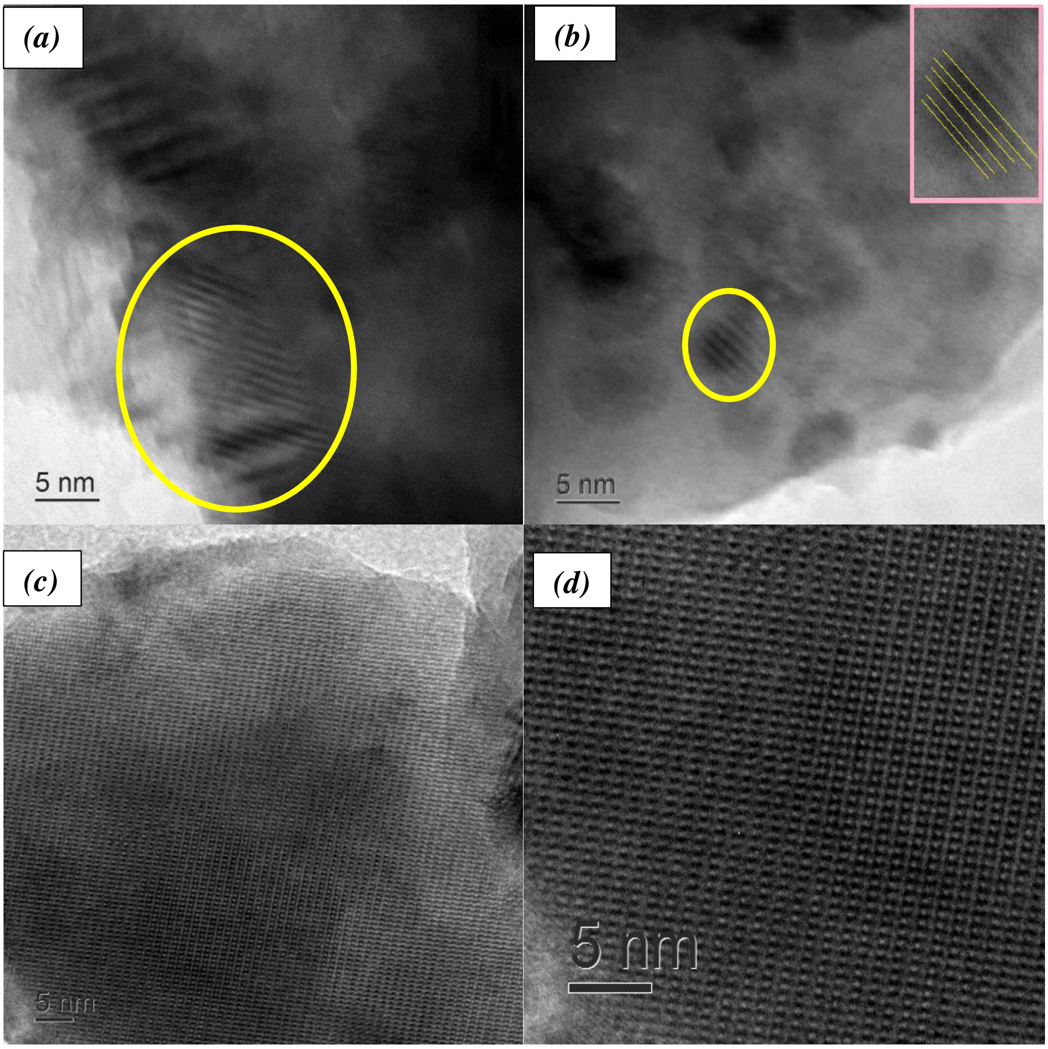

Figure 4.3.5 TEM image of (a) CaO/SiO_2-L81, (b) CaO/SiO_2-L61, (c) CaO/SiO_2-L31(low magnified) and (d) CaO/SiO_2-L31 (high magnified).

4.3.5 Thermal gravimetric analysis (TGA)

Thermal gravimetric analysis (TGA) is used to determine chemical changes, which result as changes in mass when the material is heated. Thermal gravimetric analysis (TGA) and differential thermal analysis (DTA) were examined for CaO, SiO_2-L81, SiO_2-P123 (SBA-15), CaO/SiO_2-L81 and CaO/SiO_2-P123 (SBA-15) under nitrogen at 25-600 ^oC at rate of 10 ^oC/minute. TGA pattern of CaO (Fig.4.3.6a and Fig.4.3.7a) shows a significant weight loss occurs at 440 ^oC due to loss of 7.2 %, which is due to loss of CO_2 as a result from a decomposition of the $CaCO_3$ to produce CaO nanoparticles (Butt *et al.*, 2015). The total loss is about 7.2 % of initial weight. This is provide evidence that CaO nanoparticles are unstable at the surface and they can easily absorbed CO_2 to form $CaCO_3$ as confirmed by XRD and FTIR spectra. From TGA pattern it is possible to calculate the amount of $CaCO_3$ in the sample, which is about 16 %. The rest is probably contain cubic CaO (84 %). No evidence for the presence of $Ca(OH)_2$ from the TGA-DTA patterns of CaO material.

Figure 4.3.6b and Figure 4.3.7b show TGA patterns of SiO_2-L81 and SiO_2-P123 (SBA-15), respectively. TGA patterns show two steps of weight loss. The first step occurs at 75 ^oC due to loss of 1.2-1.4 % of its initial weight. This is attributed to loss of physisorbed water from the system pores. The second step occurs at 300 ^oC due to loss of 1-1.3 %, which is probably due to the condensation reaction between the Si–OH groups (Zhang & Li, 2013). The total loss is 2.2-2.7 %.

TGA pattern of CaO/SiO_2-L81 (Fig.4.3.6c) shows three loss weight steps. The first step occurs at 75 ^oC due to 3 % that is correspond to loss of adsorbed water molecules in the silica pores and CaO surface. The second step occurs at 150 ^oC is due to 4% corresponds to condensation between $Ca(OH)_2$ and silanol groups. The third step occurs at 430 ^oC due to 4 %, correspond to decomposition of $CaCO_3$ (Ngamcharussrivichai *et al.*, 2011; Mirghiasi *et al.*, 2014; Sun *et al.*, 2010). The total loss is about 11 % of initial weight. From the TGA analysis, the amount of $CaCO_3$ present in the sample is about 9 %, $Ca(OH)_2$ is about 7% and CaO is about 84%.

TGA pattern of CaO/SiO_2-P123 (SBA-15) (Fig.4.3.7c) shows two loss weight steps. The first step occurs at 75 ^oC due to 2.3 % that is correspond to loss of adsorbed water in the silica pores and CaO surface. The second step occurs at 430 ^oC due to 1.2 %. This is attributed to decomposition of $CaCO_3$ (Butt *et al.*, 2015; Sun *et al.*, 2010). The total weight loss was 3.5 %.

In CaO (Fig.4.3.6a and Fig.4.3.7a), CaO/SiO_2-P123 (SBA-15) (Fig.4.3.7c) and CaO/SiO_2-L81(Fig.4.3.6c) thermograms show 7.2 %, 1.2 % and 4 % weight loss at 430 °C, respectively. This loss is attributed to decomposition of $CaCO_3$ to CaO and loss of CO_2. It was decreased from 7.2 to 4 % due to encapsulated of CaO within SiO_2-L81 and from 7.2 to 1.2 % due to encapsulated of CaO within SiO_2-P123 (SBA-15), which decrease the available area of CaO and decrease the adsorption amount of CO_2. The weight loss is 1.2 % for CaO/SiO_2-P123 (SBA-15), but the weight loss is 4 % for CaO/SiO_2-L81. This different is probably related to the percent of encapsulated CaO inside the pores and that on the surface of silica.

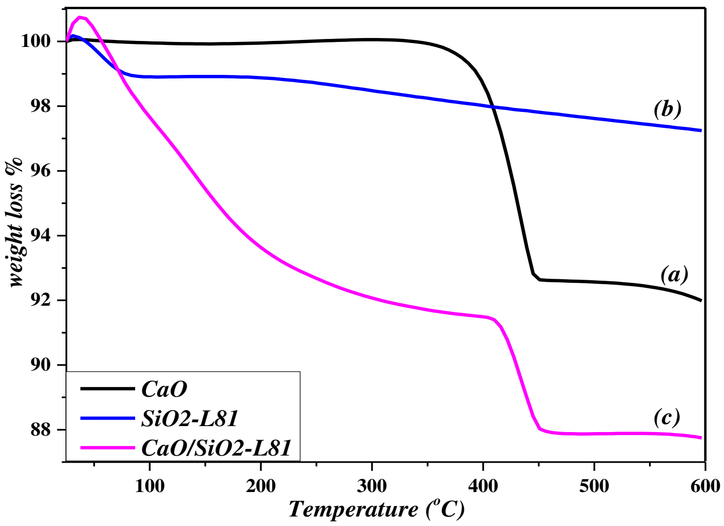

Figure 4.3.6 TGA pattern of (a) CaO, (b) SiO_2-L81 and (c) CaO/SiO_2-L81.

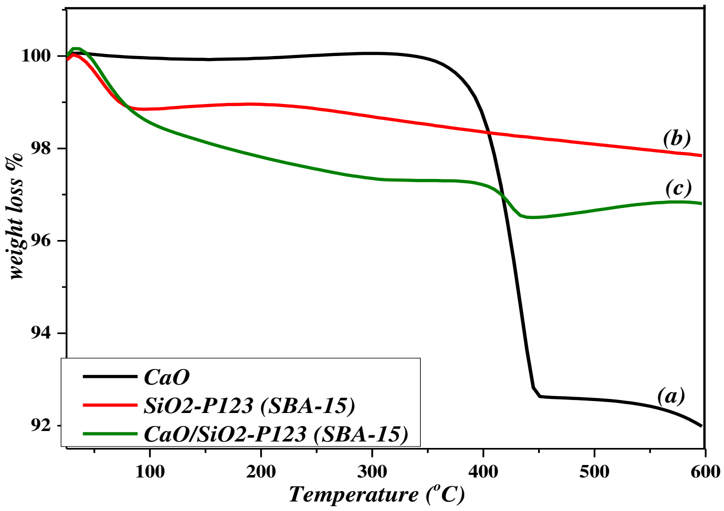

Figure 4.3.7 TGA pattern of (a) CaO, (b) SiO_2-P123 (SBA-15) and (c) CaO/SiO_2-P123 (SBA-15).

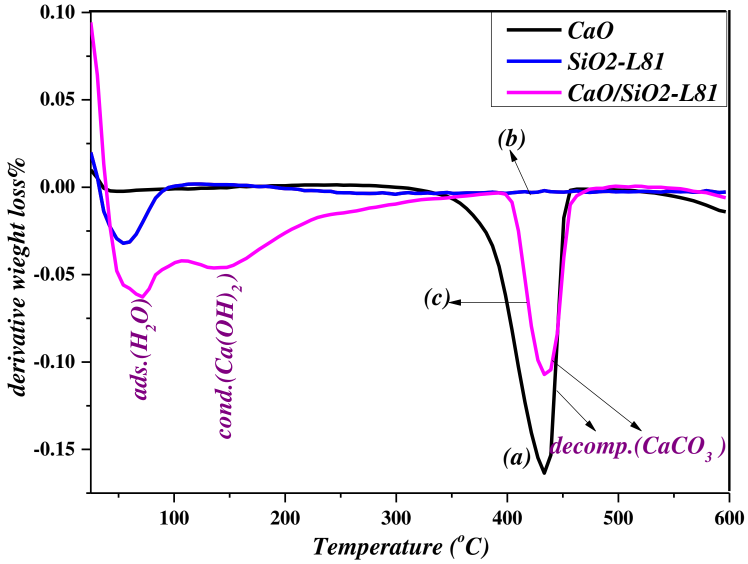

Figure 4.3.8 DTA pattern of (a) CaO, (b) SiO_2-L81 and (c) CaO/ SiO_2-L81.

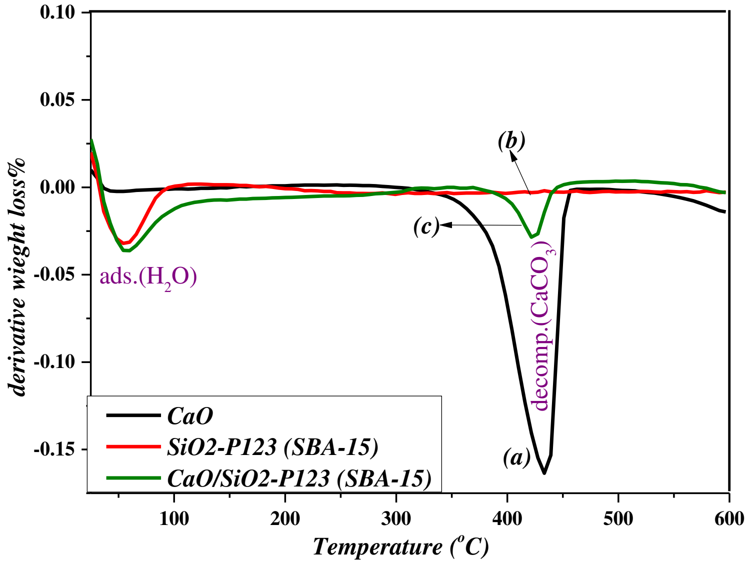

Figure 4.3.9 DTA pattern of (a) CaO, (b) SiO_2-P123 (SBA-15) and (c) CaO/SiO_2-P123 (SBA-15).

4.4 MgO/mesoporous silica.

4.4.1 Fourier transform infrared (FTIR)

Figure 4.4.1 (a-d) show FTIR spectra of MgO, SiO_2-L81, MgO/SiO_2-L81 and MgO/SiO_2-P123 (SBA-15), respectively. Three absorption regions at 3400-3600 cm^{-1}, 1400-1700 cm^{-1} and 400-1300 cm^{-1} are observed due to ν(O-H); ν(C-O) and δ(O-H); ν(Mg-O), and (Si-O-Si) vibrations, respectively. The sharp peak at 3640 cm^{-1} (Fig.4.4.1a) is due to ν(O-H) stretching vibration of free hydroxyl group on MgO crystal surface. The broad peak at 3400-3600 cm^{-1} (Figs. 4.4.1(a-d)) is due to ν(O-H) stretching vibration of hydrogen bonding hydroxyl group on MgO surface and inside silica pores (Mageshwari *et al.*, 2013; Wu *et al.*, 2013; Yang *et al.*, 2008). The two peaks at 1453 cm^{-1} and 1633 cm^{-1} (Fig.4.4.1a) are related to ν(C-O) of carbonate and δ(O-H) of adsorbed water on the surface of MgO crystals, respectively (Mageshwari *et al.*, 2013). Absorption peak at 1645 cm^{-1} (Figs.4.4.1 (b-d)) is due to δ(O-H) bending vibration (Wu *et al.*, 2013; Yang *et al.*, 2008). The absence of the peaks at 1633 cm^{-1} and 1453 cm^{-1} after encapsulation (Figs.4.4.1 (c & d)) is a good evidence for the encapsulation of MgO. The peaks at 1087 cm^{-1} (broad), 800 cm^{-1} and 459 cm^{-1} (Figs.4.4.1 (b-d)) are related to asymmetric, symmetric stretching and bending (Si-O-Si) vibration of silica network, respectively (Wu *et al.*, 2013; Yang *et al.*, 2008). The broad peak at 500 cm^{-1} (Fig.4.4.1a) is due to ν(Mg-O) stretching vibration (Mageshwari *et al.*, 2013). The decreasing of this broad band for pure MgO (Fig.4.4.1a) to a shoulder at 530 cm^{-1} (Figs.4.4.1 (c & d)) for encapsulated MgO is a good evidence for the success of encapsulation process (Salem *et al.*, 2015; Yang *et al.*, 2008).

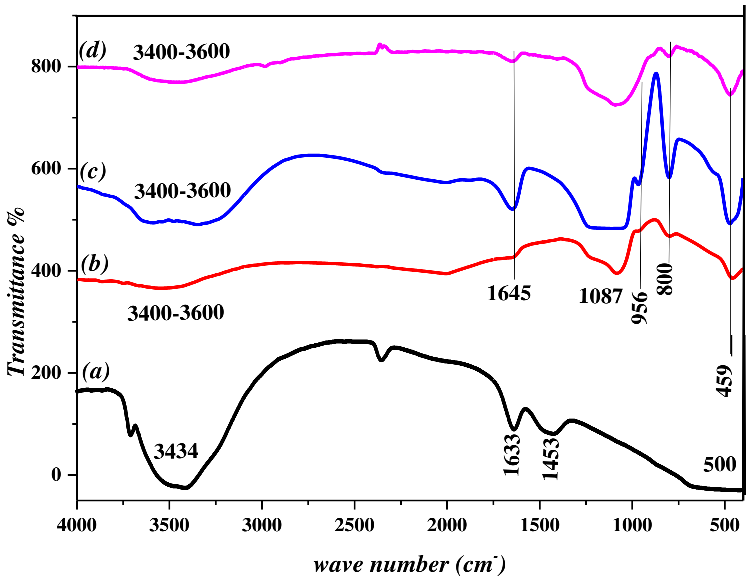

Figure 4.4.1 FTIR spectra of (a) MgO, (b) SiO_2-L81, (c) MgO/SiO_2-L81 and (d) MgO/SiO_2-P123 (SBA-15).

4.4.2 X- ray diffraction (XRD)

XRD gives information about crystalline structure of nanomaterials. Figure 4.4.2 (a-c) shows the XRD patterns of MgO/SiO_2-L81, MgO/SiO_2-L61 and MgO/SiO_2-L31, respectively. All diffraction peaks are matched with a face-centered cubic structure of MgO (JCPDS card no. 87-0653) (Hadia & Mohamed, 2015; Salem *et al.*, 2015). In Figure 4.4.2 (b & c), XRD patterns show major reflections at 2θ = 36.74°, 42.8°, 62.3°, 74.6° and 78.6° corresponding to (111), (200), (220), (311) and (222) planes of MgO with a face-centered cubic structure, respectively (Salem *et al.*, 2015). Diffraction peaks related to $Mg(OH)_2$ and impurities were not found in the XRD patterns, which confirm high purity of the synthesized materials. No diffraction peaks were detected for MgO/SiO_2-L81 (Fig.4.4.2a) in comparison with that of MgO/SiO_2-L61 and MgO/SiO_2-L31. The absence of the peaks for XRD pattern of MgO/SiO_2-L81 suggests that the MgO-NPs may present in non-crystalline form or that MgO-NPs present in small clusters in the pores of silica networks (Wang *et al.*, 2013). Scherer's equation was used for calculate the mean crystallite size of MgO encapsulated onto SiO_2-L61 and SiO_2-L31 were estimated and given in Table 4.1.

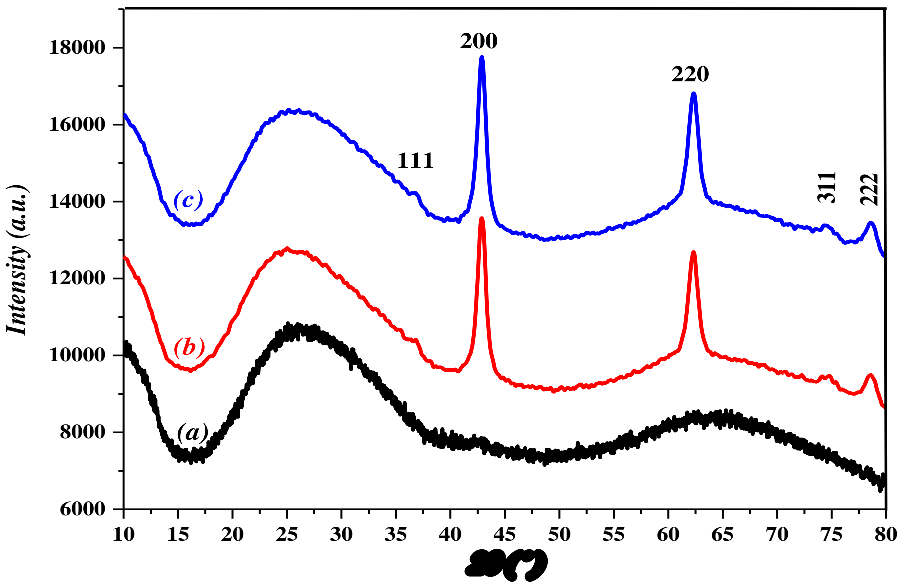

Figure 4.4.2 XRD pattern of (a) MgO/SiO$_2$-L81, (b) MgO/SiO$_2$-L61 and (c) MgO/SiO$_2$-L31.

4.4.3 Small angle X- ray scattering (SAXS)

SAXS pattern of SiO$_2$-L81 and MgO/SiO$_2$-L81 is depicted in Figure 4.4.3. The absence of the reflection peak due to (001) plane in the pattern of MgO/SiO$_2$-L81 (Fig.4.3.3b) upon impregnated MgO-NPs into SiO$_2$-L81 leads to distortion of the lamellar structure of SiO$_2$-L81 (Fig.4.3.3a). The decrease of the peak intensity at 3.25 nm^{-1} is expected due to the encapsulation of cluster material MgO into the pores, which leads to reduced scattering intensities for the Bragg reflections (Wang *et al.*, 2013).

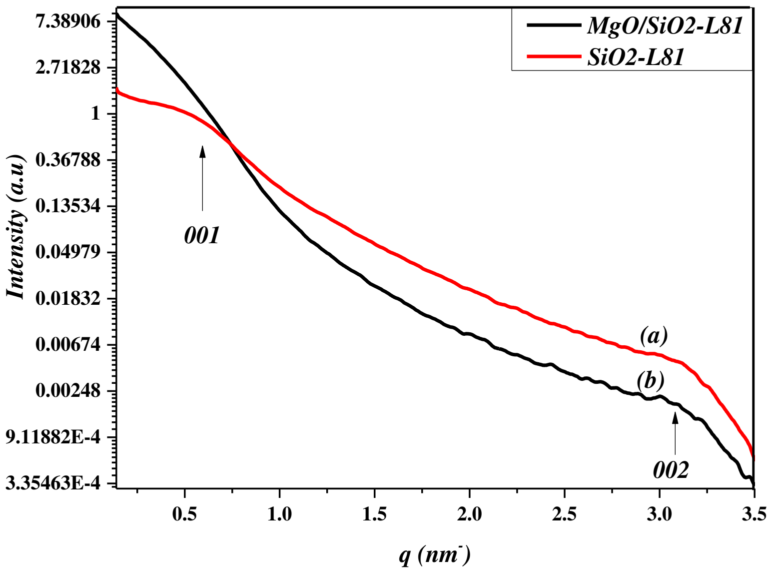

Figure 4.4.3 SAXS pattern of (a) SiO_2-L81 and (b) MgO/SiO_2-L81.

4.4.4 Transmission electron microscopy (TEM)

TEM analysis is used to study the morphology of the product. Figure 4.4.4(a & b) shows TEM image of SiO_2-L81 and MgO/SiO_2-L81, respectively. MgO nanoparticles are seen in dark and the mesoporous silica are seen in grey color.

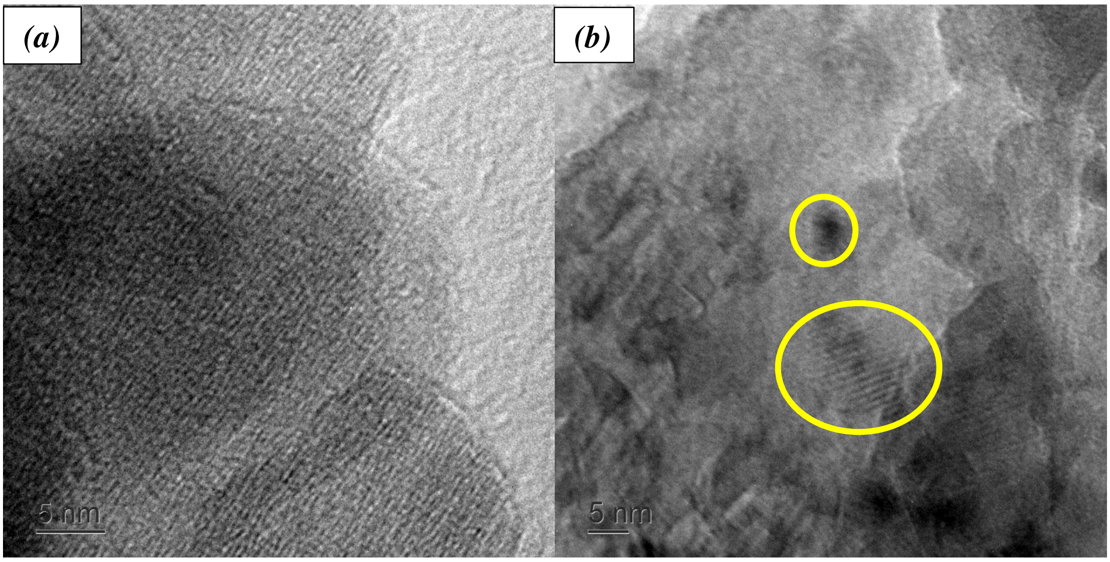

Figure 4.4.4 TEM image of (a) SiO_2-L81 and (b) MgO/SiO_2-L81.

4.4.5 Thermal gravimetric analysis (TGA)

Thermal gravimetric analysis (TGA) used to determine chemical changes, which result as changes in mass when material is heated. Thermal gravimetric analysis (TGA) and differential thermal analysis (DTA) are examined for SiO_2-L81, SiO_2-P123 (SBA-15), MgO, MgO/SiO_2-L81 and MgO/SiO_2-P123 (SBA-15) (Fig.4.4.5 and

Fig.4.4.6) under nitrogen at 25-600 ^oC at rate 10 ^oC/min, respectively. Figure 4.4.5a and figure 4.4.6a show TGA patterns of SiO_2-L81 and SiO_2-P123 (SBA-15), respectively. TGA patterns show two steps of weight loss. The first step occurs at 75 ^oC due to loss of 1.2-1.4 % of its initial weight. This is attributed to loss of physisorbed water from the system pores. The second step occurs at 300 ^oC due to loss of 1-1.3 %, which is probably due to the condensation reaction between the Si–OH groups (Zhang & Li, 2013). The total loss is 2.2-2.7 %.

TGA pattern of MgO (Fig.4.4.5b & Fig.4.4.6b) show two steps of weight loss. These steps at 75 ^oC and 280 ^oC are due to weight loss of ~ 1 % and 2 % of its initial weight correspond to loss of adsorbed H_2O and loss of adsorbed CO_2 on MgO crystal surface, respectively [12]. The total weight loss is 3 %.

TGA-DTA patterns of MgO/SiO_2-L81 (Fig.4.4.5c & Fig.4.4.6c) show three steps of weight loss. These steps at 95 ^oC, 176 ^oC and 340 ^oC are due to weight loss of ~ 1.5 %, 4.5 % and 5 % of its initial weight, respectively. These are correspond to loss of adsorbed H_2O on the surface of metal and silica pores, loss of crystallize water on MgO surface and loss of adsorbed CO_2 on MgO surface (Azzaza *et al.*, 2014; Maoz *et al.*, 2011; Zhang & Li, 2013). The total weight loss is 11 %.

TGA-DTA patterns of MgO/ SiO_2-P123 (SBA-15) (Fig.4.4.5d & Fig.4.4.6d) show two steps of weight loss. The first step at 80 ^oC due to ~ 6.5 % weight loss is correspond to loss of adsorbed H_2O on the surface of metal and silica pores. The second step is very weak at 250 ^oC due to 2.5 % weight is probably due to some dehydroxylation of silanol and formation of siloxane bonds (Azzaza *et al.*, 2014; Maoz *et al.*, 2011; Zhang & Li, 2013). The total loss is about 9 % of initial weight.

The difference in the weight loss in the first step between the silica and the encapsulated MgO is refers to the presence of crystallize water molecules of the metal oxide. It seems that more MgO nanoparticles absorbed onto SiO_2-L81 than SiO_2-P123 (SBA-15) silica.

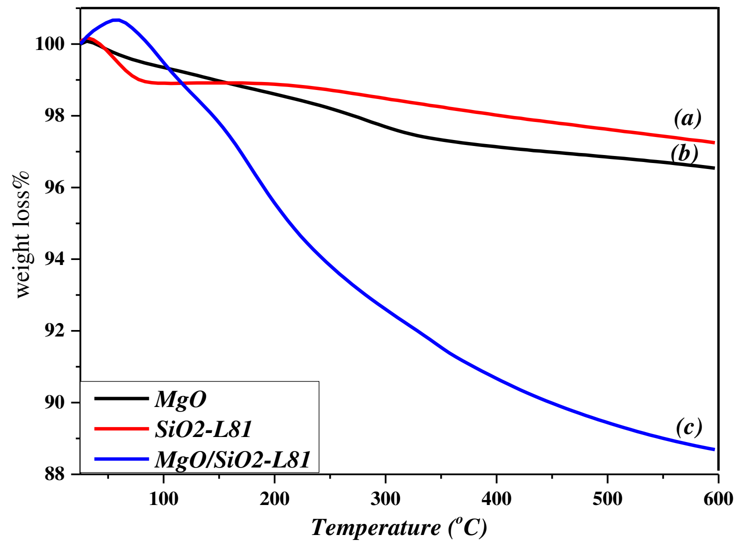

Figure 4.4.5 TGA pattern of (a) SiO_2-L81, (b) MgO and (c) MgO/SiO_2-L81.

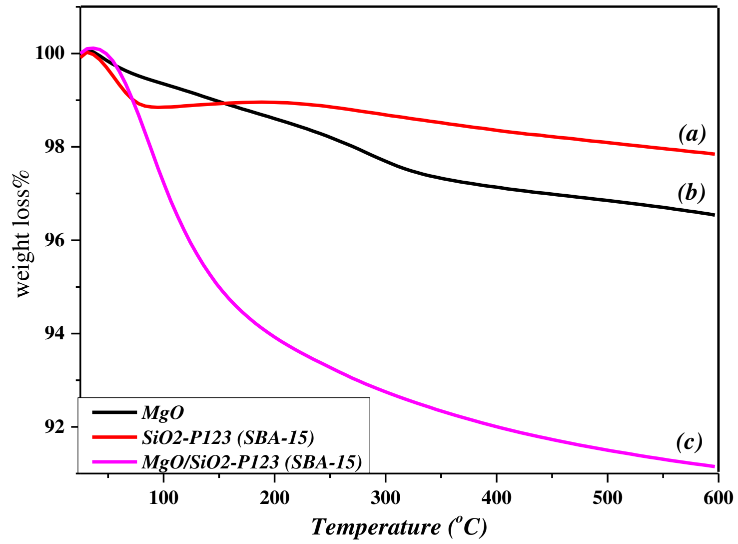

Figure 4.4.6 TGA pattern of (a) SiO_2-P123 (SBA-15), (b) MgO and (c) MgO/SiO_2-P123 (SBA-15).

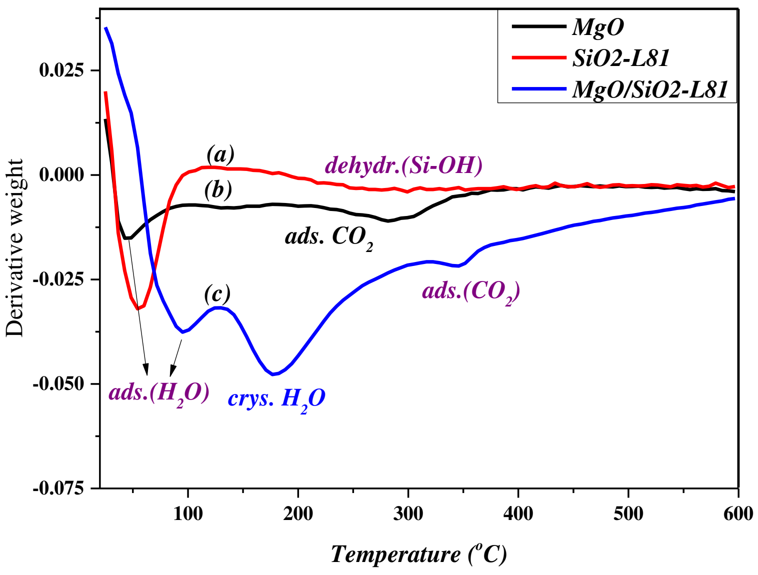

Figure 4.4.7 DTA pattern of (a) SiO_2-L81, (b) MgO and (c) MgO/SiO_2-L81.

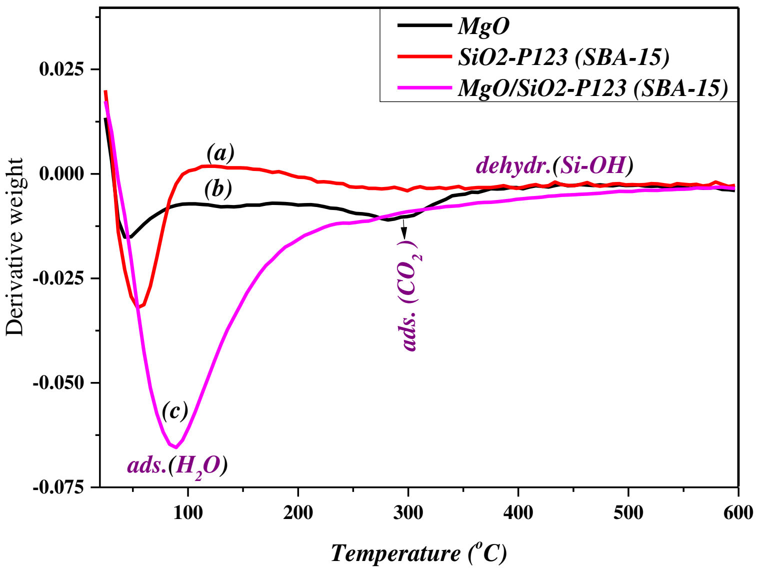

Figure 4.4.8 DTA pattern of (a) SiO_2-P123 (SBA-15), (b) MgO and (c) MgO/SiO_2-P123 (SBA-15).

4.5 ZnO/mesoporous silica.

4.5.1 Fourier transform infrared (FTIR)

Figure 4.5.1 (a-d) shows FTIR spectra of ZnO, SiO_2-L81, ZnO/SiO_2-L81 and ZnO/SiO_2-P123 (SBA-15), respectively. Three absorption regions at 3400-3600 cm^{-1}, 1400-1700 cm^{-1} and 400-1300 cm^{-1} are observed due to ν(O-H); δ(O-H); ν(Zn-O) and (Si-O-Si) vibrations, respectively. A broad band centered at 3500 cm^{-1} according to (O–H) stretching vibration correspond hydrogen bonding between adsorbed water and ZnO and silica surfaces (Figs.4.5.1 (a-d)) (Ambika & Sundrarajan, 2015; Yang *et al.*, 2008). The peak at 1631 cm^{-1} (Fig.4.5.1a) and 1645 cm^{-1} (Figs.4.5.1 (b-d)) are attributed to (O–H) bending vibration of hydroxyl groups (Ambika & Sundrarajan, 2015; Wu *et al.*, 2013; Yang *et al.*, 2008). The peaks at 1087 cm^{-1} (broad), 800 cm^{-1} and 459 cm^{-1} (Figs. 4.5.1 (b-d)) are due to asymmetric, symmetric stretching and bending of Si–O–Si vibrations from silica network (Wu *et al.*, 2013; Yang *et al.*, 2008). The shoulder at 965 cm^{-1} (Figs.4.5.1 (b-d)) is due to ν(Si–O) vibration of non-condensed silanol group (Yang *et al.*, 2008). An absorption peak at 1000 cm^{-1} (Fig.4.5.1a) according to stretching vibration of Zn–O-Zn bridging (Ambika & Sundrarajan, 2015). The peak at 511 cm^{-1} (Fig.4.5.1a) is due to Zn-O stretching vibration of ZnO (Ambika & Sundrarajan, 2015). The absence of the peaks at 511 cm^{-1}, 1000 cm^{-1} (Fig.4.5.1a) and the shoulder at 965 cm^{-1} (Fig.5.4.1b) after encapsulation (Figs.4.5.1 (c & d)) is a good evidence for the formation of Si-O-Zn linkage.

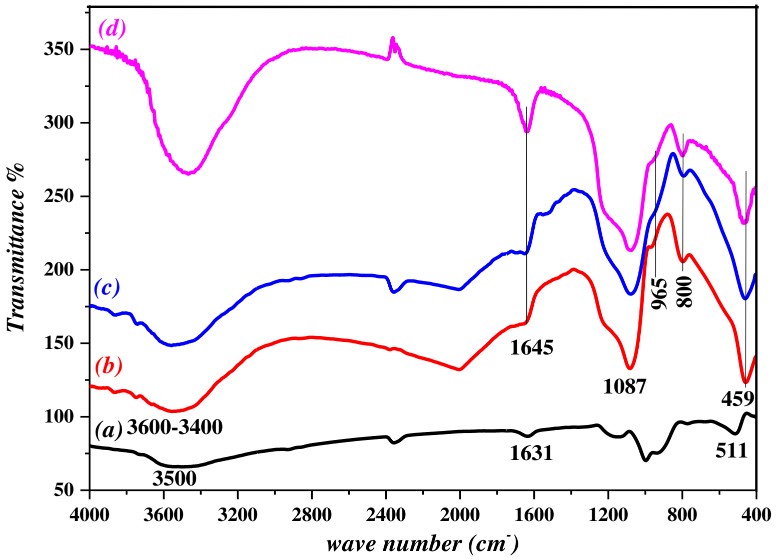

Figure 4.5.1 FTIR spectra of (a) ZnO, (b) SiO_2-L81, (c) ZnO/SiO_2-L81 and (d) ZnO/SiO_2-P123 (SBA-15).

4.5.2 X- ray diffraction (XRD)

Figure 4.5.2 (a-d) shows XRD patterns of ZnO/SiO_2-P123 (SBA-15), ZnO/SiO_2-L81, ZnO/SiO_2-L61 and ZnO/SiO_2-L31, respectively. All diffraction peaks of XRD were matched with hexagonal phase (wurtzite structure) of ZnO (JCPDS card No. 89-7102) (Kundu *et al.*, 2014). In Figure 4.5.2 (a-d), the peaks at 31.7°, 34.35°, 36.17°, 47.46 °, 56.57°, 62.82°, 66.36 °, 67.9° and 69.04° were assigned to the (100), (002), (101), (102), (110), (103), (200), (201) and (112) reflections, respectively (İpeksaç *et al.*, 2013; Kundu *et al.*, 2014; Talebian *et al.*, 2013). Diffraction peaks related to impurities were not found in XRD patterns that confirm high purity of the synthesized materials. ZnO diffraction peaks in SiO_2-L81, SiO_2-L61 and SiO_2-L31 were more intense than in SiO_2-P123 (SBA-15). The reason for this behavior is that in the case of SiO_2-P123 (SBA-15), ZnO nanoparticles are inserted into mesopores of the silica precursors. Scherer's equation was used for calculate the mean crystallite size of ZnO encapsulated onto SiO_2-P123 (SBA-15), SiO_2-L81, SiO_2-L61 and SiO_2-L31 were estimated and listed in Table 4.1.

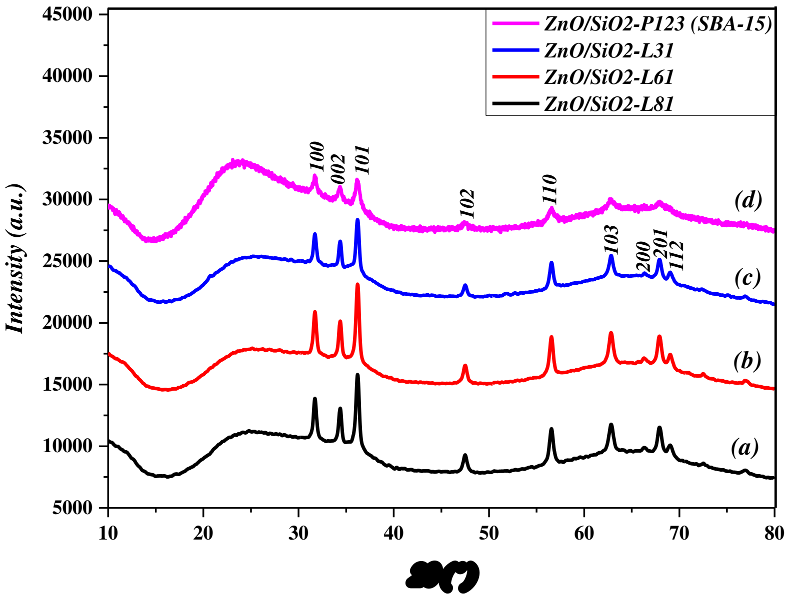

Figure 4.5.2 XRD pattern of (a) ZnO/SiO_2-L81, (b) ZnO/SiO_2-L61, (c) ZnO/SiO_2-L31 and (d) ZnO/SiO_2-P123 (SBA-15).

4.5.3 Small angle X- ray scattering (SAXS)

Figure 4.5.3 (a & b) shows SAXS pattern of SiO_2-L81 and ZnO/SiO_2-L81, respectively. SAXS pattern of ZnO/SiO_2-L81 (Fig.4.5.3b) shows two well-resolved peaks indexed as (001) and (002) reflections were corresponded to lamellar structure as identical to that of SiO_2-L81 (Fig.4.5.3a). This indicates that the addition of ZnO nanoparticles with a controlled amount in synthetic system does not obviously change the lamellar structure of SiO_2-L81 (Wang *et al.*, 2005; Lu *et al.*, 2009).

Figure 4.5.4 (a & b) shows SAXS pattern of SiO_2-P123 (SBA-15) and ZnO/SiO_2-P123 (SBA-15), respectively. SAXS pattern of ZnO/SiO_2-P123 (SBA-15) (Fig.4.5.4b) is similar to the pattern of SiO_2-P123 (SBA-15) (Fig.4.5.4a). It showed a typical pattern of a hexagonal phase with the occurrence of a strong peak, due to the (100) plane, and other two weak peaks, due to the (110) and (200) planes. This provides evidence that the addition of inorganic precursors does not alter the mesoscopic order of SiO_2-P123 (SBA-15) silica. There was a shift of all three peaks to a small q value after impregnation process. This results of increasing the inter-planar spacing, this suggest that the insertion of metal oxides is probably associated with expantion of the mesoporous silica (El-Nahhal *et al.*, 2016).

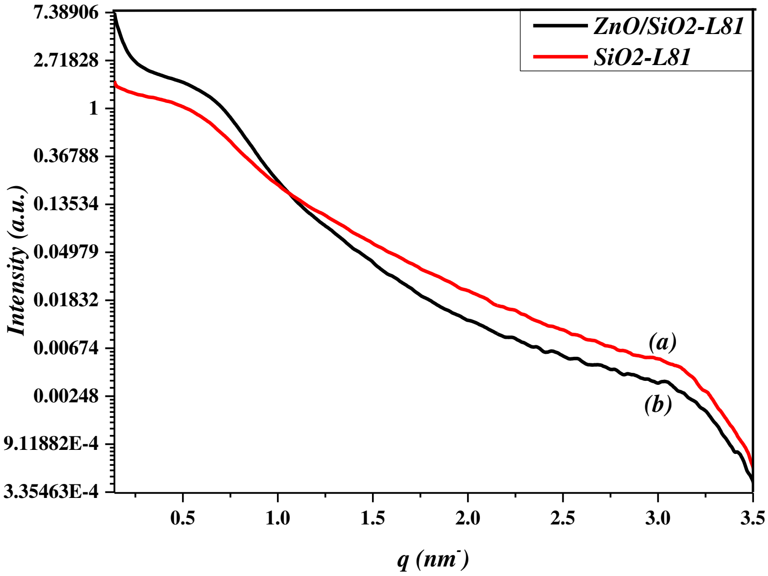

Figure 4.5.3 SAXS pattern of (a) SiO_2-L81 and (b) ZnO/SiO_2-L81.

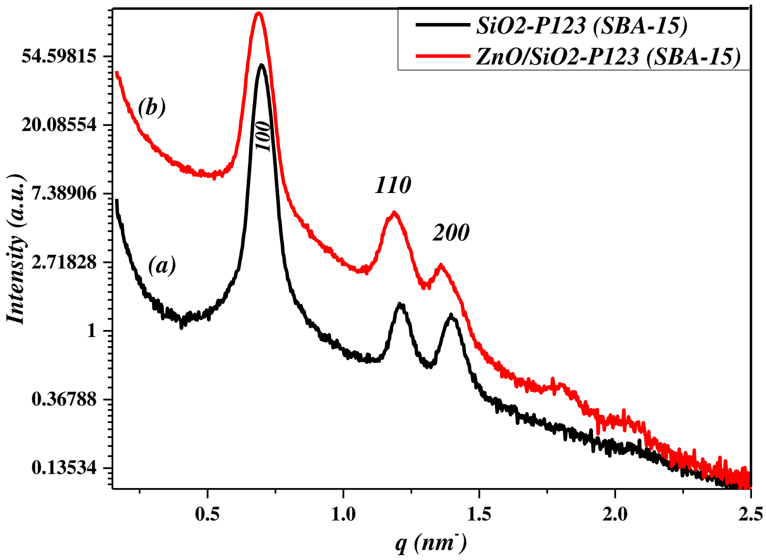

Figure 4.5.4 SAXS pattern of (a) SiO_2-P123 (SBA-15) and (b) ZnO/SiO_2-P123 (SBA-15).

4.5.4 Transmission electron microscopy (TEM)

Figure 4.5.5 (a-d) shows TEM image of SiO_2-L81, ZnO/SiO_2-L81, ZnO/SiO_2-L61 and ZnO/SiO_2-L31, respectively. The TEM image of SiO_2-L81 (Fig. 4.5.5a) shows short channel shape of grey color. Figure 4.5.5b shows hexagonal ZnO nanoparticles which are probably adsorbed onto the outside SiO_2-L81, some other ZnO particles are probably encapsulated into the silica and appear as dark color. Figure 4.5.5c shows ZnO/SiO_2-L61, where mesoporous silica is appeared in grey color, while dark color corresponds to impregnated ZnO nanoparticles into its silica network. In case of ZnO/SiO_2-L31 (Figure 4.5.4d), TEM image shows some channel shape of mesoporous silica in gray color, while a dark color indicates ZnO nanoparticles are impregnated into mesopores of SiO_2-L31.

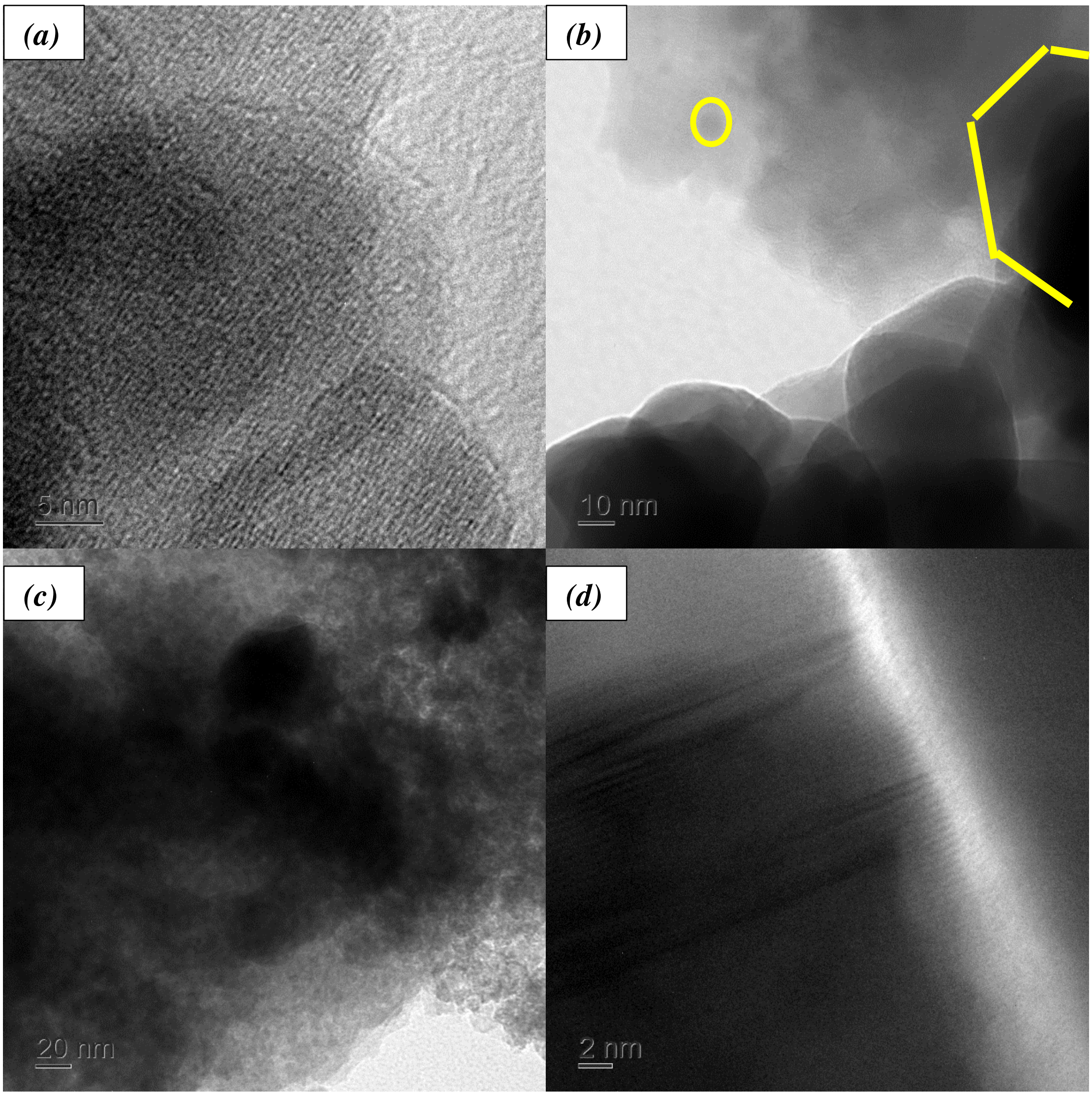

Figure 4.5.5 TEM image of (a) SiO_2-L81, (b) ZnO/SiO_2-L81, (c) ZnO/SiO_2-L61 and (d) ZnO/SiO_2-L31.

4.5.5 Thermal gravimetric analysis (TGA)

Thermal gravimetric analysis (TGA) used to determine chemical changes, which result as changes in mass when material is heated. Thermal gravimetric analysis (TGA) and differential thermal analysis (DTA) are examined for SiO_2-L81, ZnO/SiO_2-L81 and ZnO/SiO_2-P123 (SBA-15) (Fig.4.5.6 & Fig.4.5.7) under nitrogen at 25-600 ^{o}C at rate 10 ^{o}C/min, respectively. TGA-DTA patterns of SiO_2-L81 (Fig.4.5.6a & Fig.4.5.7a) show two steps of weight loss. The first step occurs at 75 ^{o}C due to loss of 1.4 % is attributed to loss of physisorbed water from the system pores. The second region occurs at 300 ^{o}C is due to loss of 1.3 %, which is probably due to the condensation reaction of silanol (Si–OH) groups (Zhang & Li, 2013). The total loss is about 2.7 % of its initial weight.

TGA-DTA pattern of ZnO/SiO_2-L81 (Fig.4.5.6b & Fig.4.5.7b) shows two steps of weight loss. The first step occurs at 75 °C due to 5.5 % weight loss, which is attributed to loss of physisorbed water on the surface of metal and silica pores. The second step occurs at 300 – 600 °C is due to 3% weight loss, which correspond to dehydroxylation of silanol and formation of siloxane bonds (El-Nahhal *et al.*, 2016; Nagajyothi *et al.*, 2015; Zhang & Li, 2013). The total weight loss is 8.5 %.

TGA-DTA pattern of ZnO/SiO_2-P123 (SBA-15) (Fig.4.5.6c & Fig.4.5.7c) shows two steps of weight loss. The first step occurs at 80 °C is due to 2.5 % weight loss, which is attributed to loss of adsorbed H_2O on the surface of metal and silica pores. The second step occurs at wide range 200 – 600 °C due to 3.5 % weight loss, which is corresponded to dehydroxylation of silanol and formation of siloxane bonds (El-Nahhal *et al.*, 2016; Nagajyothi *et al.*, 2015; Zhang & Li, 2013). The total loss is about 5 % of initial weight.

The difference in the weight loss in the first step between the silica and the encapsulated ZnO nanoparticles refers to the presence of crystallize water molecules of the metal oxide (Fig.4.5.7). It seems that more ZnO nanoparticles absorbed onto SiO2-L81 than SiO_2-P123 (SBA-15) silica.

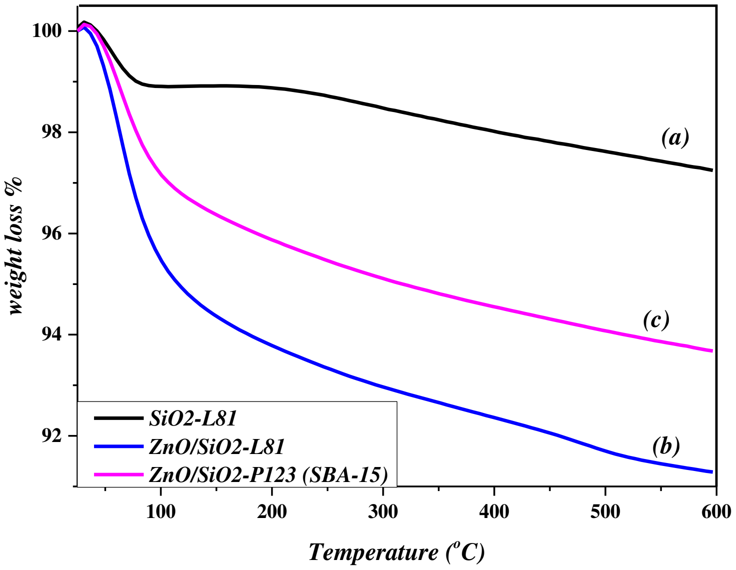

Figure 4.5.6 TGA pattern of (a) SiO_2-L81, (b) ZnO/SiO_2-L81 and (c) ZnO/SiO_2-P123(SBA-15).

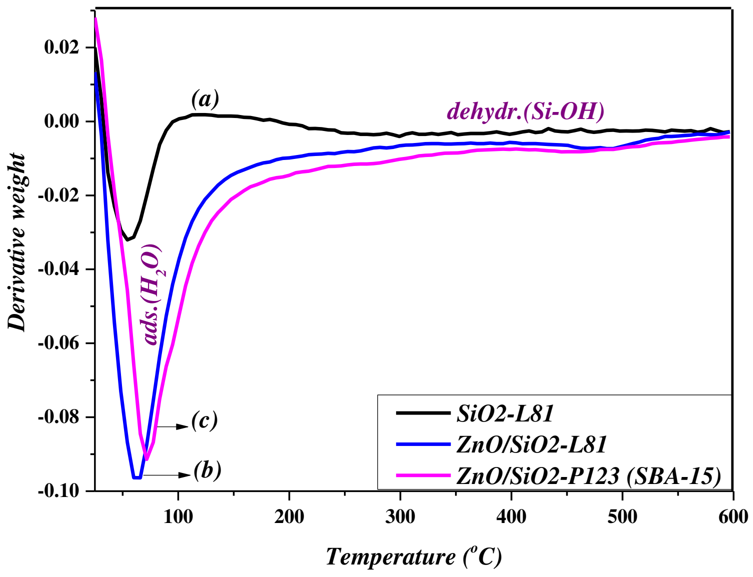

Figure 4.5.7 DTA pattern of (a) SiO_2-L81, (b) ZnO/SiO_2-L81 and (c) ZnO/SiO_2-P123 (SBA-15).

4.6 CuO/mesoporous silica

4.6.1 Fourier transform infrared (FTIR)

Figure 4.6.1 (a-d) shows FTIR spectra of CuO, SiO_2-L81, CuO/SiO_2-L81 and CuO/ SiO_2-P123 (SBA-15), respectively. Three absorption regions at 3400-3600 cm^{-1}, 1500-1700 cm^{-1} and 400-1200 cm^{-1} are detected due to ν(O-H); δ(O-H); ν(Cu-O) and (Si-O-Si) vibrations, respectively. The broad peak centered at 3500 cm^{-1} is associated with (O–H) stretching vibration of hydrogen bonding of absorbed water molecule on CuO (Fig.4.6.1a) and silica surfaces (Figs.4.6.1 (b-d)) (El-Nahhal *et al.*, 2016; Yang *et al.*, 2008). The peaks at 1625 cm^{-1} (Fig.4.6.1a) and 1645 cm^{-1} (Figs.4.6.1(b-d)) are related to bending vibration (O-H) of hydroxyl groups (El-Nahhal *et al.*, 2016; Wu *et al.*, 2013; Yang *et al.*, 2008). The absorption peaks at 1087 cm^{-1} (broad), 800 cm^{-1} and 459 cm^{-1} (Figs.4.6.1 (b-d)) are due to asymmetric, symmetric stretching and bending vibration of (Si-O-Si) vibrations from silica network, respectively (Wu *et al.*, 2013; Yang *et al.*, 2008). The absorption peak at 1080 cm^{-1} (Fig.4.6.1a) is due to stretching vibration of (Cu-O-Cu) bridging. The peak around 480 cm^{-1} (Fig.4.6.1a) is due to stretching vibration of Cu-O (El-Nahhal *et al.*, 2016). The decreasing of this medium peak for pure CuO (Fig.4.6.1a) to a shoulder at 560 cm^{-1} (Figs.4.6.1(c & d)) for encapsulated CuO is a good evidence for the success of encapsulation process.

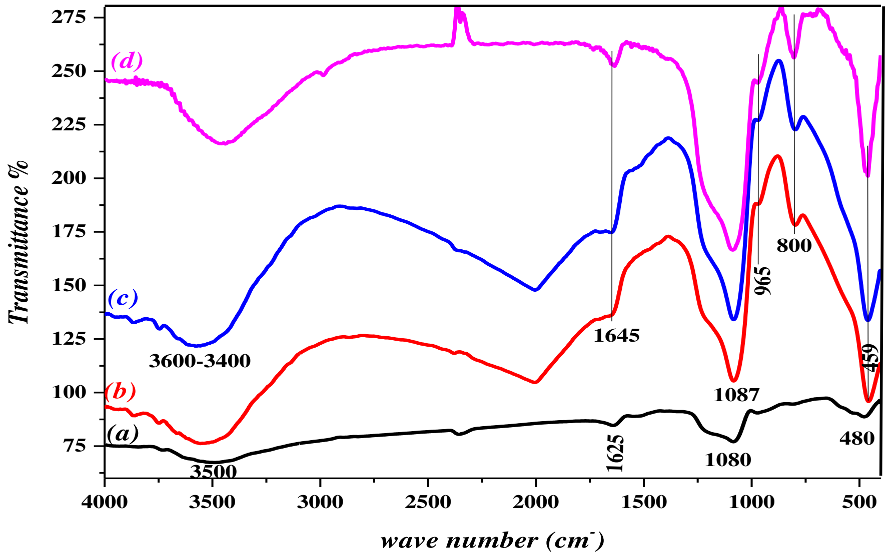

Figure 4.6.1 FTIR spectra of (a) CuO, (b) SiO_2-L81, (c) CuO/SiO_2-L81 and (d) CuO/SiO_2-P123 (SBA-15).

4.6.2 X- ray diffraction (XRD)

Figure 4.6.2 (a-d) shows XRD patterns of CuO/SiO_2-P123 (SBA-15), CuO/SiO_2-L31, CuO/SiO_2-L61 and CuO/SiO_2-L81, respectively. All the peaks in the diffraction pattern indicate to the monoclinic phase of CuO, which is in good consistent with (JCPDS no. 05-0661) (Dong *et al.*, 2015). Diffraction peaks related to impurities were not found in XRD patterns, which confirm high purity of synthesized materials. In Figure 4.6.2 (a-d), the obvious main peaks correspond to (110), (-111), (111), (-202), (020), (202), (-113), (-311), (220) (Dong *et al.*, 2015; El-Nahhal *et al.*, 2016). CuO diffraction peaks in SiO_2-L81, SiO_2-L61 and SiO_2-L31 were more intense than in SiO_2-P123 (SBA-15). The low intensity peaks for CuO/SiO_2-P123 (SBA-15) is probably due to entrapment of CuO particles inside the pores in comparison with that of other mesoporous silica materials. Scherer's equation determines the crystallite mean size. Scherer's equation was used to calculate the mean crystallite size of CuO encapsulated onto SiO_2-P123 (SBA-15), SiO_2-L81, SiO_2-L61 and SiO_2-L31 were estimated and listed Table 4.1.

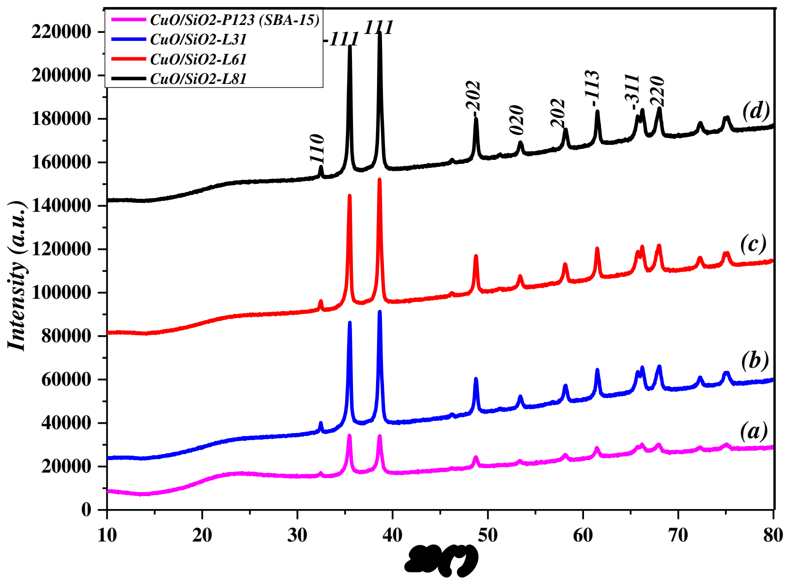

Figure 4.6.2 XRD pattern of (a) CuO/SiO_2-P123 (SBA-15), (b) CuO/SiO_2-L31, (c) CuO/SiO_2-L61 and (d) CuO/SiO_2-L81.

4.6.3 Small angle X- ray scattering (SAXS)

Figure 4.6.3 (a & b) shows SAXS patterns of SiO_2-L81 and CuO/SiO_2-L81, respectively. SAXS pattern of CuO/SiO_2-L81 (Fig.4.6.3b) shows two well-resolved peaks indexed as (001) and (002) reflections corresponding to lamellar structure. This indicates that the addition of CuO with a controlled amount in synthetic system does not alter the mesoscopic order of SiO_2-L81 (Wang *et al.*, 2005).

Figure 4.6.4 (a & b) shows SAXS patterns of SiO_2-P123 (SBA-15) and CuO/SiO_2-P123 (SBA-15), respectively. SAXS pattern of CuO/SiO_2-P123 (SBA-15) (Fig.4.6.4b) is similar to the patterns of SiO_2-P123 (SBA-15) (Fig.4.6.4b). It showed a typical pattern of a hexagonal phase with the occurrence of a strong peak, due to the (100) plane, and other two weak peaks, due to the (110) and (200) planes. This provides evidence that the addition of inorganic precursors does not alter the mesoscopic order of SiO_2-P123 (SBA-15) silica. There was a shift of all three peaks to a smaller angle after impregnation process. This results of increasing the inter-planar spacing, this suggest that the insertion of metal oxides is probably associated with expansion of the mesoporous silica (El-Nahhal *et al.*, 2016).

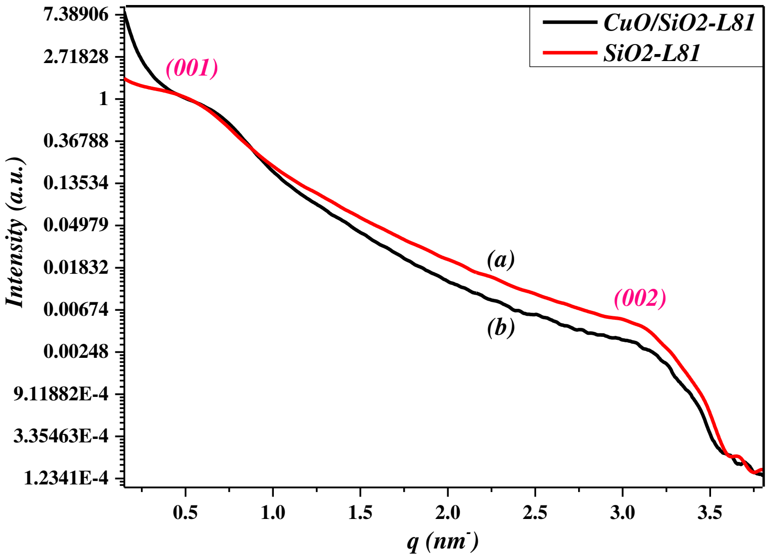

Figure 4.6.3 SAXS pattern of (a) SiO_2-L81 and (b) CuO/SiO_2-L81.

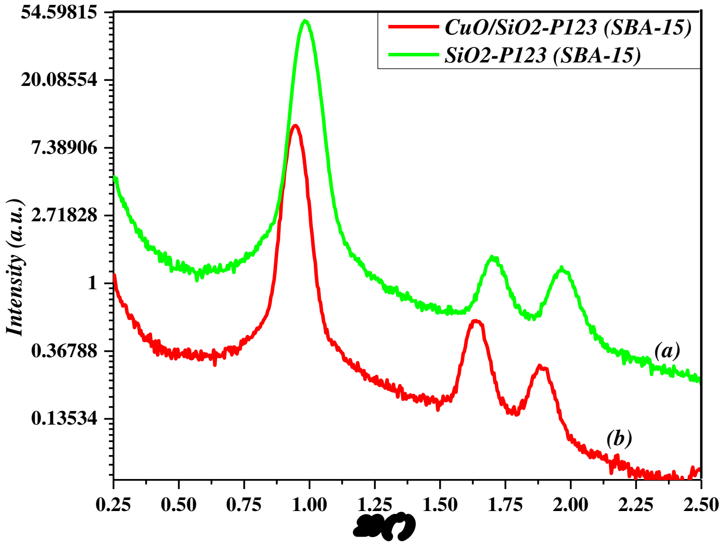

Figure 4.6.4 SAXS pattern of (a) SiO_2-P123 (SBA-15) and (b) CuO/SiO_2-P123 (SBA-15).

4.6.4 Transmission electron microscopy (TEM)

TEM analysis is used to study the morphology of the product. Figure 4.6.5 (a & b) shows TEM image of SiO_2-L81 and CuO/SiO_2-L81, respectively. CuO nanoparticles are seen in dark and the mesoporous silica are seen in grey color.

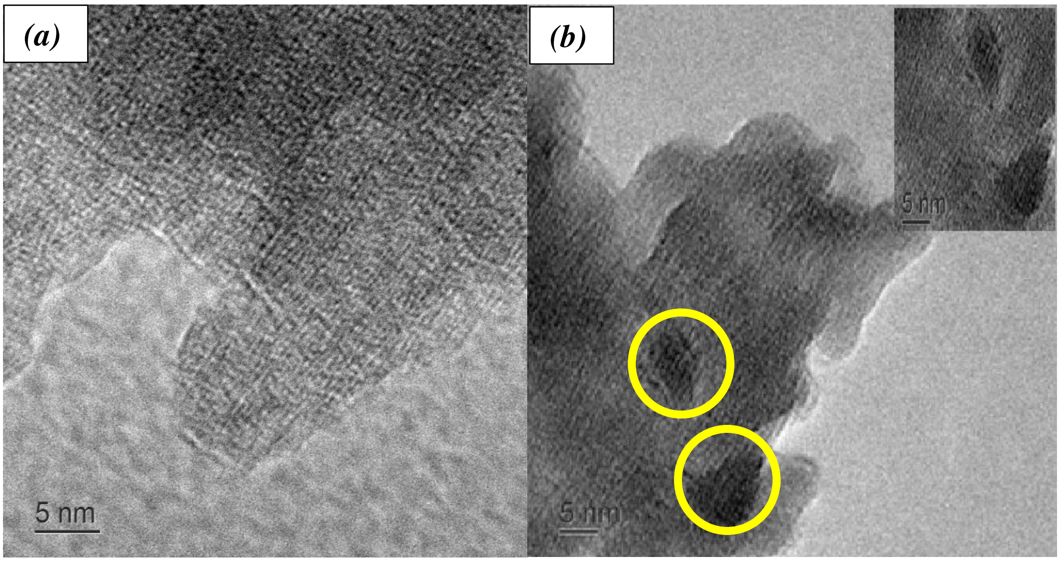

Figure 4.6.5 TEM image of (a) SiO_2-L81 and (b) CuO/SiO_2-L81.

4.6.5 Thermal gravimetric analysis (TGA)

Thermal gravimetric analysis (TGA) used to determine chemical changes, which result as changes in mass when material is heated. Thermal gravimetric analysis

(TGA) and differential thermal analysis (DTA) are examined for SiO_2-L81, CuO/SiO_2-L81 and CuO/SiO_2-P123 (SBA-15) (Fig.4.6.6 & Fig.4.6.7) under nitrogen at 25-600 ^{o}C at rate 10 ^{o}C/min, respectively. TGA-DTA pattern of SiO_2-L81 (Fig.4.6.6a & Fig4.6.7a) shows two-loss weight steps. The first step occurs at 75 ^{o}C is due to loss of 1.4 % of its initial weight. This attributed to loss of physisorbed water from the system pores. The second step occurs at 300 ^{o}C is due to loss of 1.3 %, which is probably due to the condensation reaction of silanol (Si–OH) groups (Zhang & Li, 2013). The total weight loss is 2.7 %.

TGA-DTA patterns of CuO/SiO_2-L81 (Fig.4.6.6b & Fig.4.6.7b) show two steps of weight loss. The first step occurs 80 ^{o}C is due to 5 % weight loss, which is attributed to loss of adsorbed H_2O on the surface of metal and silica pores. The second step occurs over wide range at 200–600 ^{o}C is due to 2 % weight loss, which is corresponded to dehydroxylation of silanol and formation of siloxane bonds (El-Nahhal *et al.*, 2016; Zhang & Li, 2013). The total weight loss is 7 %.

TGA-DTA patterns of CuO/SiO_2-P123 (SBA-15) (Fig.4.6.6c & Fig4.6.7c) shows two steps of weight loss. The first step occurs 80 ^{o}C is due to 3 % weight loss, which is attributed to loss of adsorbed H_2O on the surface of metal and silica pores. The second step occurs over wide range at 200–600 ^{o}C is due to 2.3 % weight loss, which is corresponded to dehydroxylation of silanol and formation of siloxane bonds (El-Nahhal *et al.*, 2016; Zhang & Li, 2013). The total weight loss is 5.3 %.

The difference in the weight loss in the first step beween the silica and the encapsulated CuO nanoparticles refers to the presence of crystallize water molecules of the metal oxide. It seems that more CuO nanoparticles are absorbed onto SiO2-L81 than SiO_2-P123 (SBA-15) silica.

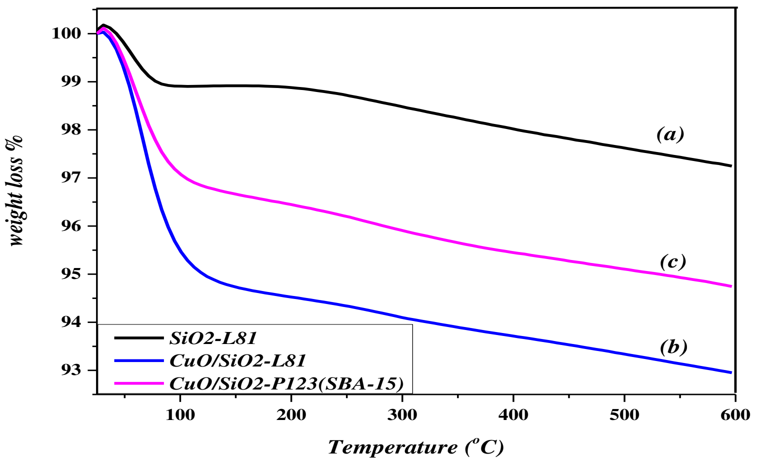

Figure 4.6.6 TGA pattern of (a) SiO_2-L81, (b) CuO/SiO_2-L81 and (c) CuO/SiO_2-P123 (SBA-15).

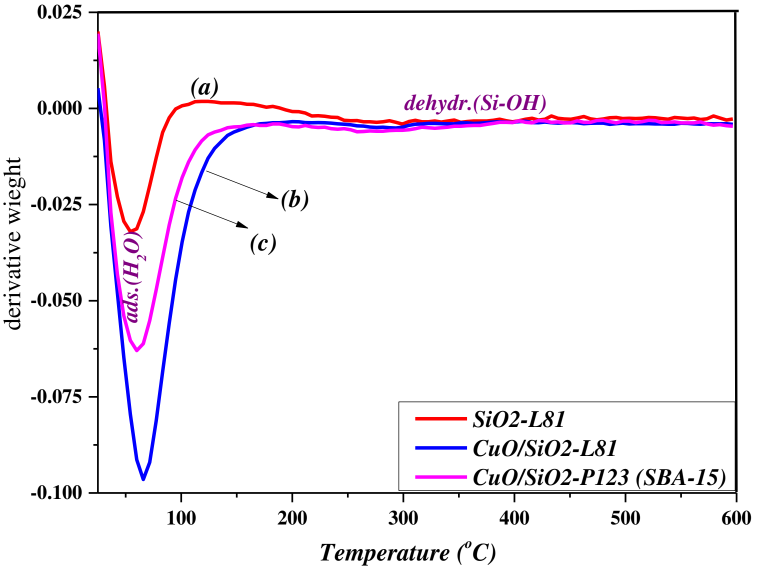

Figure 4.6.7 DTA pattern of (a) SiO_2-L81, (b) CuO/SiO_2-L81 and (c) CuO/SiO_2-P123 (SBA-15).

Table 4.2 Experimental description

Materials	**Synthesis description**	**Material description**
CaO/SiO_2-P123 (SBA-15)	$CaCO_3$+acetic acid → $Ca(CH_3COO)_2$+ SiO_2-P123(SBA-15) $\xrightarrow[\text{2) dried at 100 °C in oven}]{\text{1) stirring at 80 °C to dryness}}$ calcination (600 °C, 4 h)	A fine white powder material appearance.
CaO/SiO_2-L81	$CaCO_3$+acetic acid → $Ca(CH_3COO)_2$+ SiO_2-L81 $\xrightarrow[\text{2) dried at 100 °C in oven}]{\text{1) stirring at 80 °C to dryness}}$ calcination (600 °C, 4h)	A dark mixture contain CaO, $Ca(OH)_2$ & $CaCO_3$ is encapsulated into grey silica

CaO/SiO_2-L61	$CaCO_3$+acetic acid → $Ca(CH_3COO)_2$+ SiO_2-L61 $\xrightarrow[\text{2) dried at 100 °C in oven}]{\text{1) stirring at 80 °C to dryness}}$ calcination (600 °C, 4 h)	Dark CaO-NPs encapsulated in grey silica
CaO/SiO_2-L31	$CaCO_3$+acetic acid → $Ca(CH_3COO)_2$+ SiO_2-L31 $\xrightarrow[\text{2) dried at 100 °C in oven}]{\text{1) stirring at 80 °C to dryness}}$ calcination (600 °C, 4 h)	Cross net shape in grey color occupied by CaO-NPs in dark color
MgO/SiO_2-P123 (SBA-15)	$Mg(CH_3COO)_2$+ SiO_2-P123(SBA-15) $\xrightarrow[\text{2) dried at 100 °C in oven}]{\text{1) stirring at 80 °C to dryness}}$ calcination (600 °C, 4 h)	Fine white powder appearance.
MgO/SiO_2-L81	$Mg(CH_3COO)_2$+ SiO_2-L81 $\xrightarrow[\text{2) dried at 100 °C in oven}]{\text{1) stirring at 80 °C to dryness}}$ calcination (600 °C, 4 h)	Noncrystalline MgO-NPs encapsulated meso-silica
MgO/SiO_2-L61	$Mg(CH_3COO)_2$+ SiO_2-L61 $\xrightarrow[\text{2) dried at 100 °C in oven}]{\text{1) stirring at 80 °C to dryness}}$ calcination (600 °C, 4 h)	Cubic MgO-NPs encapsulated mesoporous silica
MgO/SiO_2-L31	$Mg(CH_3COO)_2$+ SiO_2-L31 $\xrightarrow[\text{2) dried at 100 °C in oven}]{\text{1) stirring at 80 °C to dryness}}$ calcination (600 °C, 4 h)	
ZnO/SiO_2-P123 (SBA-15)	$Zn(CH_3COO)_2$+ SiO_2-P123(SBA-15) $\xrightarrow[\text{2) dried at 100 °C in oven}]{\text{1) stirring at 80 °C to dryness}}$ calcination (600°C, 4h)	ZnO-NPs impregnated into silica pores, with expantion of silica walls.
ZnO/SiO_2-L81	$Zn(CH_3COO)_2$+ SiO_2-L81 $\xrightarrow[\text{2) dried at 100 °C in oven}]{\text{1) stirring at 80 °C to dryness}}$ calcination (600 °C, 4 h)	large hexagonal ZnO-NPs outside the silica, some other ZnO-NPs encapsulated into the silica in dark color
ZnO/SiO_2-L61	$Zn(CH_3COO)_2$+ SiO_2-L61 $\xrightarrow[\text{2) dried at 100 °C in oven}]{\text{1) stirring at 80 °C to dryness}}$ calcination (600 °C, 4 h)	Dark ZnO-NPs encapsulated in grey silica
ZnO/SiO_2-L31	$Zn(CH_3COO)_2$+ SiO_2-L31 $\xrightarrow[\text{2) dried at 100 °C in oven}]{\text{1) stirring at 80 °C to dryness}}$ calcination (600 °C, 4 h)	Dark ZnO-NPs as nanowire impregnated into grey silica channel
CuO/SiO_2-P123 (SBA-15)	$Cu(CH_3COO)_2$+ SiO_2-P123(SBA-15) $\xrightarrow[\text{2) dried at 100 °C in oven}]{\text{1) stirring at 80 °C to dryness}}$ calcination (600°C, 4h)	CuO-NPs impregnated into silica pores, with expantion of silica walls.
CuO/SiO_2-L81	$Cu(CH_3COO)_2$+ SiO_2-L81 $\xrightarrow[\text{2) dried at 100 °C in oven}]{\text{1) stirring at 80 °C to dryness}}$ calcination (600 °C, 4 h)	Dark CuO-NPs encapsulated into grey silica.
CuO/SiO_2-L61	$Cu(CH_3COO)_2$+ SiO_2-L61 $\xrightarrow[\text{2) dried at 100 °C in oven}]{\text{1) stirring at 80 °C to dryness}}$ calcination (600 °C, 4 h)	Monoclinic CuO-NPs impregnated into lamellar silica

CuO/SiO_2-L31	$Cu(CH_3COO)_2$+ SiO_2-L31 $\xrightarrow[\text{2) dried at 100 }^{o}\text{C in oven}]{\text{1) stirring at 80 }^{o}\text{C to dryness}}$ calcination (600 ^{o}C, 4 h)	Monoclinic CuO-NPs impregnated into lamellar silica

4.7 Conclusion

Metal oxides (CaO, MgO, CuO and ZnO) are encapsulated into/onto mesoporous silica materials using impregnation method. Four different mesoporous silica host materials are involved (SiO_2-P123 (SBA-15), SiO_2-L81, SiO_2-L61 and SiO_2-L31). Several characterization techniques were used to investigate the structural properties of the synthesized metal oxides encapsulated mesoporous silica materials include fourier transform infrared spectroscopy (FTIR), X- ray diffraction (XRD), small angle X- ray scattering (SAXS), transmission electron microscopy (TEM) and thermal gravimetric analysis (TGA).

FTIR spectra show that metal oxides were physically bonded with silanol group within silica pores. Because there is no obvious change in the spectrum of metal oxide encapsulated mesoporous silica and the spectrum of mesoporous silica itself.

For CuO and ZnO encapsulated mesoporous silica XRD patterns prove that CuO and ZnO encapsulated mesoporous silica are in crystalline form and there is no presence of metal hydroxide form or other impurities. SAXS results for CuO and ZnO encapsulated mesoporous silica SiO_2-P123 (SBA-15) show that these metal oxides were physically bonded with silanol group inside silica pores.

For CaO encapsulated mesoporous silica, XRD pattern shows a presence of other reflection peaks due to $Ca(OH)_2$ (with high intensity) and $CaCO_3$ (with low intensity). $CaCO_3$ presence illustrates rapid carbonation of CaO by atmospheric CO_2 in comparison with other metal oxides. TGA is also confirmed the carbonation of CaO with a loss weight step at 440 ^{o}C.

For MgO encapsulated mesoporous silica, XRD patterns show that MgO takes two forms, a crystalline form for MgO/SiO_2-L31 and MgO/SiO_2-L61. While MgO/SiO_2-L81 takes non-crystalline form with no XRD reflection peaks. TEM and SAXS confirm that MgO is loaded into/onto mesoporous silica affect the lamellar structure of the mesoporous silica.

SAXS and TEM results for CaO, CuO and ZnO encapsulated onto mesoporous silica SiO_2-L81, SiO_2-L61 & SiO_2-L31 confirmed that these metal oxides are mostly loaded onto the surface of the silica and do not affect or change the lamellar structure of the mesoporous silica.

TGA thermograms confirm the thermal stability of the synthesized encapsulated metal oxides mesoporous silica materials at high temperature. From XRD patterns, the mean particle size of each metal oxide altered with the type of mesoporous silica (Table 4.1).

Chapter Five

Results and Discussion

Synthesis and characterization of curcumin–metal(II) encapsulated mesoporous silica complexes.

5.1 Introduction

We used batch method to prepare curcumin metal(II) complexes, where each of MO/mesoporous silica systems were mixed with ethanolic curcumin solution. Several methods and techniques were used for structural characterization of these new materials. These methods include fourier transform infrared spectroscopy (FTIR), X-ray diffraction (XRD), small angle X- ray scattering (SAXS), transmission electron microscopy (TEM), thermal gravimetric analysis (TGA) and ultraviolet-visible spectroscopy (UV-vis).

5.2 Synthesis

Curcumin-metal(II) complex was prepared by treatment of encapsulated metal oxide/ mesoporous silica to curcumin ethanolic solution under shaking to accelerate the reaction (Scheme 5.2). curcumin is present in keto-form (a), enol-form (b) and curcumin anion (c) as given in scheme 5.1.

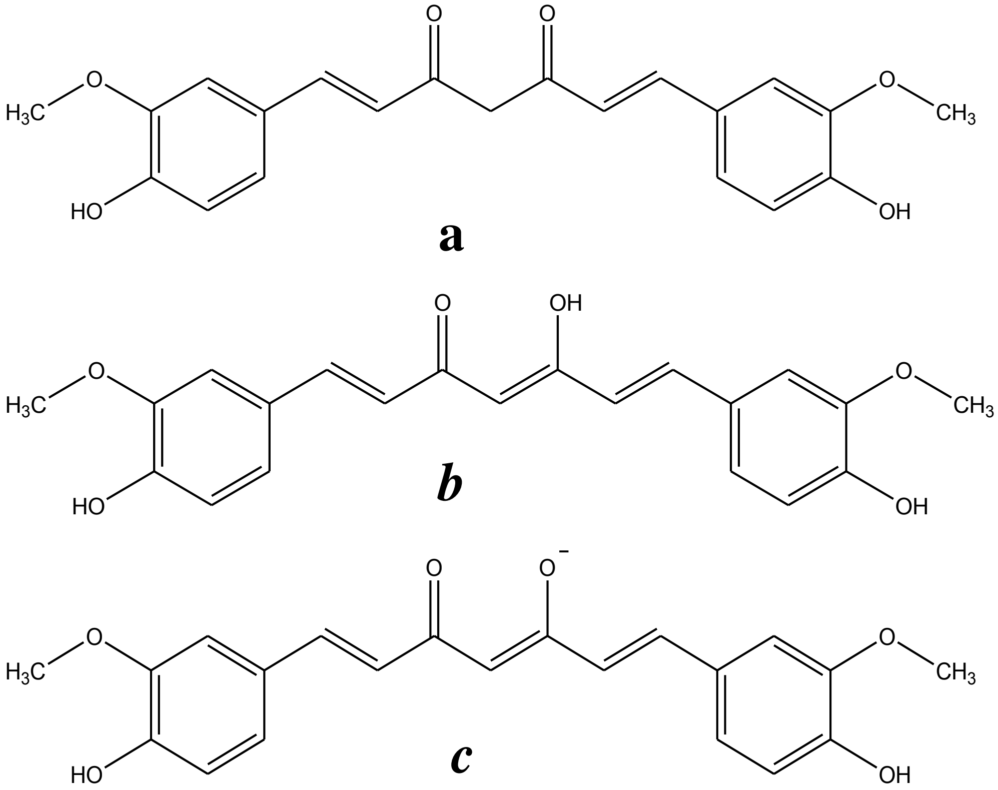

Scheme 5.1 Structure of curcumin (a) keto-form, (b) enol-form and (c) curcumin anion.

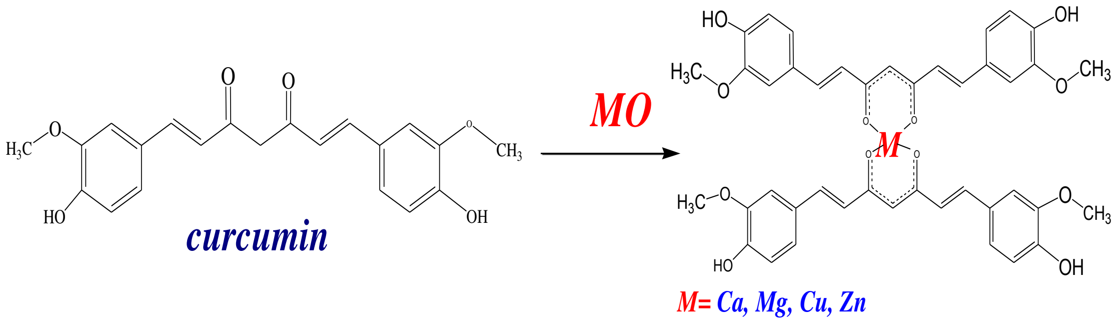

Scheme 5.2 Synthesis of curcumin – metal(II) complex.

5.3 Fourier transform infrared (FTIR)

Figure 5.1 shows FTIR spectra of curcumin. The presence of a sharp absorption peak at 3513 cm^{-1} related to phenolic –OH stretching vibration (Subhan *et al.*, 2013). The small peaks at 3023 cm^{-1} and 2970 cm^{-1} are due to the aromatic (C-H) and methyl (C–H) stretching vibration, respectively (Subhan *et al.*, 2013). The most prominent band in the IR spectrum at 1420-1630 cm^{-1} attributed to the mixture of stretching vibrations of (C=C) and C=O stretching vibration of curcumin (Gangwar *et al.*, 2013; Mohan *et al.*, 2012; Subhan *et al.*, 2013). C=O stretching vibration appears at low frequency due to high conjugation system. The peaks at 1277 cm^{-1} is attributed to enol and phenol (C–O) stretching vibrations (Mohan *et al.*, 2012). An absorption band centered at 1161 cm^{-1} correspond to the in-plane deformation vibration of phenyl rings. The peak at 1026 cm^{-1} is related to C–O–C vibration and benzoate trans-CH vibration at 961 cm^{-1} (Mohan *et al.*, 2012). The peak at 864 cm^{-1} belongs to the C-H out-of-plane vibration of aromatic rings. The IR band at 820 cm^{-1} assigned to the highly mixed (C-H) and aromatic (C–CH) bending vibrations (Subhan *et al.*, 2013). The out-of-plane vibrations of both OH groups are found at 458 cm^{-1} (Mohan *et al.*, 2012; Subhan *et al.*, 2013).

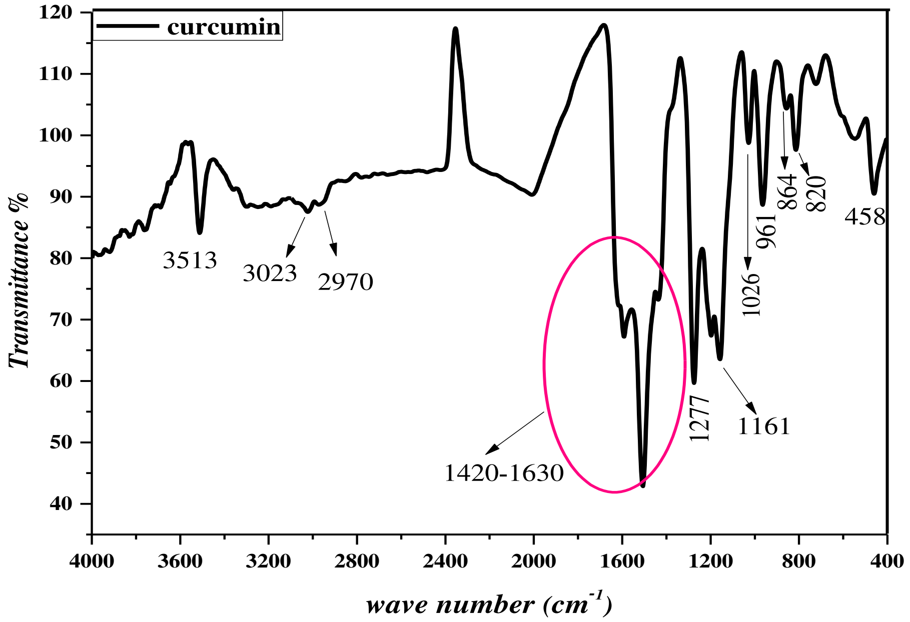

Figure 5.1 FTIR spectrum of curcumin

Figure 5.2 (a & b) shows FTIR spectra of CaO/SiO_2-L81 and curc-Ca(II)/SiO_2-L81, respectively. Three absorption regions are detected at 3000-3600 cm^{-1}, 1400-1800 cm^{-1} and 400-1300 cm^{-1} due to ν(O-H); ν(C-O) & δ(O-H); ν(Ca-O) and (Si-O-Si) vibrations, respectively. The sharp peak at 3643 cm^{-1} (Figs. 5.2b) is due to ν(O-H) of $Ca(OH)_2$. The broad band at 3400-3600 cm^{-1} (Figs.5.2 (a & b)) due to ν(O-H) of hydrogen bonded of hydroxyl groups with silica (Yang *et al.*, 2008; Zaki *et al.*, 2006). A peak at 1645 cm^{-1} (Figs.5.2 (a & b)) is assigned due to δ(O-H) bending vibration of hydroxyl groups. The decrease of peak intensities of absorption peaks at 3400-3600 cm^{-1} and 1645 cm^{-1} (Fig.5.2b) is probably due to the complexation of curcumin with metal into/onto the silica pores. In Figure 5.2b, several peaks around 1511 cm^{-1} and 1428 cm^{-1} indicate curcumin – calcium complex (Zhao *et al.*, 2010; Mohanan, 2014). In Figure 5.2 (a & b), the three peaks at 1087 cm^{-1} (broad), 800 cm^{-1} and 459 cm^{-1} are due to (Si-O-Si) asymmetric, symmetric stretching and bending vibrations of silica network, respectively (Wu *et al.*, 2013; Yang *et al.*, 2008). The shoulder at about 510 cm^{-1} (Fig. 5.2a) is due to ν(Ca-O) for encapsulated CaO into mesoporous silica. The absence of this shoulder at 510 cm^{-1} (Fig.5.2b) is a good evidence for the formation of curcumin-calcium(II) complex. Other curcumin peaks are probably obscured within broad, intense mesoporous silica absorption peaks (Das, 2011).

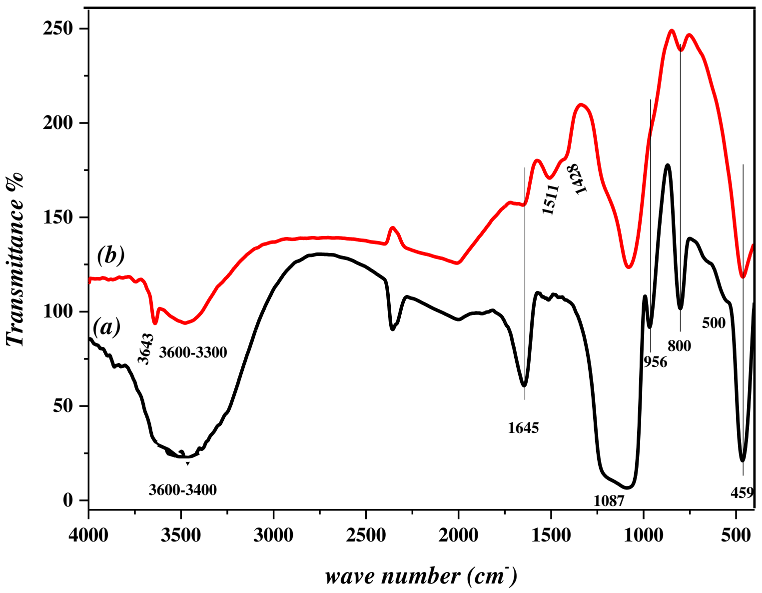

Figure 5.2 FTIR spectrum of (a) CaO/SiO_2-L81 and (b) curc-Ca(II)/SiO_2-L81.

5.4 X- ray diffraction (XRD)

XRD patterns for CaO/SiO_2-L81 and curc–Ca(II)/SiO_2-L81 are depicted in Figure 5.3 (a & b), respectively. CaO/SiO_2-L81 (Fig.5.3a) exhibits reflection peaks corresponded to CaO faced-center cubic structure (*), hexagonal structure $Ca(OH)_2$ ($) and $CaCO_3$ (♦) (Stutzman, 1996). After the interaction between CaO/SiO_2-L81 with curcumin, XRD exhibits reflection peaks corresponded to face-centered cubic structure of CaO (*) and hexagonal structure of $Ca(OH)_2$ and almost essential part of $CaCO_3$ reflection peaks are disappeared (Fig.5.3b) (Stutzman, 1996). The intensity of peaks corresponding to CaO decreases after intraction with curcumin. The obvious reason for this behavior is that only the surface CaO-NPs are in access for complexation with curcumin, but entrapped of CaO-NPs are not accessible for curcumin molecules. This is the reason behind that CaO-NPs at the surface are mostly converted to $CaCO_3$ which were consumed for the complexation with curcumin. Further evidence for the involvement of $CaCO_3$ in complexation with curcumin is confirmed by TGA (Fig.5.9), where there was a reduction of CO_2 weight loss peak after treatment with curcumin.

Figure 5.4 (a & b) shows XRD patterns of MgO/SiO_2-L81 and curc–Mg(II)/SiO_2-L81, respectively. No diffraction peaks were detected for MgO/SiO_2-L81 and curc-Mg(II)

/SiO_2-L81 (Fig.5.4 (a & b)). The absence of these peaks does not give an obvious indication about the formation of curcumin-Mg(II) complex.

Figure 5.5 (a & b) shows XRD pattern of CuO/SiO_2-L81 and curc–Cu(II)/SiO_2-L81, respectively. CuO/SiO_2-L81 (Fig.5.5a) exhibits reflection peaks corresponded to monoclinic phase of CuO (Dong *et al.*, 2015). Similar diffraction pattern was detected for curc–Cu(II)/SiO_2-L81 (Fig.5.5b) with less intense reflection peaks in comparison with CuO/SiO_2-L81. The presence of these reflections suggest that CuO is not completely react with curcumin.

Figure 5.6 (a & b) shows XRD pattern of ZnO/SiO_2-L81 and curc–Zn(II)/SiO_2-L81, respectively. ZnO/SiO_2-L81 (Fig.5.6a) exhibits reflection peaks correspond to wurtzite ZnO structure (İpeksaç *et al.*, 2013). Curc–Zn(II)/SiO_2-L81 XRD pattern (Fig.5.6b) has similar diffraction pattern of ZnO/SiO_2-L81 (Fig.5.6a) with a small decreasing in reflection intensities. The decreasing of intensity of reflection peaks of ZnO components indicates the curcumin complexation with Zn(II). The presence of ZnO reflections for curc-Zn(II)/SiO_2-L81 prove the presence of unreacted ZnO nanoparticles.

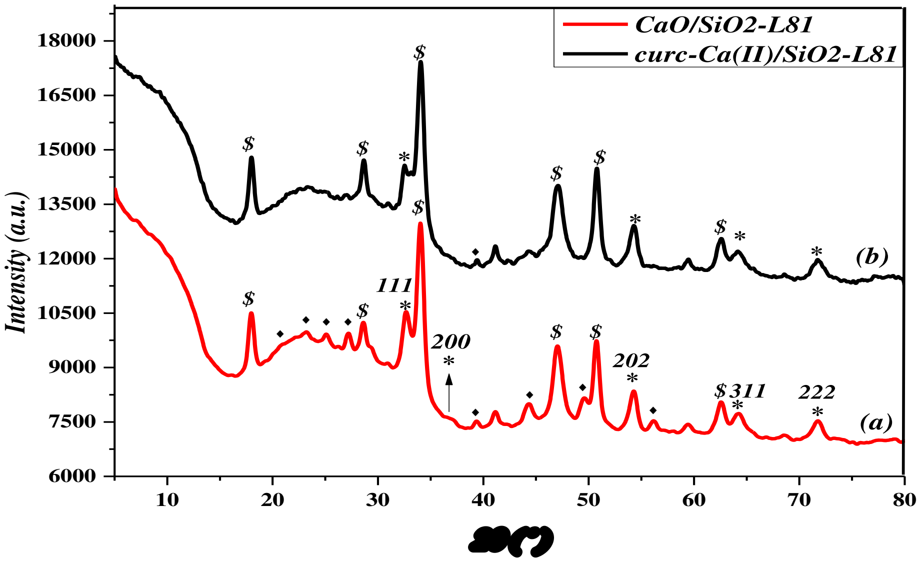

Figure 5.3 XRD pattern of (a) CaO/SiO_2-L81 and (b) curc–Ca(II)/SiO_2-L81.

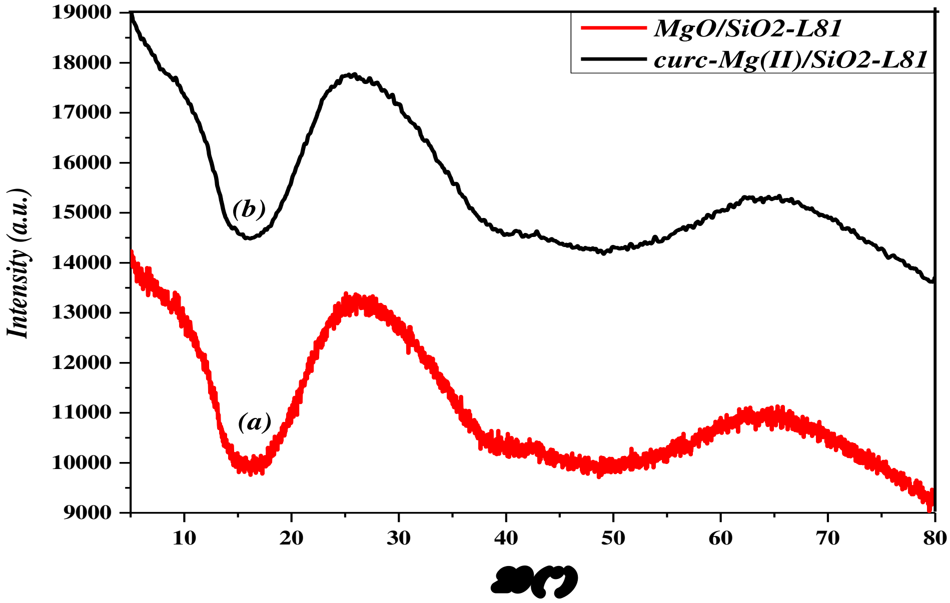

Figure 5.4 XRD pattern of (a) MgO/SiO_2-L81 and (b) curc–Mg(II)/SiO_2-L81.

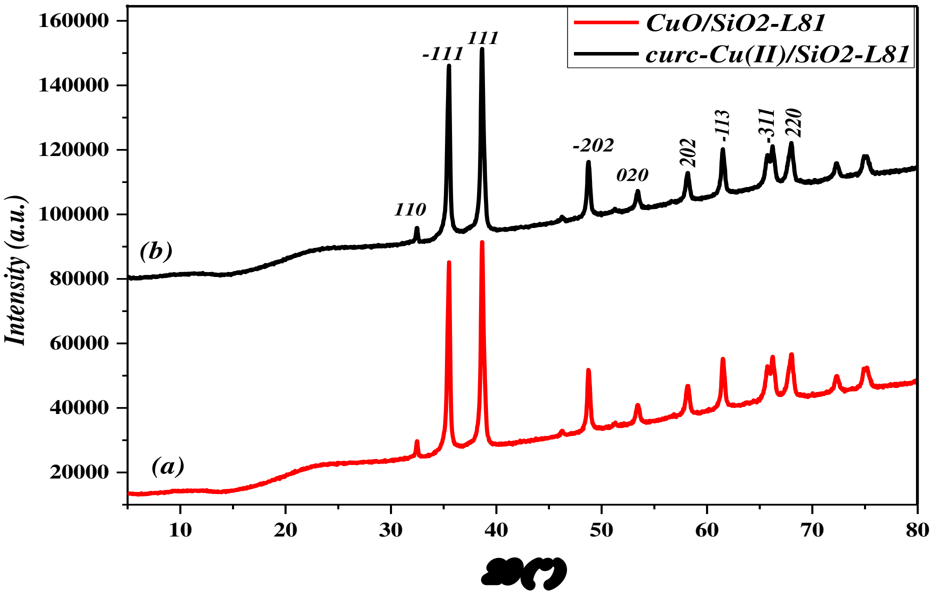

Figure 5.5 XRD pattern of (a) CuO/SiO_2-L81 and (b) curc–Cu(II)/SiO_2-L81.

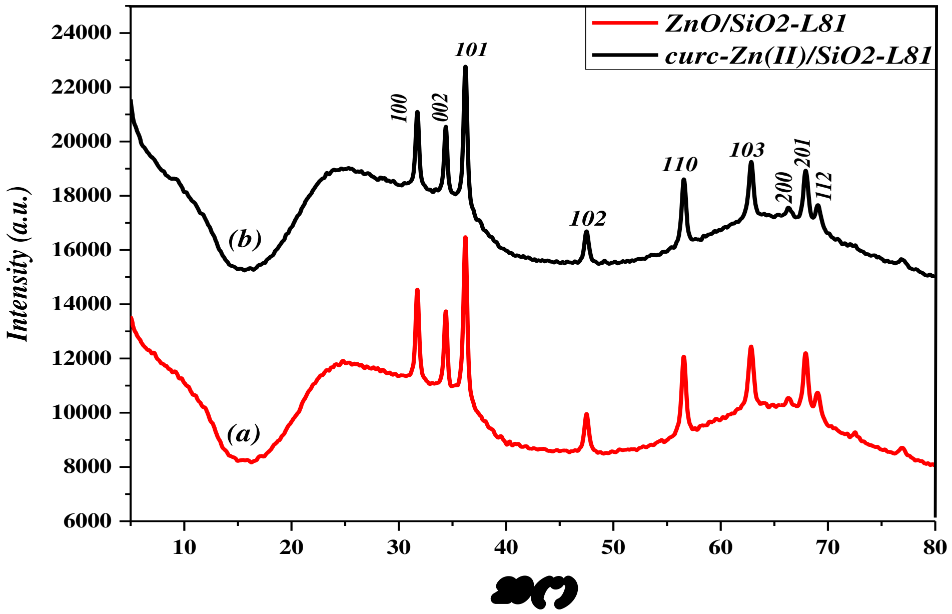

Figure 5.6 XRD pattern of (a) ZnO/SiO$_2$-L81 and (b) curc–Zn(II)/SiO$_2$-L81.

5.5 Small angle X- ray scattering (SAXS)

Figure 5.7 (a-c) shows SAXS pattern of SiO$_2$-L81, CaO/SiO$_2$-L81 and curc–Ca(II) /SiO$_2$-L81, respectively. SiO$_2$-L81 (Fig.5.7a) exhibits two reflection peaks related to (001) and (002) correspond to lamellar mesoscopic structure (Dovgolevsky *et al.*, 2008). In Figure 5.7b, the intensity of all reflections decrease, which indicates that pore blocking by CaO-NPs have partly destroyed the lamellar structure of SiO$_2$-L81 (Haung *et al.* 2010). Curc–Ca(II)/SiO$_2$-L81 SAXS pattern (Fig.5.7c) has similar SAXS pattern for CaO/SiO$_2$-L81. This suggests that the formation of curcumin-calcium(II) complex does not alter the mesoscopic structure of SiO$_2$-L81.

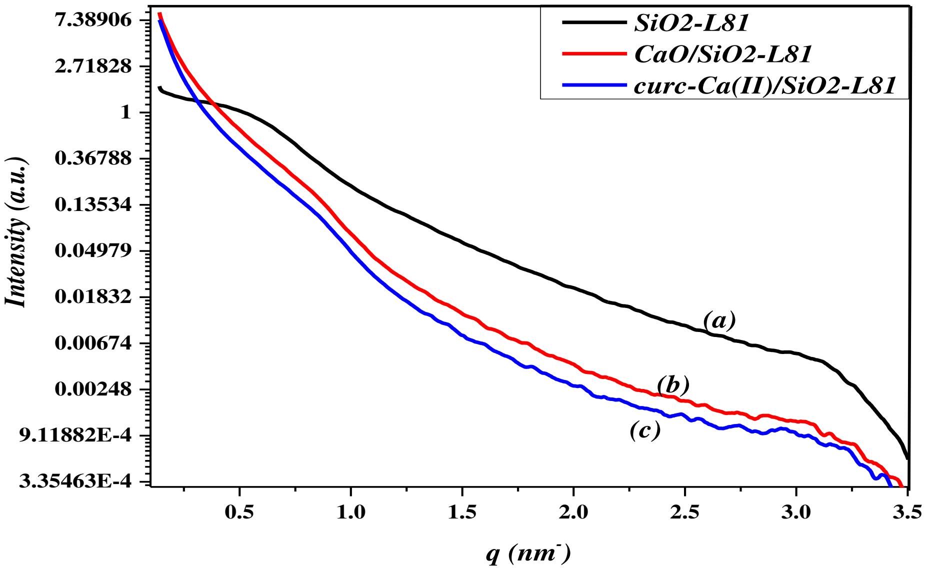

Figure 5.7 SAXS pattern of (a) SiO_2-L81, (b) CaO/SiO_2-L81 and (c) curc–Ca(II)/SiO_2-L81.

5.6 Thermal gravimetric analysis (TGA)

Thermal gravimetric analysis (TGA) used to determine chemical changes, which result as changes in mass when material is heated. Thermal gravimetric analysis (TGA) and differential thermal analysis (DTA) are examined for curc-M(II)/SiO_2-L81 and curc-M(II)/SiO_2-P123 (SBA-15) (Fig.5.8, Fig.5.11, Fig.5.12, Fig.5.13) under nitrogen at 25-600 °C at rate 10 °C/min. Curcumin was stable up to 150 °C and the DTA peak observed at 75 °C due to loss of physically adsorbed water.

TGA – DTA pattern of curc-Ca(II)/SiO_2-L81 and curc-Ca(II)/SiO_2-P123 (SBA-15) (Fig.5.8) show three loss weight steps. For curc-Ca(II)/SiO_2-L81, the first step at 65 °C due to 4.5 % weight loss that corresponds to loss of adsorbed water. The second step at 175 – 430 °C due to 4.5 % weight loss that attributed to decomposition of curcumin. The third step above 430 °C due to 1.5 %, which is due to decomposition of $CaCO_3$ (Gangwar *et al.*, 2013; Mohanan, 2014; Zaki *et al.*, 2006). The total loss is about 10.5 % of initial weight.

For curc-Ca(II)/SiO_2-P123 (SBA-15), the first step at 65 °C due to 6.5 % weight loss that corresponds to loss of adsorbed water. The second step at 200 – 430 °C due to 6 % weight loss that attributed to decomposition of curcumin. The third step above 430 °C due to 0.5 %, which is due to decomposition of $CaCO_3$ (Gangwar *et al.*, 2013; Mohanan, 2014; Zaki *et al.*, 2006). The total loss is about 13 % of initial weight.

CaO, CaO/SiO_2-L81 and curc-Ca(II)/SiO_2-L81 thermograms (Figs.5.9 (a-c)) show 7.2 %, 4 % and 1.5 % weight loss at 430 °C, respectively. This loss is attributed to decomposition of $CaCO_3$ to CaO and loss of CO_2. It was decreased from 7.2 to 4 % due to encapsulated of CaO with SiO_2-L81 and from 4 to 1.5 % due to complexation of calcium(II) with curcumin, which decrease the available area of CaO and decrease the adsorption amount of CO_2.

CaO, CaO/SiO_2-P123 (SBA-15) and curc-Ca(II)/SiO_2-P123 (SBA-15) thermograms (Figs.5.10 (a-c)) show 7.2 %, 1.2 % and 0.5 % weight loss at 430 °C, respectively. This loss is attributed to decomposition of $CaCO_3$ to CaO and loss of CO_2. It was decreased from 7.2 to 1.2 % due to encapsulated of CaO within SiO_2-P123 (SBA-15) and from 1.2 to 0.5 % due to complexation of calcium(II) with curcumin, which decrease the available area of CaO and decrease the adsorption amount of CO_2. The weight loss is 0.5 % for curc-Ca(II) /SiO_2-P123 (SBA-15), but the weight loss is 1.5 % for curc-Ca(II)/SiO_2-L81. This different is probably related to the percent of calcium(II) with curcumin complexation.

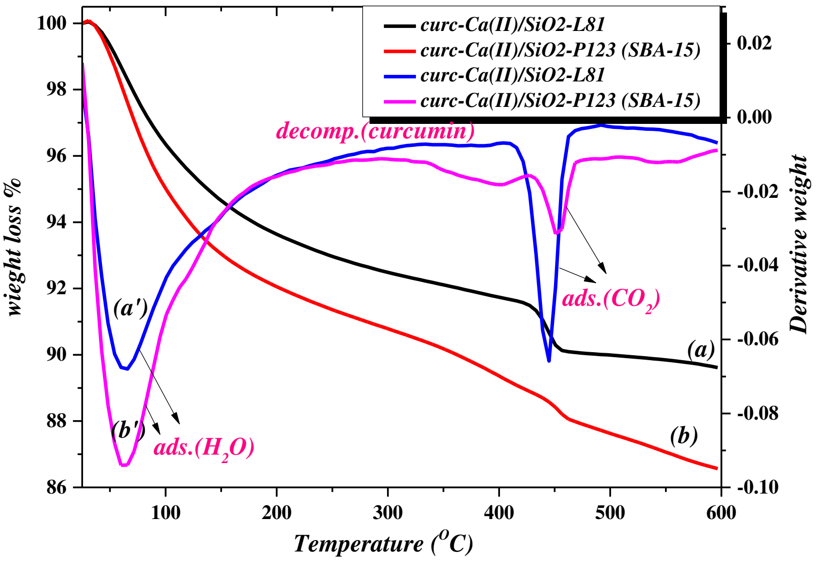

Figure 5.8 TGA – DTA pattern of (a, a') curc-Ca(II)/SiO_2-L81 and (b, b') curc-Ca(II)/SiO_2-P123 (SBA-15).

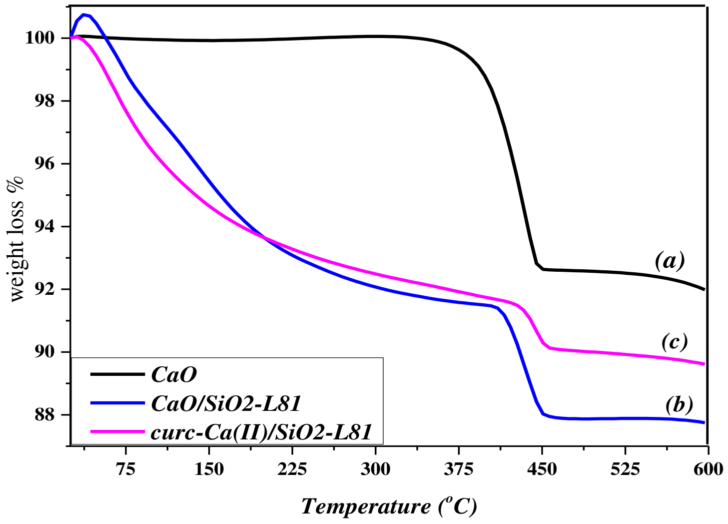

Figure 5.9 TGA pattern of (a) CaO, (b) CaO/SiO$_2$-L81 and (c) curc-Ca(II)/ SiO$_2$-L81.

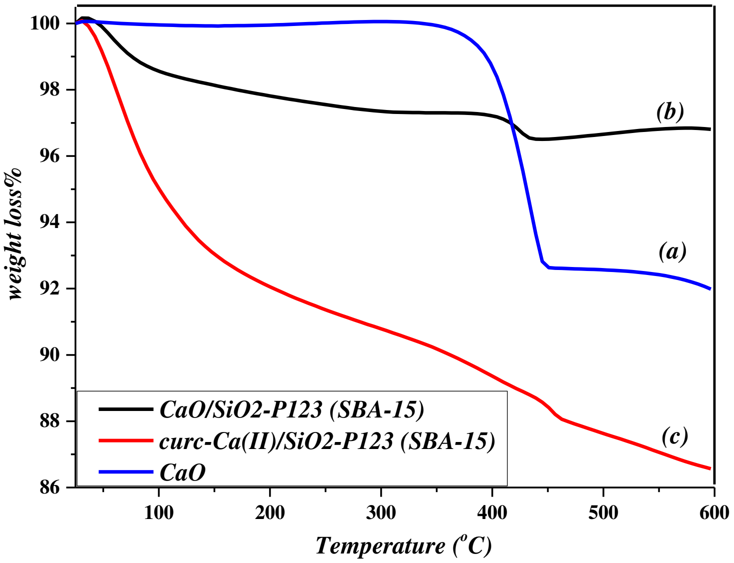

Figure 5.10 TGA pattern of (a) CaO, (b) CaO/SiO$_2$-P123 (SBA-15) and (c) curc-Ca(II)/SiO$_2$-P123 (SBA-15).

Figure 5.11 shows TGA – DTA pattern of curc-Mg(II)/SiO$_2$-L81 and curc-Mg(II)/ SiO$_2$-P123 (SBA-15). TGA-DTA pattern of curc-Mg(II)/SiO$_2$-L81 shows three loss weight steps. The first step (shoulder) and second step at 75 °C and 135 °C are due to 2.5 % and 6.5 % weight loss that are probably due to loss of adsorbed water and elimination of the crystalline water (Mohanan, 2014; Zebib *et al.*, 2010). The third step after 250 °C due to 4.2 %, which is due to chemical decomposition of curcumin without formation of thermally stable intermediates up to 600 °C (Zebib *et al.*, 2010). The total loss is about 13.2 % of initial weight.

TGA-DTA pattern of curc-Mg(II)/SiO_2-P123 (SBA-15) shows two steps of weight loss. The first broad step at 75 °C due to 9 % weight loss that corresponds to loss of adsorbed water and is probably due to elimination of the crystalline water (Mohanan, 2014; Zebib *et al.*, 2010). The second step above 230 °C due to 4.8 %, which is due to curcumin decomposition without formation of thermally stable intermediates up to 600 °C (Zebib *et al.*, 2010). The total loss is about 13.8 % of initial weight.

H

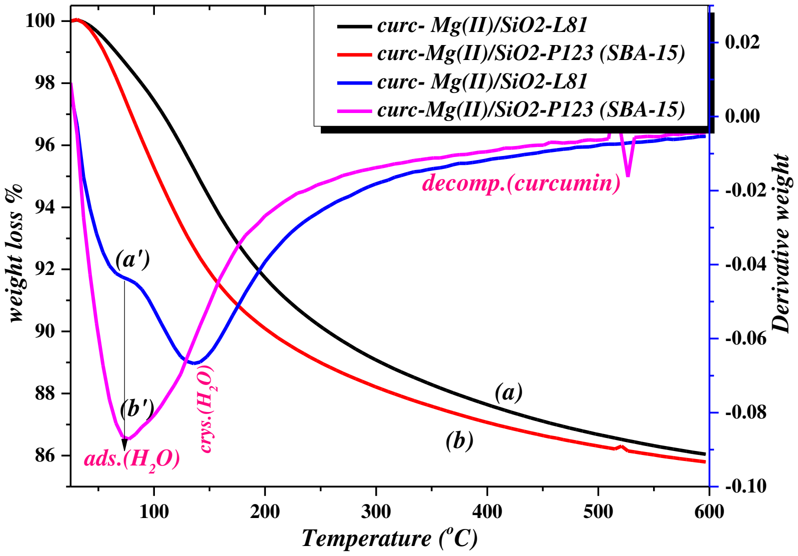

Figure 5.11 TGA–DTA pattern of (a, a') curc-Mg(II)/SiO_2-L81 and (b, b') curc-Mg(II)/SiO_2-P123 (SBA-15).

Figure 5.12 shows TGA-DTA pattern of curc-Cu(II)/SiO_2-L81 and curc-Cu(II)/SiO_2-P123 (SBA-15). TGA – DTA pattern of curc-Cu(II)/SiO_2-L81 shows three loss weight steps. The first step at 65 °C due to 5 % weight loss that corresponds to loss of adsorbed water. The second step at 287 °C due to 1.1 % weight loss that is probably due to condensation of silanols of silica precursors. The third step above 410 °C due to 1.6 %, which is due to curcumin decomposition (Mohanan, 2014; Zebib *et al.*, 2010). The total loss is about 7.7 % of initial weight.

TGA – DTA pattern of curc-Cu(II)/SiO_2-P123 (SBA-15) shows three loss weight steps. The first at about 65 °C due to 6 % weight loss that corresponds to loss of adsorbed water. The second step at 287 °C due to 1.5 % weight loss that is probably due condensation of silanols of silica precursors. The third step above 410 °C due to

2.3 % that is due to curcumin decomposition (Mohanan, 2014; Zebib *et al.*, 2010). The total loss is about 9.8 % of initial weight. A thermally stable decomposition product exists after 550 °C. It may be related with the formation of CuO oxide.

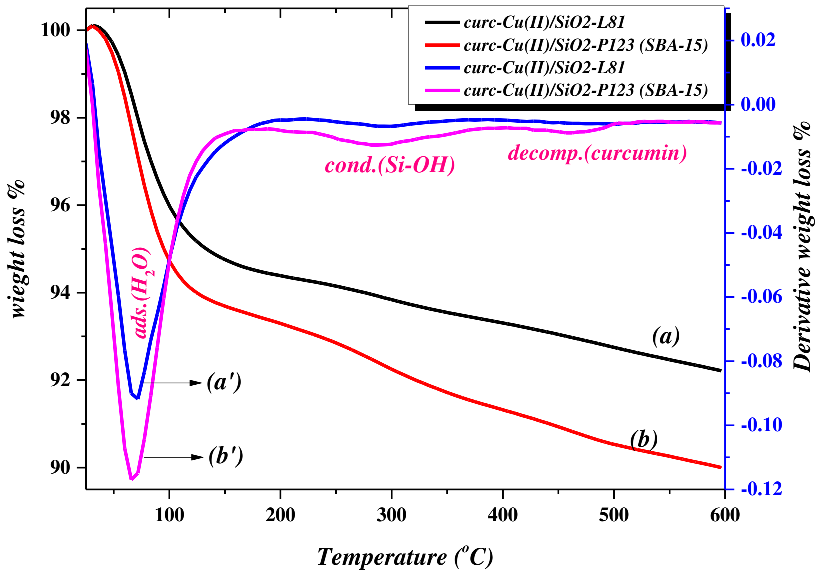

Figure 5.12 TGA–DTA pattern of (a, a') curc-Cu(II)/SiO$_2$ and (b, b') curc-Cu(II)/SiO$_2$-P123 (SBA-15).

Figure 5.13 shows TGA-DTA pattern of curc-Zn(II)/SiO$_2$-L81 and curc-Zn(II)/SiO$_2$-P123 (SBA-15). TGA-DTA pattern of curc-Zn(II)/SiO$_2$-L81 shows three steps of weight loss. The first at 72 °C due to 5 % weight loss that corresponds to loss of adsorbed water. The second step at 250 °C due to 2.6 %, which probably due to condensation of silanols of silica precursors. The third step at 400 °C due to 1.9 %, which is due to curcumin decomposition (Zebib *et al.*, 2010). The total loss is about 9.5 % of initial weight.

TGA-DTA pattern of curc-Zn(II)/SiO$_2$-P123 (SBA-15) shows three steps of weight loss. The first at about 72 °C due to 5.4 % weight loss that corresponds to loss of adsorbed water. The second step at 250 °C due to 2 %, which probably due to condensation of silanols of silica precursors. The third step above 400 °C due to 1.6 %, which is due to curcumin decomposition (Zebib *et al.*, 2010). The total loss is about 9 % of initial weight.

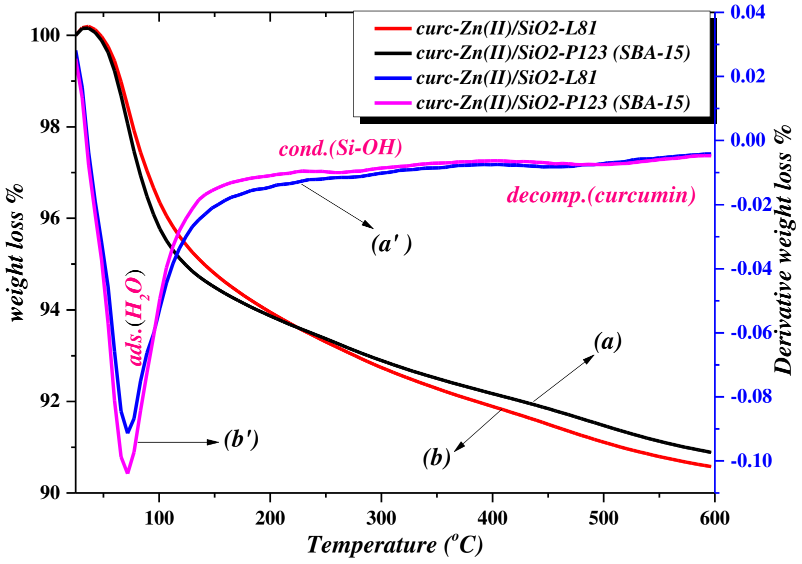

Figure 5.13 TGA–DTA pattern of (a, a') curc-Zn(II)/SiO$_2$-L81 and (b, b') curc-Zn(II)/SiO$_2$-P123 (SBA-15).

5.7 Ultraviolet-Visible spectroscopy (UV-vis)

Figure 5.14 shows UV-vis spectra of curcumin with different concentrations. A UV-visible spectrum of the curcumin in ethanol shows absorption maximum at 429 nm assigned to the band $\pi \rightarrow \pi^*$. As concentration decreases, the absorbance also decreases. The spectra maintained the absorption peak at 429 nm (Patra & Barakat, 2011).

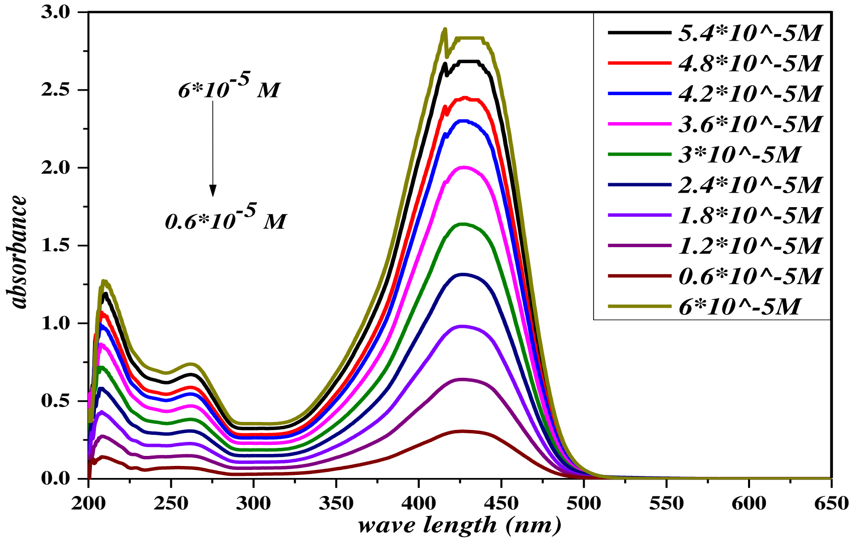

Figure 5.14 UV-vis spectra of different curcumin concentration for standard curve.

Figure 5.15 shows the standard curve of curcumin. The relation between absorbance and concentration is linear.

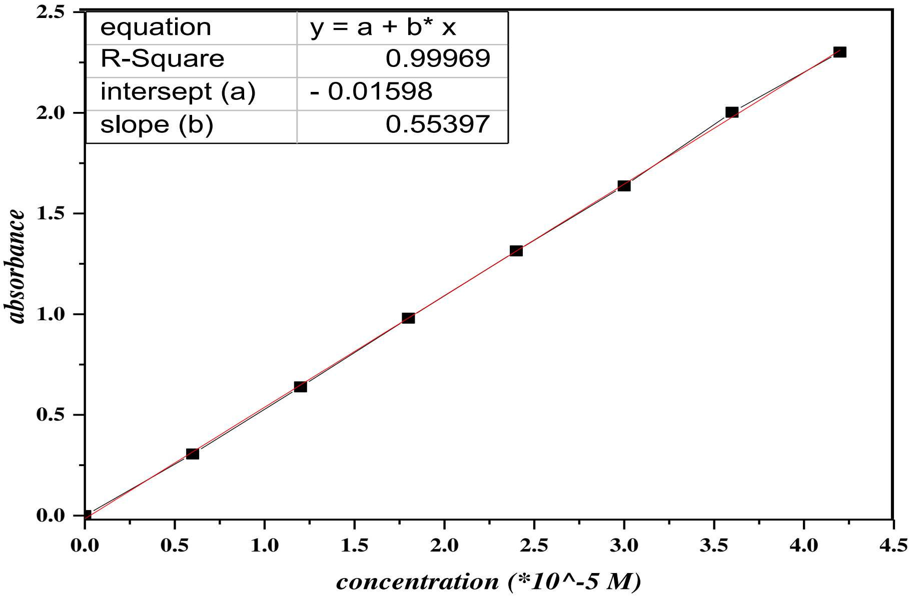

Figure 5.15 Curcumin standard curve.

Figure 5.16 (a & b) shows UV-vis spectra of curcumin solution and curcumin/SiO_2-L81 solution, respectively. UV-vis spectrum of curcumin in ethanol shows absorption maximum at 429 nm assigned to the band $\pi \rightarrow \pi^*$ (Patra & Barakat, 2011). The UV-vis spectra of curcumin/SiO_2-L81 (Fig.5.16b) shows an absorption maximum at 429 nm. It is clear that SiO_2-L81 uptake of curcumin from its ethanolic solution is very small and there is no change in absorption maximum peak.

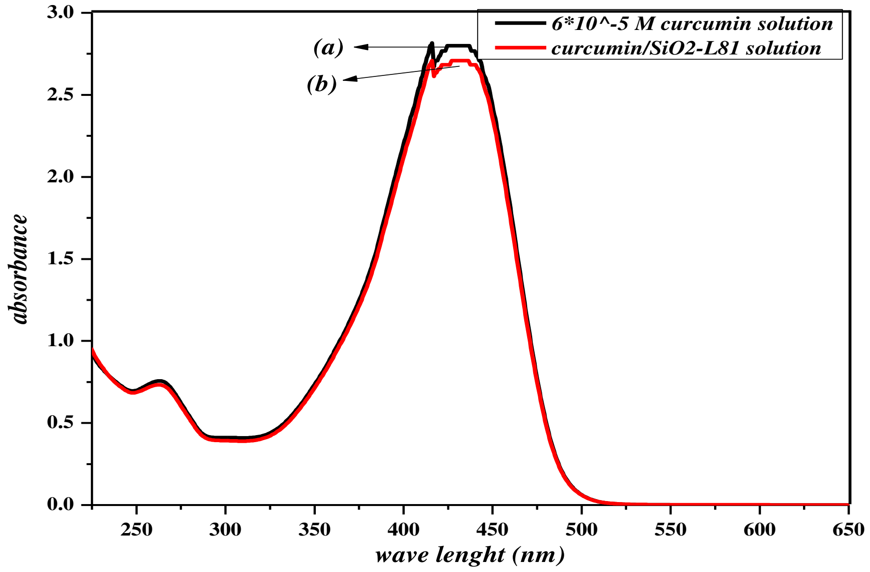

Figure 5.16 UV-vis spectra of (a) curcumin solution and (b) curcumin/SiO_2-L81 solution.

Figure 5.17 (a & b) shows UV-vis spectra of curcumin solution and curc-Ca(II)/SiO_2-L81 solution, respectively. UV-vis spectrum of curcumin in ethanol shows absorption maximum at 429 nm assigned to the band $\pi \rightarrow \pi^*$ (Patra & Barakat, 2011). For the curcumin-Ca(II) complex (Fig.5.17b), the maximum absorption peak of curcumin decreases due to the formation of curcumin – calcium (II) complex (Zebib *et al.*, 2010).

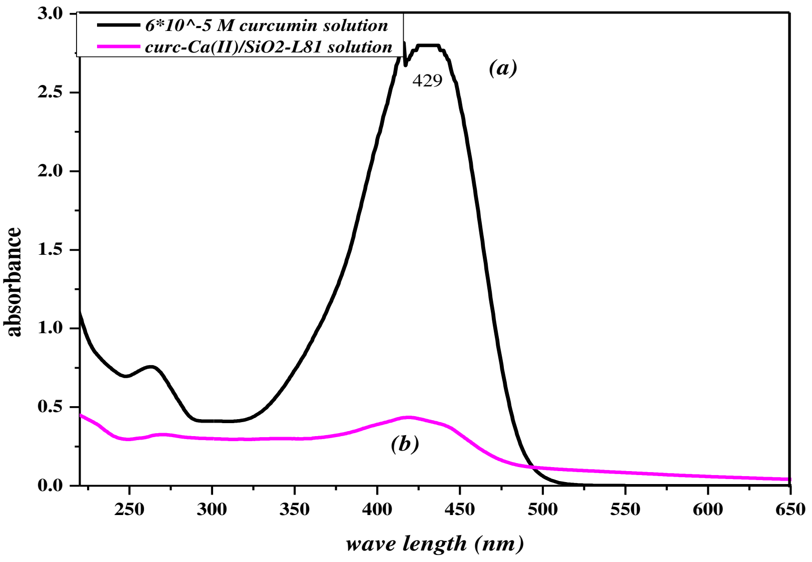

Figure 5.17 UV-vis spectra of (a) curcumin solution and (b) curc-Ca(II)a/SiO_2-L81 solution.

Figure 5.18 (a & b) shows UV-vis spectra of curcumin solution and curc-Mg(II)/SiO_2-L81 solution, respectively. UV-vis spectrum of curcumin in ethanol shows absorption maximum at 429 nm assigned to the band $\pi \rightarrow \pi^*$ (Patra & Barakat, 2011). For the curcumin-Mg(II) complex (Fig.5.18b), the maximum absorption peak of curcumin decreases due to the formation of curcumin – magnesium(II) complex (Zebib *et al.*, 2010).

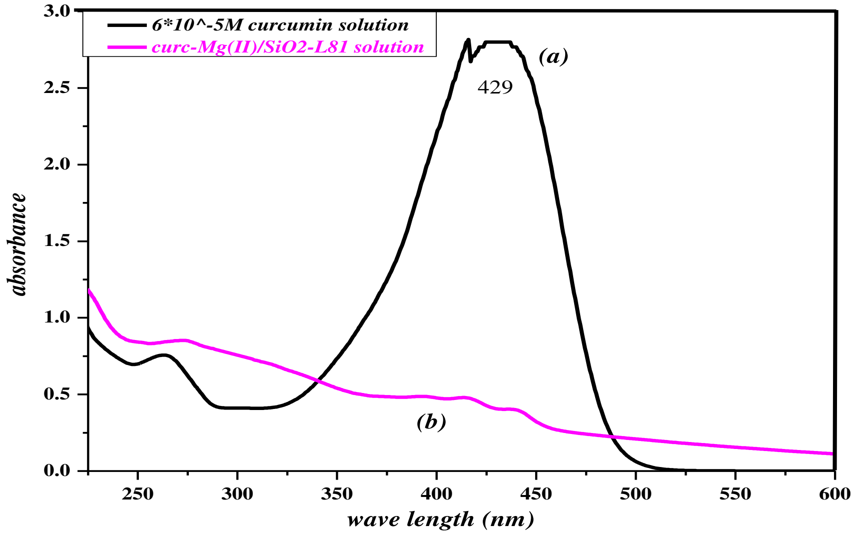

Figure 5.18 UV-vis spectra of (a) curcumin solution and (b) curc-Mg(II)/SiO_2-L81 solution.

Figure 5.19 (a & b) shows UV-vis spectra of curcumin solution and curc-Zn(II)/SiO_2-L81 solution, respectively. UV-vis spectrum of curcumin in ethanol shows absorption maximum at 429 nm assigned to the band $\pi \rightarrow \pi^*$ (Patra & Barakat, 2011). For the curcumin-Zn(II) complexes (Fig.5.19b), The maximum absorption peak of curcumin decrease due to the formation of curcumin – zinc (II) complex (Banerjee, 2014; Zebib *et al.*, 2010).

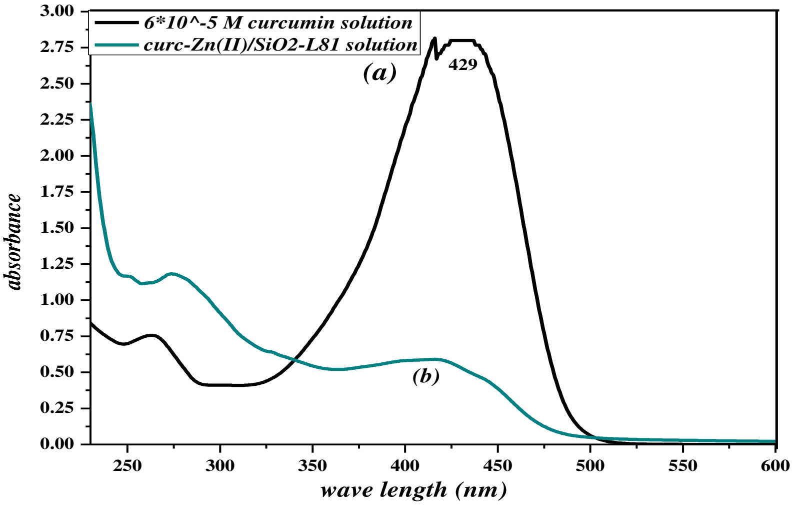

Figure 5.19 UV-vis spectra of (a) curcumin solution and (b) curc-Zn(II)/SiO_2-L81 solution.

Figure 5.20 (a & b) shows UV-vis spectra of curcumin solution and curc-Cu(II)/SiO_2-L81 solution, respectively. UV-vis spectrum of curcumin in ethanol shows absorption maximum at 429 nm assigned to the band $\pi \rightarrow \pi^*$ (Patra & Barakat, 2011). For the curcumin-Cu(II) complex (Fig.5.20), the maximum absorption peak of curcumin decreases due to the formation of curcumin – copper (II) complex (Banerjee, 2014; Zebib *et al.*, 2010).

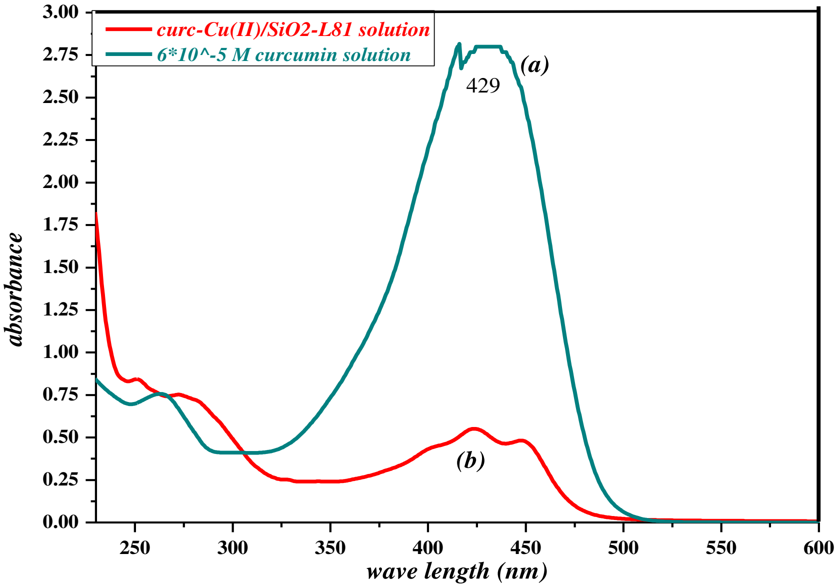

Figure 5.20 UV-vis spectra of (a) curcumin solution and (b) curc-Cu(II)/SiO_2-L81 solution.

Figures (5.21, 5.22, 5.23 & 5.24) showed curcumin uptake % for MO/SiO_2 with different Pluronic surfactant (P-123, L-81, L-61 and L-31). Curcumin uptake % was determined by batch method by mixing each of metal oxide/silica systems with ethanolic curcumin solutions. Measurements were carried out at room temperature after 72 h uptake time to reach equilibrium. As shown in the Figures (5.21, 5.22, 5.23 & 5.24), curcumin uptake % of all metal oxide/silica systems were found in the following order:

SiO_2-P123 (SBA-15) > SiO_2-L81 > SiO_2-L61 > SiO_2-L31.

Figures (5.25, 5.26, 5.27 & 5.28) showed curcumin uptake % for metal oxide encapsulated using all four silica systems (SiO_2-P123 (SBA-15), SiO_2-L81, SiO_2-L61, SiO_2-L31) with different metal oxides (CaO, MgO, CuO and ZnO). Curcumin uptake % was determined by batch method. Measurements were carried out at room temperature after 72 h uptake time to reach equilibrium. As shown in Figures (5.25, 5.26, 5.27 & 5.28), curcumin uptake % of all MO/silica systems were found in the following order:

CaO > MgO > CuO > ZnO.

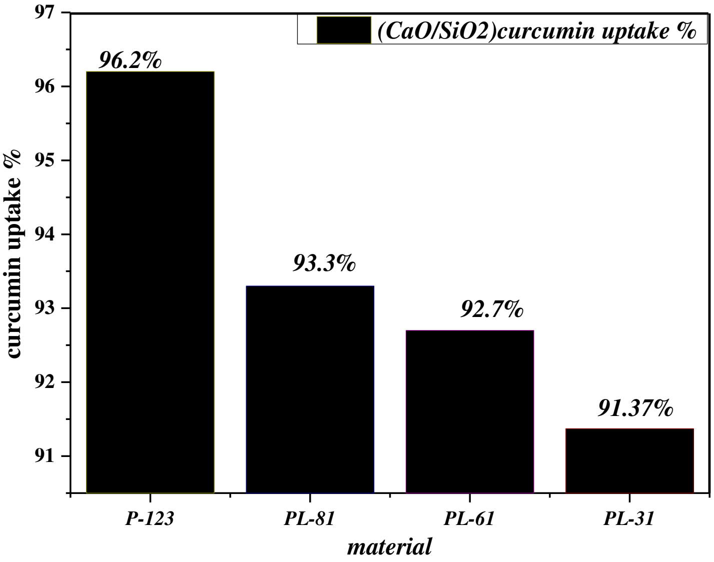

Figure 5.21 Curcumin uptake % for CaO/SiO_2 with different Pluronic surfactant (P-123, L-81, L-61 and L-31).

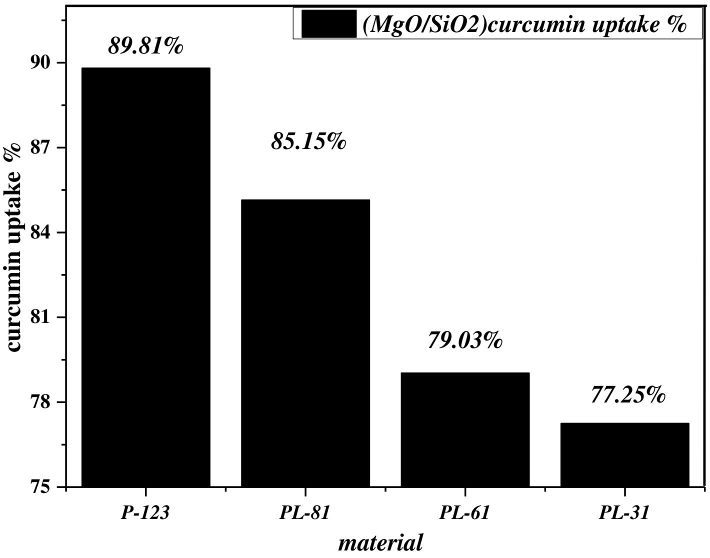

Figure 5.22 Curcumin uptake % for MgO/SiO$_2$ with different Pluronic surfactant (P-123, L-81, L-61 and L-31).

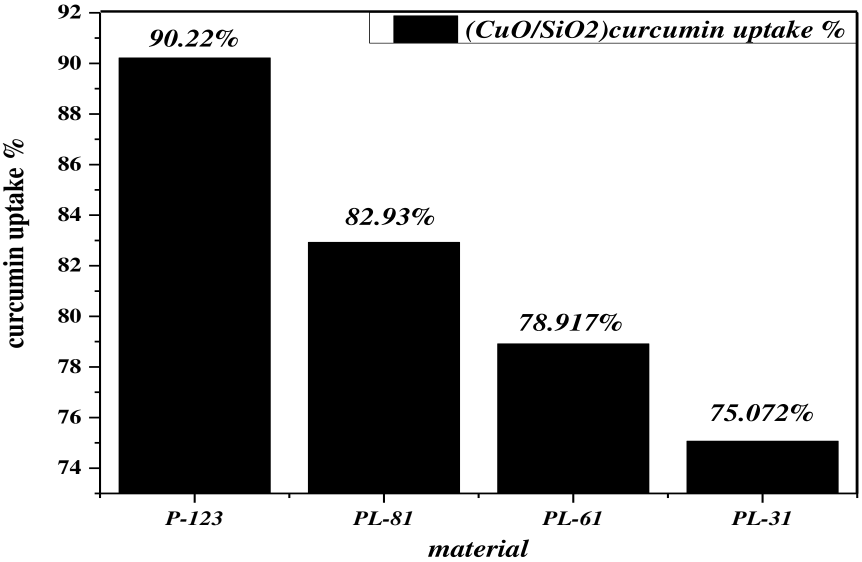

Figure 5.23 Curcumin uptake % for CuO/SiO$_2$ with different Pluronic surfactant (P-123, L-81, L-61 and L-31).

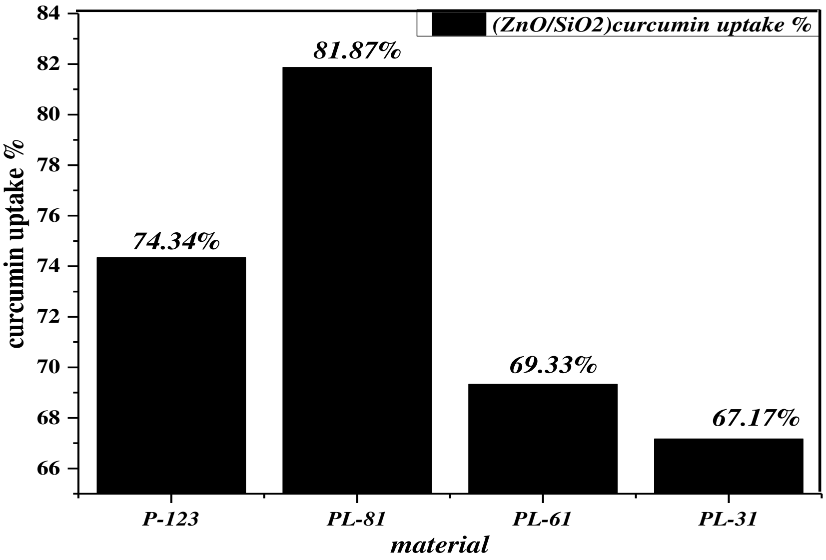

Figure 5.24 Curcumin uptake % for ZnO/SiO_2 with different Pluronic surfactant (P-123, L-81, L-61 and L-31).

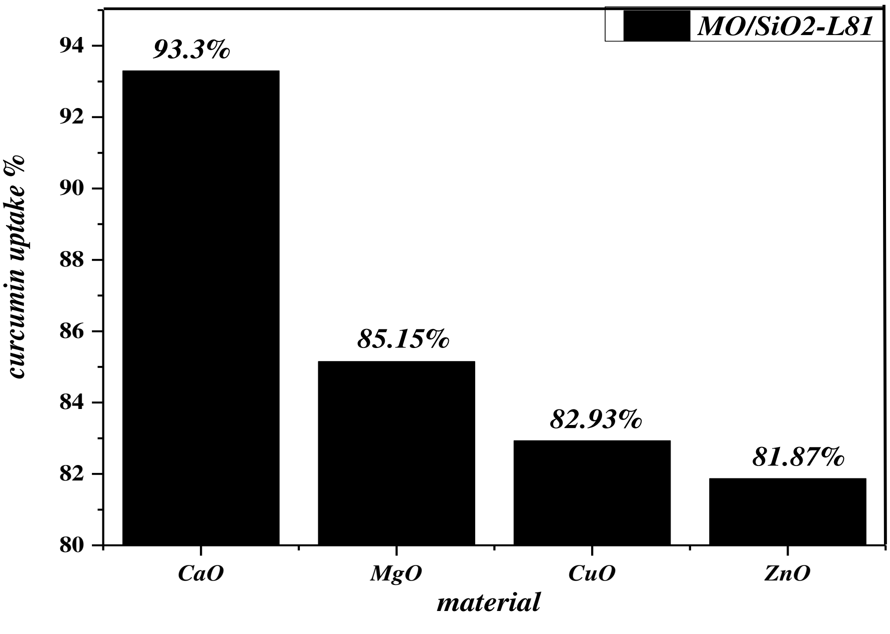

Figure 5.25 Curcumin uptake % for SiO_2-L81 with different metal oxide (CaO, MgO, CuO and ZnO).

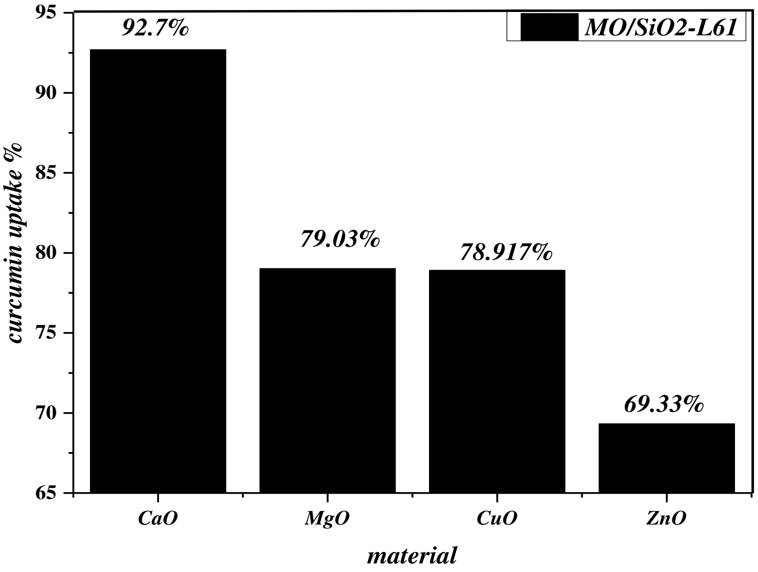

Figure 5.26 Curcumin uptake % for SiO_2-L61 with different metal oxide (CaO, MgO, CuO and ZnO).

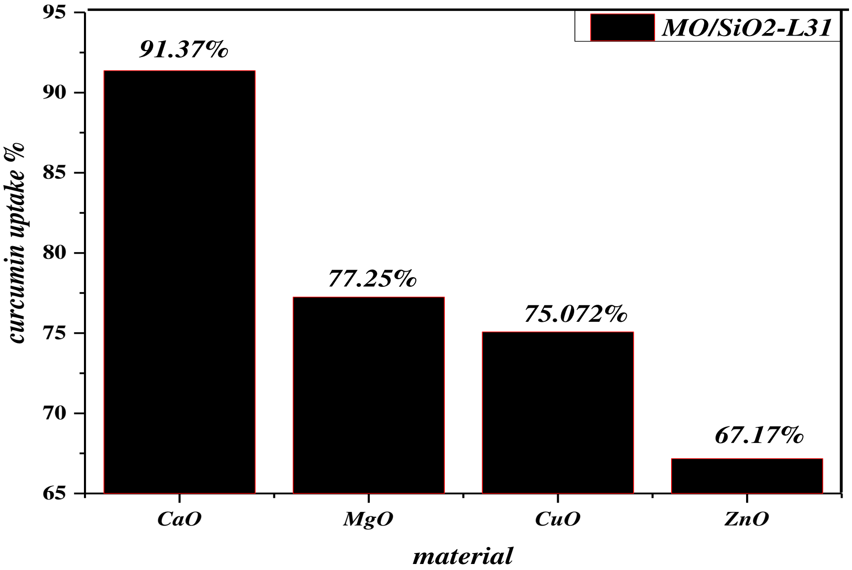

Figure 5.27 Curcumin uptake % for SiO_2-L31 with different metal oxide (CaO, MgO, CuO and ZnO).

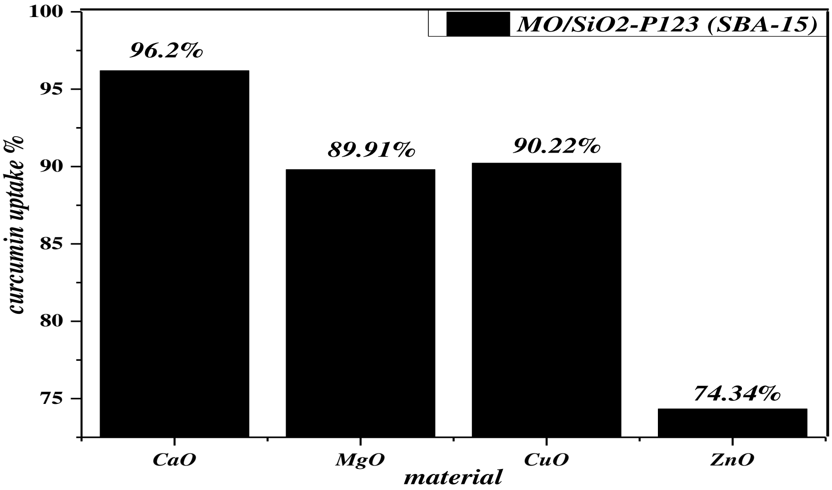

Figure 5.28 Curcumin uptake % for SiO_2-P123 (SBA-15) with different metal oxide (CaO, MgO, CuO and ZnO).

Table 5.1 Metal oxide/silica capacities for curcumin uptake(mg/1 g)

Metal oxide/silica nanocomposites	**Material uptake capacity of curcumin (mg/ 1g)**
CaO/ SiO_2-P123 (SBA-15)	2.657
CaO/SiO_2-L81	2.578
CaO/SiO_2-L61	2.56
CaO/SiO_2-L31	2.524
MgO/ SiO_2-P123 (SBA-15)	2.484
MgO/SiO_2-L81	2.352
MgO/SiO_2-L61	2.183
MgO/SiO_2-L31	2.134
ZnO/ SiO_2-P123 (SBA-15)	2.054
ZnO/SiO_2-L81	2.261
ZnO/SiO_2-L61	1.915
ZnO/SiO_2-L31	1.855
CuO/ SiO_2-P123 (SBA-15)	2.492
CuO/SiO_2-L81	2.291
CuO/SiO_2-L61	2.18
CuO/SiO_2-L31	2.074

5.8 Conclusion

Curcumin–metal(II) complexes encapsulated mesoporous silica were synthesized by treatment of curcumin with metal oxide encapsulated mesoporous silica. The synthesized materials were characterized using fourier transform infrared spectroscopy (FTIR), X-ray diffraction (XRD), small angle X- ray scattering (SAXS), thermal gravimetric analysis (TGA) and ultraviolet-visible spectroscopy (UV-vis).

SAXS results confirmed that the introduction of curcumin into silica precursors do not alter the mesoscopic structure of mesoporous silica. XRD analysis shows that not all the metal oxide reacts with curcumin. This is confirmed by a slight decrease of all diffraction peaks intensity of metal oxide. FTIR analysis also prove that curcumin is chemically bonded with metal oxide. TGA thermogram revealed that the weight loss of curcumin is decreased in the following order 6% > 4.8% > 2.8% > 1.5% for the complexes of Ca(II) > Mg(II) > Cu(II) > Zn(II), respectively. Curcumin uptake % studies show that CaO/SiO_2-P123 (SBA-15) is the best for curcumin uptake, curcumin uptake % was 96.2 %.

Conclusion

Mesoporous silica materials (SBA-15 and lamellar SiO_2) were synthesized using a series of triblock copolymer (Pluronic) nonionic surfactant as template by sol-gel method. Encapsulated metal oxide into mesoporous silica was synthesized using four different metal oxides (CaO, MgO, CuO and ZnO) by impregnation method. The curcumin reacted with encapsulated metal oxide mesoporous silica materials to form curcumin-metal(II) complexes. These materials were investigated by several characterization techniques, such as fourier transform infrared spectroscopy (FTIR), X-ray diffraction (XRD), small angle X- ray scattering (SAXS), transmission electron microscopy (TEM), thermal gravimetric analysis (TGA) and ultraviolet-visible spectroscopy (UV-vis).

For mesoporous silica materials, XRD analysis showed that these materials were in amorphous form. SAXS and TEM confirmed that mesoporous silica synthesized by short EO chain surfactant gives lamellar structure, while that synthesized using medium EO chain surfactant gives 2D hexagonal (P6mm) structure. As the length of PO chain increases, the mesoscopic structure ordering increases.

FTIR spectra of encapsulated metal oxide mesoporous silica confirmed that metal oxides were physically bonded with silanol groups. SAXS and TEM confirmed that the introduction of metal oxides into mesoporous silica do not alter the mesoscopic structure of mesoporous silica. XRD showed that all metal oxides were in crystalline form, faced center cubic CaO, face centered cubic MgO, monoclinic CuO and wurtzite ZnO. TGA thermogram confirmed the high thermal stability of such materials.

For curcumin-metal(II) encapsulated mesoporous silica, SAXS and FTIR confirmed that curcumin was chemically bonded with metal oxides. The curcumin uptake capacity is depended on the nature of metal oxides and the nature of mesoporous silica. it is found that CaO/SBA-15 was the best for curcumin uptake of 96.2%

References

Aguilera-Camacho, L. D., Hernández-Navarro, C., Moreno, K. J., García-Miranda, J. S., & Arizmendi-Morquecho, A. (2015). Improvement effects of CaO nanoparticles on tribological and microhardness properties of PMMA coating. *Journal of Coatings Technology and Research*, 12(2), 347-355.

Ak, T., & Gülçin, İ. (2008). Antioxidant and radical scavenging properties of curcumin. *Chemico-biological interactions*, 174(1), 27-37.

Ambika, S., & Sundrarajan, M. (2015). Antibacterial behaviour of Vitex negundo extract assisted ZnO nanoparticles against pathogenic bacteria. *Journal of Photochemistry and Photobiology B: Biology*, 146, 52-57.

Ambika, S., & Sundrarajan, M. (2015). Green biosynthesis of ZnO nanoparticles using Vitex negundo L. extract: spectroscopic investigation of interaction between ZnO nanoparticles and human serum albumin. *Journal of Photochemistry and Photobiology B: Biology*, 149, 143-148.

Anderson, A. M., Mitchell, M. S., & Mohan, R. S. (2000). Isolation of curcumin from turmeric. *J. Chem. Educ*, 77(3), 359.

Athens, G. L., Shayib, R. M., & Chmelka, B. F. (2009). Functionalization of mesostructured inorganic–organic and porous inorganic materials. *Current Opinion in Colloid & Interface Science*, 14(4), 281-292.

Azam, A., Ahmed, A. S., Oves, M., Khan, M. S., & Memic, A. (2012). Size-dependent antimicrobial properties of CuO nanoparticles against Gram-positive and-negative bacterial strains. *Int. J. Nanomed*, 7, 3527-3535.

Azzaza, S., El-Hilo, M., Narayanan, S., Vijaya, J. J., Mamouni, N., Benyoussef, A. & Bououdina, M. (2014). Structural, optical and magnetic characterizations of Mn-doped MgO nanoparticles. *Materials Chemistry and Physics*, 143(3), 1500-1507.

Bagshaw, S. A., Prouzet, E., & Pinnavaia, T. J. (1995). Templating of mesoporous molecular sieves by nonionic polyethylene oxide surfactants. *Science*, 269(5228), 1242.

Bahawana, Basniwal, R. K., Buttar, H. S., Jain, V. K., & Jain, N. (2011). Curcumin nanoparticles: preparation, characterization, and antimicrobial study. *Journal of agricultural and food chemistry*, 59(5), 2056-2061.

Ballem, M. A., Córdoba, J. M., & Odén, M. (2010). Influence of synthesis temperature on morphology of SBA-16 mesoporous materials with a three-dimensional pore system. *Microporous and Mesoporous Materials*, 129(1), 106-111.

Banerjee, R. (2014). Inhibitory effect of Curcumin-Cu (II) and Curcumin-Zn (II) complexes on amyloid-beta peptide fibrillation. *Bioinorganic chemistry and applications*, 2014.

Barrabino, A. (2011). Synthesis of mesoporous silica particles with control of both pore diameter and particle size.

Barreca, D., Blau, W. J., Croke, G. M., Deeney, F. A., Dillon, F. C., Holmes, J. D., & Tondello, E. (2007). Iron oxide nanoparticle impregnated mesoporous silicas as platforms for the growth of carbon nanotubes. *Microporous and mesoporous Materials*, 103(1), 142-149.

Benamor, T., Michelin, L., Lebeau, B., & Marichal, C. (2012). Flash induction calcination: A powerful tool for total template removal and fine tuning of the hydrophobic/hydrophilic balance in SBA-15 type silica mesoporous materials. *Microporous and Mesoporous Materials*, 147(1), 334-342.

Benamor, T., Vidal, L., Lebeau, B., & Marichal, C. (2012). Influence of synthesis parameters on the physico-chemical characteristics of SBA-15 type ordered mesoporous silica. *Microporous and Mesoporous Materials*, 153, 100-114.

Butt, A. R., Ejaz, S., Baron, J. C., Ikram, M., & ALIa, S. (2015). CaO NANOPARTICLES AS A POTENTIAL DRUG DELIVERY AGENT FOR BIOMEDICAL APPLICATIONS. *Digest Journal of Nanomaterials & Biostructures (DJNB)*, 10(3).

Chandran, P., Netha, S., & Khan, S. S. (2014). Effect of humic acid on photocatalytic activity of ZnO nanoparticles. *Journal of Photochemistry and Photobiology B: Biology*, 138, 155-159.

Chatterjee, A., Das, P. C., Adak, K., Das, S., Ghosh, S., & Ganguly, S. (2014). Curcumin-A Natural Antioxidant for Improving Shelf Life of Wheat Flour. *Chem. Sci. Rev. Lett.*, 3(11), 322-328.

Chen, L., Xu, J., Zhang, W. H., Holmes, J. D., & Morris, M. A. (2011). Syntheses of complex mesoporous silicas using mixtures of nonionic block copolymer surfactants: Understanding formation of different structures using solubility parameters. *Journal of colloid and interface science*, 353(1), 169-180.

Claesson, E. M., & Philipse, A. P. (2007). Thiol-functionalized silica colloids, grains, and membranes for irreversible adsorption of metal (oxide) nanoparticles. *Colloids and Surfaces A: Physicochemical and Engineering Aspects*, 297(1), 46-54.

Dagher, S., Haik, Y., Ayesh, A. I., & Tit, N. (2014). Synthesis and optical properties of colloidal CuO nanoparticles. *Journal of Luminescence*, 151, 149-154.

De Falco, G., Morgan, A., Commodo, M., Minutolo, P., & D'Anna, A. (2013). Flame synthesis of MgO nanoparticles in a FASP reactor. *MRS Online Proceedings Library Archive*, 1506, mrsf12-1506.

Dhal, J. P., Sethi, M., Mishra, B. G., & Hota, G. (2015). MgO nanomaterials with different morphologies and their sorption capacity for removal of toxic dyes. *Materials Letters*, 141, 267-271.

Das, S. (2011). Immobilization of Enzymes in Sol-Gel Mesoporous Silica, Enzymatic Digestion of Biomass, and Silica-Curcumin Hybrid Materials (Doctoral dissertation, Drexel University).

Dong, C., Xiao, X., Chen, G., Guan, H., & Wang, Y. (2015). Morphology control of porous CuO by surfactant using combustion method. *Applied Surface Science*, 349, 844-848.

Dovgolevsky, E., Kirmayer, S., Lakin, E., Yang, Y., Brinker, C. J., & Frey, G. L. (2008). Self-assembled conjugated polymer–surfactant–silica mesostructures and their integration into light-emitting diodes. *Journal of Materials Chemistry*, 18(4), 423-436.

El-Nahhal, I. M., Salem, J. K., Kuhn, S., Hammad, T., Hempelmann, R., & Al Bhaisi, S. (2016). Synthesis & characterization of silica coated and functionalized silica coated zinc oxide nanomaterials. *Powder Technology*, 287, 439-446.

El-Nahhal, I. M., Salem, J. K., Kuhn, S., Hammad, T., Hempelmann, R., & Al Bhaisi, S. (2016). Synthesis and characterization of silica-, meso-silica-and their functionalized silica-coated copper oxide nanomaterials. *Journal of Sol-Gel Science and Technology*, 79(3), 573-583.

El-Nahhal, I. M., Salem, J. K., Selmane, M., Kodeh, F. S., & Ebtihan, H. A. (2017). Synthesis and structural characterization of ZnO and CuO nanoparticles supported mesoporous silica SBA-15. *Chemical Physics Letters*, 667, 165-171.

El-Trass, A., ElShamy, H., El-Mehasseb, I., & El-Kemary, M. (2012). CuO nanoparticles: synthesis, characterization, optical properties and interaction with amino acids. *Applied Surface Science*, 258(7), 2997-3001.

Fernández-García, M., & Rodriguez, J. A. (2011). Metal oxide nanoparticles. *Encyclopedia of Inorganic and Bioinorganic Chemistry*.

Flodström, K., & Alfredsson, V. (2003). Influence of the block length of triblock copolymers on the formation of mesoporous silica. *Microporous and mesoporous Materials*, 59(2), 167-176.

Furtado, A. M., Wang, Y., Glover, T. G., & LeVan, M. D. (2011). MCM-41 impregnated with active metal sites: synthesis, characterization, and ammonia adsorption. *Microporous and Mesoporous Materials*, 142(2), 730-739.

Gangwar, R. K., Tomar, G. B., Dhumale, V. A., Zinjarde, S., Sharma, R. B., & Datar, S. (2013). Curcumin conjugated silica nanoparticles for improving bioavailability and its anticancer applications. *Journal of agricultural and food chemistry*, 61(40), 9632-9637.

García-Martínez, J., Brugarolas, P., & Domínguez-Domínguez, S. (2007). Ordered circular mesoporosity induced by phospholipids. *Microporous and mesoporous materials*, 100(1), 63-69.

Ge, Y. S., Jin, C., Song, Z., Zhang, J. Q., Jiang, F. L., & Liu, Y. (2014). Multi-spectroscopic analysis and molecular modeling on the interaction of curcumin and its derivatives with human serum albumin: a comparative study. *Spectrochimica Acta Part A: Molecular and Biomolecular Spectroscopy*, 124, 265-276.

Ghiasi, M., & Malekzadeh, A. (2012). Synthesis of CaCO3 nanoparticles via citrate method and sequential preparation of CaO and Ca (OH) 2 nanoparticles. *Crystal Research and Technology*, 47(4), 471-478.

Ghosh, S., & Mondal, S. (2012). Spectroscopic study on the interaction of medicinal pigment, curcumin with various surfactants: An overview. *J. Surf. Sci. Technol*, 28, 179-195.

Gupta, N. K., Nahata, A., & Dixit, V. K. (2010). Development of a spectrofluorimetric method for the determination of curcumin. *Asian J Trad Med*, 5(1), 12-18.

Hadia, N. M. A., & Mohamed, H. A. H. (2015). Characteristics and optical properties of MgO nanowires synthesized by solvothermal method. *Materials Science in Semiconductor Processing*, 29, 238-244.

Higgins, S., Kennard, R., Hill, N., DiCarlo, J., & DeSisto, W. J. (2006). Preparation and characterization of non-ionic block co-polymer templated mesoporous silica membranes. *Journal of membrane science*, 279(1), 669-674.

Himesh, S., Sharan, P. S., Mishra, K., Govind, N., & Singhai, A. K. (2011). Qualitative and quantitative profile of curcumin from ethanolic extract of Curcuma longa. *Int Res J Pharm*, 2, 180-184.

Hoffmann, F., Cornelius, M., Morell, J., & Fröba, M. (2006). Silica-based mesoporous organic–inorganic hybrid materials. *Angewandte Chemie International Edition*, 45(20), 3216-3251.

Hu, K., Huang, X., Gao, Y., Huang, X., Xiao, H., & McClements, D. J. (2015). Core–shell biopolymer nanoparticle delivery systems: Synthesis and characterization of curcumin fortified zein–pectin nanoparticles. *Food chemistry*, 182, 275-281.

Huang, W. C., Lai, N. C., Chang, L. L., & Yang, C. M. (2012). Mercaptopropyl-functionalized helical mesoporous silica nanoparticles with c2mm symmetry:

Cocondensation synthesis and structural transformation in the dilute solution of mixed cationic and nonionic surfactants. *Microporous and Mesoporous Materials*, 151, 411-417.

Huang, C. H., Chang, K. P., Yu, C. T., Chiang, P. C., & Wang, C. F. (2010). Development of high-temperature CO_2 sorbents made of CaO-based mesoporous silica. *Chemical Engineering Journal*, 161(1), 129-135.

Hussein, J., Razik, T. E. A., & El-Banna, M. (2015). Pre- administration of curcumin prevents hyperhomocysteinemia in ethanol-induced gastric ulcer.

Imtiaz, A., Akhyar Farrukh, M., Khaleeq-ur-rahman, M., Adnan, R. (2013). Micelle-Assisted Synthesis of Al2O3·CaO Nanocatalyst: Optical Properties and Their Applications in Photodegradation of 2,4,6-Trinitrophenol. *The Scientific World Journal*.

İpeksaç, T., Kaya, F., & Kaya, C. (2013). Hydrothermal synthesis of Zinc oxide (ZnO) nanotubes and its electrophoretic deposition on nickel filter. *Materials Letters*, 100, 11-14.

Kabanov, A. V., Batrakova, E. V., & Alakhov, V. Y. (2002). Pluronic® block copolymers as novel polymer therapeutics for drug and gene delivery. *Journal of controlled release*, 82(2), 189-212.

Kairyte, K., Kadys, A., & Luksiene, Z. (2013). Antibacterial and antifungal activity of photoactivated ZnO nanoparticles in suspension. *Journal of Photochemistry and Photobiology B: Biology*, 128, 78-84.

Kanhathaisong, S., Rattanaphani, S., Rattanaphani, V., & Manyum, T. (2011). A spectroscopic investigation of the complex of turmeric dye with copper (II) in aqueous solution. *Suranaree J. Sci. Technol*, 18(2), 159-165.

Khalil, M. I., Al-Qunaibit, M. M., Al-Zahem, A. M., & Labis, J. P. (2014). Synthesis and characterization of ZnO nanoparticles by thermal decomposition of a curcumin zinc complex. *Arabian Journal of Chemistry*, 7(6), 1178-1184.

Kipkemboi, P., Fogden, A., Alfredsson, V., & Flodström, K. (2001). Triblock copolymers as templates in mesoporous silica formation: Structural dependence on polymer chain length and synthesis temperature. *Langmuir*, 17(17), 5398-5402.

Krupka, T. M., & Exner, A. A. (2011). Structural parameters governing activity of Pluronic triblock copolymers in hyperthermia cancer therapy. *International Journal of Hyperthermia*, 27(7), 663-671.

Kshirsagar, J. M., Shrivastava, R., & Adwani, P. S. (2015). Preparation and characterization of copper oxide nanoparticles and determination of enhancement in critical heat flux. *Thermal Science*, (00), 26-26.

Kulkarni, S. J., Maske, K. N., Budre, M. P., & Mahajan, R. P. (2012). Extraction and purification of curcuminoids from Turmeric (Curcuma longa L.). *Int. J. Pharmacol. Pharm. Tech*, 1, 2277-3436.

Kumar, A., Thota, S., Varma, S., & Kumar, J. (2011). Sol–gel synthesis of highly luminescent magnesium oxide nanocrystallites. *Journal of Luminescence*, 131(4), 640-648.

Kundu, D., Hazra, C., Chatterjee, A., Chaudhari, A., & Mishra, S. (2014). Extracellular biosynthesis of zinc oxide nanoparticles using Rhodococcus pyridinivorans NT2: Multifunctional textile finishing, biosafety evaluation and in vitro drug delivery in colon carcinoma. *Journal of Photochemistry and Photobiology B: Biology*, 140, 194-204.

Lam, K. F., Yeung, K. L., & McKay, G. (2005). Gold Removal and Recovery using Mesoporous Silica Adsorbents. *In 2005 NSTI Nanotechnology Conference and Trade Show-NSTI Nanotech 2005 Technical Proceedings* (p. 273).

Lee, H. S., Kim, W. H., Lee, J. H., Choi, D. J., Jeong, Y. K., & Chang, J. H. (2012). Transition metal-chelating surfactant micelle templates for facile synthesis of mesoporous silica nanoparticles. *Journal of Solid State Chemistry*, 185, 89-94.

Lee, J., & Chang, J. H. (2012). Highly ordered magnetic mesoporous silicas for effective elimination of carbon monoxide. *Journal of Solid State Chemistry*, 188, 100-104.

Lu, Q., Wang, Z., Li, J., Wang, P., & Ye, X. (2009). Structure and photoluminescent properties of ZnO encapsulated in mesoporous silica SBA-15 fabricated by two-solvent strategy. *Nanoscale research letters*, 4(7), 646.

Mageshwari, K., Mali, S. S., Sathyamoorthy, R., & Patil, P. S. (2013). Template-free synthesis of MgO nanoparticles for effective photocatalytic applications. *Powder technology*, 249, 456-462.

Maoz, B. M., Tirosh, E., Sadan, M. B., & Markovich, G. (2011). Defect-induced magnetism in chemically synthesized nanoscale sheets of MgO. *Physical Review B*, 83(16), 161201

Meenakshi, S. D., Rajarajan, M., Rajendran, S., Kennedy, Z. R., & Brindha, G. (2012). Synthesis and characterization of magnesium oxide nanoparticles. *Elixir Int J*, 50(9), 1-3.

Mesa, M., Sierra, L., & Guth, J. L. (2008). Contribution to the study of the formation mechanism of mesoporous SBA-15 and SBA-16 type silica particles in aqueous acid solutions. *Microporous and mesoporous materials*, 112(1), 338-350.

Miguel, G., Juan, H., Leticia, B., Joaquin, N., & Mario, E. R. G. (2009). Characterization of calcium carbonate, calcium oxide and calcium hydroxide as starting point to the improvement of lime for their use in construction. *J Mater Civ Eng*, 21, 625-708.

Mirghiasi, Z., Bakhtiari, F., Darezereshki, E., & Esmaeilzadeh, E. (2014). Preparation and characterization of CaO nanoparticles from Ca (OH) 2 by direct thermal decomposition method. *Journal of Industrial and Engineering Chemistry*, 20(1), 113-117.

Modasiya, M. K., & Patel, V. M. (2012). Studies on solubility of curcumin. *International Journal of Pharmacy & Life Sciences*, 3(3).

Mohan, P. K., Sreelakshmi, G., Muraleedharan, C. V., & Joseph, R. (2012). Water soluble complexes of curcumin with cyclodextrins: Characterization by FT-Raman spectroscopy. *Vibrational Spectroscopy*, 62, 77-84.

Mohanan, P. V. (2014). Curcumin and its derivatives as Antioxidants and DNA Intercalators.

Mohandes, F., Davar, F., & Salavati-Niasari, M. (2010). Magnesium oxide nanocrystals via thermal decomposition of magnesium oxalate. *Journal of Physics and Chemistry of Solids*, 71(12), 1623-1628.

Mustafa, G., Tahir, H., Sultan, M., & Akhtar, N. (2013). Synthesis and characterization of cupric oxide (CuO) nanoparticles and their application for the removal of dyes. *African Journal of Biotechnology*, 12(47), 6650-6660.

Nagajyothi, P. C., Cha, S. J., Yang, I. J., Sreekanth, T. V. M., Kim, K. J., & Shin, H. M. (2015). Antioxidant and anti-inflammatory activities of zinc oxide nanoparticles synthesized using Polygala tenuifolia root extract. *Journal of Photochemistry and Photobiology B: Biology*, 146, 10-17.

Naik, S. P., Yamakita, S., Ogura, M., & Okubo, T. (2004). Studies on mesoporous silica films synthesized using F127, a triblock co-polymer. *Microporous and mesoporous materials*, 75(1), 51-59.

Ngamcharussrivichai, C., Meechan, W., Ketcong, A., Kangwansaichon, K., Butnark, S. (2011). Preparation of heterogeneous catalysts from limestone for transesterification of vegetable oils—Effects of binder addition. *Journal of Industrial and Engineering Chemistry*, 17, 587–595.

Nikolić, M., Giannakopoulos, K. P., & Srdić, V. V. (2010). Synthesis and characterization of mesoporous silica core-shell particles. *Processing Appl. Ceramics*, 4(2), 81-85.

Pang, S. C., Tay, S. H., & Chin, S. F. (2014). Facile synthesis of curcumin-loaded starch-maleate nanoparticles. *Journal of Nanomaterials*, 2014, 22.

Panigoro, R., & Diah Dhianawaty, D. (2013). Curcumin concentration in fresh and decoction of dried Curcuma longa L.(Turmeric) rhizome as homemade jamu. Abstrak.

Pathakoti, K., Huang, M. J., Watts, J. D., He, X., & Hwang, H. M. (2014). Using experimental data of Escherichia coli to develop a QSAR model for predicting the photo-induced cytotoxicity of metal oxide nanoparticles. *Journal of Photochemistry and Photobiology B: Biology*, 130, 234-240.

Patra, D., & Barakat, C. (2011). Synchronous fluorescence spectroscopic study of solvatochromic curcumin dye. *Spectrochimica Acta Part A: Molecular and Biomolecular Spectroscopy*, 79(5), 1034-1041.

Patra, D., & Barakat, C. (2011). Unique role of ionic liquid [bmin][BF 4] during curcumin–surfactant association and micellization of cationic, anionic and non-ionic surfactant solutions. *Spectrochimica Acta Part A: Molecular and Biomolecular Spectroscopy*, 79(5), 1823-1828.

Phiwdang, K., Suphankij, S., Mekprasart, W., & Pecharapa, W. (2013). Synthesis of CuO nanoparticles by precipitation method using different precursors. *Energy Procedia*, 34, 740-745.

Popuri, A. K., & Pagala, B. (2013). Extraction of curcumin from turmeric roots. *Int J Innov Res Studies*, 2(5), 289-299.

Rahman, I. A., & Padavettan, V. (2012). Synthesis of silica nanoparticles by sol-gel: size-dependent properties, surface modification, and applications in silica-polymer nanocomposites—a review. *Journal of Nanomaterials*, 2012, 8.

Ramanujam, K., & Sundrarajan, M. (2014). Antibacterial effects of biosynthesized MgO nanoparticles using ethanolic fruit extract of Emblica officinalis. *Journal of Photochemistry and Photobiology B: Biology*, 141, 296-300.

Refaat, A. A. (2011). Biodiesel production using solid metal oxide catalysts. *International Journal of Environmental Science & Technology*, 8(1), 203-221.

Roggenbuck, J., Waitz, T., & Tiemann, M. (2008). Synthesis of mesoporous metal oxides by structure replication: Strategies of impregnating porous matrices with metal salts. *Microporous and Mesoporous Materials*, 113(1), 575-582.

Safaei-Ghomi, J., Ghasemzadeh, M. A., & Mehrabi, M. (2013). Calcium oxide nanoparticles catalyzed one-step multicomponent synthesis of highly substituted pyridines in aqueous ethanol media. *Scientia Iranica*, 20(3), 549-554.

Saithongdee, A., Praphairaksit, N., & Imyim, A. (2014). Electrospun curcumin-loaded zein membrane for iron (III) ions sensing. *Sensors and Actuators B: Chemical*, 202, 935-940.

Salem, J. K., El-Nahhal, I. M., Hammad, T. M., Kuhn, S., Sharekh, S. A., El-Askalani, M., & Hempelmann, R. (2015). Optical and fluorescence properties of MgO nanoparticles in micellar solution of hydroxyethyl laurdimonium chloride. *Chemical Physics Letters*, 636, 26-30.

Sayin, M. (2010). Synthesis of mesoporous silica particles using SDS-Pluronic couples *(Doctoral dissertation, Bilkent University*).

Showkat, A. M., Zhang, Y. P., Kim, M. S., Gopalan, A. I., Reddy, K. R., & Lee, K. (2007). Analysis of heavy metal toxic ions by adsorption onto amino-functionalized ordered mesoporous silica. *BULLETIN-KOREAN CHEMICAL SOCIETY*, 28(11), 1985.

Sierra, L., Valange, S., & Guth, J. L. (2009). Formation mechanism and morphology of mesoporous SBA-16 type silica particles prepared with the triblock copolymer surfactant PEO 140 PPO 39 PEO 140. *Microporous and Mesoporous Materials*, 124(1), 100-109.

Singh, G., Babele, P. K., Kumar, A., Srivastava, A., Sinha, R. P., & Tyagi, M. B. (2014). Synthesis of ZnO nanoparticles using the cell extract of the cyanobacterium, Anabaena strain L31 and its conjugation with UV-B absorbing compound shinorine. *Journal of Photochemistry and Photobiology B: Biology*, 138, 55-62.

Smijs, T. G., & Pavel, S. (2011). Titanium dioxide and zinc oxide nanoparticles in sunscreens: focus on their safety and effectiveness. *Nanotechnol Sci Appl*, 4(4), 95-112.

Son, D. I., You, C. H., & Kim, T. W. (2009). Structural, optical, and electronic properties of colloidal CuO nanoparticles formed by using a colloid-thermal synthesis process. *Applied surface science*, 255(21), 8794-8797.

Stankovic, I. (2004). Curcumin Chemical and Technical Assessment (CTA), *61 st JECFA*.

Stutzman, P. E. (1996). Guide for X-ray powder diffraction analysis of Portland cement and clinker. *US Department of Commerce, Technology Administration, National Institute of Standards and Technology, Office of Applied Economics, Building and Fire Research Laboratory*.

Subhan, M. A., Alam, K., Rahaman, M. S., Rahman, M. A., & Awal, R. (2013). Synthesis and Characterization of Metal Complexes Containing Curcumin (C 21 H 20 O 6) and Study of their Anti-microbial Activities and DNA-binding Properties. *Journal of Scientific Research*, 6(1), 97-109.

Suleiman, M., Mousa, M., Hussein, A., Hammouti, B., Hadda, T. B., & Warad, I. (2013). Copper (II)-oxide nanostructures: synthesis, characterizations and their applications-review. *Journal of Materials and Environmental Science*, 4(5), 792-797.

Sun, H., Han, J., Ding, Y., Li, W., Daun, J., Chen, P., Lou, H., Zheng, X. (2010). One-pot synthesized mesoporous Ca/SBA-15 solid base for transeeterification of sunflower oil with methanol. *Applied Catalysis A: General*, 390, 26–34.

Tada-Oikawa, S., Ichihara, G., Suzuki, Y., Izuoka, K., Wu, W., Yamada, Y., ... & Ichihara, S. (2015). Zn (II) released from zinc oxide nano/micro particles suppresses vasculogenesis in human endothelial colony-forming cells. *Toxicology Reports*, 2, 692-701.

Talebian, N., Amininezhad, S. M., & Doudi, M. (2013). Controllable synthesis of ZnO nanoparticles and their morphology-dependent antibacterial and optical properties. *Journal of Photochemistry and Photobiology B: Biology*, 120, 66-73.

Tang, Z. X., Claveau, D., Corcuff, R., Belkacemi, K., & Arul, J. (2008). Preparation of nano-CaO using thermal-decomposition method. *Materials letters*, 62(14), 2096-2098.

Thejeswari, Y., Kumar, S. R., Duganath, N., & Devanna, N. (2013). *INTERNATIONAL JOURNAL OF UNIVERSAL PHARMACY AND BIO SCIENCES.*

Thielemann, J. P., Girgsdies, F., Schlögl, R., & Hess, C. (2011). Pore structure and surface area of silica SBA-15: influence of washing and scale-up. *Beilstein journal of nanotechnology*, 2(1), 110-118.

Verma, R., Naik, K. K., Gangwar, J., & Srivastava, A. K. (2014). Morphology, mechanism and optical properties of nanometer-sized MgO synthesized via facile wet chemical method. *Materials Chemistry and Physics*, 148(3), 1064-1070.

Waldron, K., Wu, W. D., Wu, Z., Liu, W., Selomulya, C., Zhao, D., & Chen, X. D. (2014). Formation of monodisperse mesoporous silica microparticles via spray-drying. *Journal of colloid and interface science*, 418, 225-233.

Wang, H., Xu, J. Z., Zhu, J. J., & Chen, H. Y. (2002). Preparation of CuO nanoparticles by microwave irradiation. *Journal of Crystal Growth*, 244(1), 88-94.

Wang, N., Yu, X., Shen, K., Chu, W., & Qian, W. (2013). Synthesis, characterization and catalytic performance of MgO-coated Ni/SBA-15 catalysts for methane dry reforming to syngas and hydrogen. *International journal of hydrogen energy*, 38(23), 9718-9731.

Wang, Y. M., Wu, Z. Y., Wei, Y. L., & Zhu, J. H. (2005). In situ coating metal oxide on SBA-15 in one-pot synthesis. *Microporous and mesoporous materials*, 84(1), 127-136.

Wanyika, H., Gatebe, E., Kioni, P., Tang, Z., & Gao, Y. (2011). Synthesis and characterization of ordered mesoporous silica nanoparticles with tunable physical properties by varying molar composition of reagents. *African Journal of Pharmacy and Pharmacology*, 5(21), 2402-2410.

Wehmas, L. C., Anders, C., Chess, J., Punnoose, A., Pereira, C. B., Greenwood, J. A., & Tanguay, R. L. (2015). Comparative metal oxide nanoparticle toxicity using embryonic zebrafish. *Toxicology reports*, 2, 702-715.

Wei, L., Hu, N., & Zhang, Y. (2010). Synthesis of polymer-mesoporous silica nanocomposites. *Materials*, 3(7), 4066-4079.

Wu, L., Wang, H., Lan, H., Liu, H., & Qu, J. (2013). Adsorption of Cu (II)–EDTA chelates on tri-ammonium-functionalized mesoporous silica from aqueous solution. *Separation and Purification Technology*, 117, 118-123.

Yang, H., Xu, R., Xue, X., Li, F., & Li, G. (2008). Hybrid surfactant-templated mesoporous silica formed in ethanol and its application for heavy metal removal. *Journal of Hazardous Materials*, 152(2), 690-698.

Yang, J., Zhang, F., Chen, Y., Qian, S., Hu, P., Li, W. & Zhao, D. (2011). Core-shell Ag@SiO2@mSiO2 mesoporous nanocarriers for metal-enhanced fluorescence. *Chemical Communications*, 47(42), 11618-11620.

Young, S. K. (2002). Overview of sol-gel science and technology (No. ARL-TR-2650). ARMY RESEARCH LAB ABERDEEN PROVING GROUND MD.

Yue, Y., Yin, C., Huo, F., Chao, J., & Zhang, Y. (2014). The application of natural drug-curcumin in the detection hypochlorous acid of real sample and its bioimaging. *Sensors and Actuators B: Chemical*, 202, 551-556.

Zaki, M. I., Knözinger, H., Tesche, B., Mekhemer, G. A. H. (2006). Influence of phosphonation and phosphation on surface acid–base and morphological properties of CaO as investigated by in situ FTIR spectroscopy and electron microscopy. *Journal of Colloid and Interface Science*, 303, 9-17.

Zebib, B., Mouloungui, Z., & Noirot, V. (2010). Stabilization of curcumin by complexation with divalent cations in glycerol/water system. *Bioinorganic chemistry and applications*, 2010.

Zhang, D., & Li, J. (2013). Ordered SBA-15 mesoporous silica with high amino-functionalization for adsorption of heavy metal ions. Chinese Science Bulletin, 58(8), 879-883.

Zhang, X., & Tsapatsis, M. (2011). Mesoporous silica nanoparticles from a clear sol and their transformation to lamellar silicalite-1 particles and films. Microporous and Mesoporous Materials, 138(1), 239-242.

Zhao, D., Feng, J., Huo, Q., Melosh, N., Fredrickson, G. H., Chmelka, B. F., & Stucky, G. D. (1998). Triblock copolymer syntheses of mesoporous silica with periodic 50 to 300 angstrom pores. science, 279(5350), 548-552.

Zhao, D., Huo, Q., Feng, J., Chmelka, B. F., & Stucky, G. D. (1998). Nonionic triblock and star diblock copolymer and oligomeric surfactant syntheses of highly ordered, hydrothermally stable, mesoporous silica structures. Journal of the American Chemical Society, 120(24), 6024-6036.

Zhao, D., Sun, J., Li, Q., & Stucky, G. D. (2000). Morphological control of highly ordered mesoporous silica SBA-15. Chemistry of Materials, 12(2), 275-279.

Zhao, X. Z., Jiang, T., Wang, L., Yang, H., Zhang, S., & Zhou, P. (2010). Interaction of curcumin with Zn (II) and Cu (II) ions based on experiment and theoretical calculation. Journal of Molecular Structure, 984(1), 316-325.

Zhu, Q. G. (2009). Studies On Prospect Of Curcumin As An Analytical Reagent For Aluminium (Doctoral dissertation, Universiti Sains Malaysia).